TECHNISCHE UNIVERSITÄT MÜNCHEN

Lehrstuhl für Theoretische Chemie

Jahn-Teller and spin-orbit coupling effects in transition-metal trifluorides

Padmabati Mondal

Vollständiger Abdruck der von der Fakultät für Chemie der Technischen Universität München zur Erlangung des akademischen Grades eines

Doktors der Naturwissenschaften

genehmigten Dissertation.

Vorsitzender:	Univ.-Prof. Dr. Tom Nilges
Prüfer der Dissertation:	
1.	Univ.-Prof. Dr. Wolfgang Domcke
2.	Univ.-Prof. Dr. Steffen J. Glaser

Die Dissertation wurde am 18.10.2012 bei der Technischen Universität München eingereicht und durch die Fakultät für Chemie am 22.11.2012 angenommen.

Contents

List of Abbreviations

JT	Jahn-Teller
CI	conical intersections
PE	potential-energy
SO	spin orbit
BP	Breit Pauli
DCB	Dirac Coulomb Breit
HF	Hartree-Fock
ESR	electron spin resonance
IR	infrared
DMS	dipole moment surfaces
BOA	Born-Oppenheimer approximation
KEO	kinetic-energy operator
NACT	nonadiabatic coupling term
ADT	adiabatic-to-diabatic transformation
TDSE	time-dependent Schrödinger equation
CASSCF	complete-active-space self-consistent-field
ANO	atomic natural orbitals
cc-pVQZ	correlation consistent polarized valence quadruple zeta
ROHF	restricted open-shell HF
CAS	complete active space
MRCI	multireference configuration interaction
CASPT2	complete-active-space purturbation theory (second order)
VEE	vertical excitation energy
FWHM	full width at half maximum
TDM	transition dipole moment

List of Notations

$\vec{\mu}_e(r)$	electronic part of $\vec{\mu}$
$\vec{\mu}_n(Q)$	nuclear part of $\vec{\mu}$
$\vec{\mu}_e^{(0)}$	$\vec{\mu}_e(0)$
$\vec{\mu}_e^{fi}$	$\langle\Psi_f\|\vec{\mu}_e(r)\|\Psi_i\rangle$
$\vec{\mu}_n^{fi}$	$\langle\Psi_f\|\vec{\mu}_n(Q)\|\Psi_i\rangle$
μ_{ex}	x-component of $\vec{\mu}_e(r)$
μ_{nx}	x-component of $\vec{\mu}_n(Q)$
μ_{ey}	y-component of $\vec{\mu}_e(r)$
μ_{ny}	y-component of $\vec{\mu}_n(Q)$
μ_{ex}^{fi}	$\langle\Psi_f\|\mu_{ex}\|\Psi_i\rangle$
μ_{nx}^{fi}	$\langle\Psi_f\|\mu_{nx}\|\Psi_i\rangle$
μ_{ey}^{fi}	$\langle\Psi_f\|\mu_{ey}\|\Psi_i\rangle$
μ_{ny}^{fi}	$\langle\Psi_f\|\mu_{ny}\|\Psi_i\rangle$
$\mu'_{nx,x}$	$\frac{\partial\mu_{nx}}{\partial Q_x}$
$\mu'_{nx,y}$	$\frac{\partial\mu_{nx}}{\partial Q_y}$
$\mu'_{ny,x}$	$\frac{\partial\mu_{ny}}{\partial Q_x}$
$\mu'_{ny,y}$	$\frac{\partial\mu_{ny}}{\partial Q_y}$
$\mu'_{nx,x,xx}$	$\langle\psi_x\|\mu'_{nx,x}\|\psi_x\rangle$
$\mu'_{nx,y,xx}$	$\langle\psi_x\|\mu'_{nx,y}\|\psi_x\rangle$
$\mu'_{nx,x,xy}$	$\langle\psi_x\|\mu'_{nx,x}\|\psi_y\rangle$
$\mu'_{nx,y,xy}$	$\langle\psi_x\|\mu'_{nx,y}\|\psi_y\rangle$
$\mu'_{nx,x,yy}$	$\langle\psi_y\|\mu'_{nx,x}\|\psi_y\rangle$
$\mu'_{nx,y,yy}$	$\langle\psi_y\|\mu'_{nx,y}\|\psi_y\rangle$
$\mu'_{ny,x,xx}$	$\langle\psi_x\|\mu'_{ny,x}\|\psi_x\rangle$
$\mu'_{ny,y,xx}$	$\langle\psi_x\|\mu'_{ny,y}\|\psi_x\rangle$
$\mu'_{ny,x,xy}$	$\langle\psi_x\|\mu'_{ny,x}\|\psi_y\rangle$
$\mu'_{ny,y,xy}$	$\langle\psi_x\|\mu'_{ny,y}\|\psi_y\rangle$
$\mu'_{ny,x,yy}$	$\langle\psi_y\|\mu'_{ny,x}\|\psi_y\rangle$
$\mu'_{ny,y,yy}$	$\langle\psi_y\|\mu'_{ny,y}\|\psi_y\rangle$
$\mu_{ex,xx}^{(0)}$	$\langle\psi_x\|\mu_{ex}^{(0)}\|\psi_x\rangle$
$\mu_{ex,xy}^{(0)}$	$\langle\psi_x\|\mu_{ex}^{(0)}\|\psi_y\rangle$
$\mu_{ex,yy}^{(0)}$	$\langle\psi_y\|\mu_{ex}^{(0)}\|\psi_y\rangle$
$\mu_{ey,xx}^{(0)}$	$\langle\psi_x\|\mu_{ey}^{(0)}\|\psi_x\rangle$
$\mu_{ey,xy}^{(0)}$	$\langle\psi_x\|\mu_{ey}^{(0)}\|\psi_y\rangle$
$\mu_{ey,yy}^{(0)}$	$\langle\psi_y\|\mu_{ey}^{(0)}\|\psi_y\rangle$

Chapter 1

Introduction

The Jahn-Teller (JT) effect[1,2] is one of the most interesting phenomena in modern physics and chemistry. The theory of the JT effect provides a general approach to the understanding of the properties of electronic spectra of molecules, clusters and solids. It is a special kind of vibronic coupling which is intimately related to the degeneracy (or pseudo-degeneracy) of electronic states. These degeneracies are induced by high spatial symmetries of the molecules or crystals. According to JT theorem,[1] formulated by H. A. Jahn and E. Teller in 1937,

"A configuration of a polyatomic molecule for an electronic state having orbital degeneracy cannot be stable with respect to all displacements of the nuclei unless in the original configuration the nuclei all lie on a straight line."

As JT effect is related to degenerate electronic states, the Born-Oppenheimer approximation (BOA)[3] (adiabatic approximation) breaks down in JT-active states. The JT effect can also be considered as a special case of conical intersections (CI).[1] Dynamical processes in photochemistry and photobiology, such as radiationless transitions in polyatomic molecules, are nowadays explained in terms of conically intersecting potential-energy (PE) surfaces.[4,5]

The JT effect is a well-known phenomenon in molecules, metal-molecule complexes, atomic clusters and crystals.[6] The applications of JT theory comprise the fields of spectroscopy, stereochemistry, structural phase transformations, as well as high-temperature superconductivity.[6] Various phenomena in coordination complexes (transition-metal complexes) would have remained unexplained without JT theory. Two types of the JT effect are distinguished in the literature. In some molecules and crystals, the distortion from the high-symmetry conformation is strong and permanent. This case is called static JT effect. In solids, the static JT effect usually is of primary interest, that is, the distortion of the crystal lattice or of impurity centers from the highest possible symmetry to a lower spatial symmetry.[7,8] In some molecules, the distortion can not be detected either due to random movements of bonds, which do not allow the measurement of nuclear geometry within a given time resolution, or else the distortion is too weak as to be observable. However, the distortion can be observed by freezing the nuclear motion out at low temperatures. This case is referred as dynamic Jahn-Teller distortion.[6–8]

The most common case is the $E \times e$ JT effect, where a doubly degenerate mode (e) lifts the degeneracy of a doubly degenerate electronic state (E) in trigonal, tetrahedral or

cubic systems.[6] The dynamical $E \times e$ JT effect has been investigated in great detail with various spectroscopic methods in molecular radicals and radical cations, examples being CH_3O, Na_3, NH_3^+, CH_3I^+ and $C_6H_6^+$.[9–14]

Another mechanism which tends to remove the degeneracy of open-shell electronic states is spin-orbit (SO) coupling. As is well known, SO coupling is a relativistic effect in electronic structure and as such increases with the second power of the nuclear charge in the valence shell of molecules.[15] While SO coupling can often be neglected in molecules containing first-row and second-row atoms, it is essential to take SO coupling into account for molecules and complexes containing transition metals, lanthanides or other heavy atoms. The JT effect and the effect of SO coupling tend to quench each other.[16] This phenomenon is particularly interesting when they are of comparable magnitudes which often is the case in first- and second-row transition-metal complexes.

The $E \times e$ JT Hamiltonian including SO coupling is well established for spin-$\frac{1}{2}$ systems, that is, for ^2E electronic states.[9,17–20] In the solid-state literature, SO coupling in electronic states of higher spin multiplicity has been considered, starting from atom-like SO operators

$$H_{SO} = \lambda \mathbf{L} \cdot \mathbf{S}, \tag{1.1}$$

assuming Russel-Saunders coupling and an empirical SO coupling constant λ.[16,21–23] Such empirical models are appropriate for impurity atoms with partially occupied inner shells in a rigid crystal environment. In molecules, metal-molecule complexes and atomic clusters, on the other hand, which are less rigid and often perform large-amplitude nuclear motions upon electronic excitation, a more accurate treatment of the SO interaction may be necessary. A microscopic and essentially exact description of SO coupling is provided by the Breit-Pauli (BP) operator. The BP operator can be derived from the Dirac-Coulomb-Breit (DCB) Hamiltonian by projection to a two-component form, using the Foldy-Wouthuysen transformation.[24–26] The matrix elements of the BP operator with nonrelativistic electronic wave functions can nowadays routinely be evaluated with a number of *ab initio* electronic-structure packages.[27–29] These recent developments open the way for systematic first-principles investigations of the interplay of JT and SO couplings in transition-metal and rare-earth compounds, as well as in other molecules or solid-state systems containing heavy atoms.

It has been shown by Poluyanov and Domcke that the SO coupling in systems with an even number of unpaired electrons is fundamentally different from SO coupling in systems with an odd number of unpaired electrons.[30] In the latter case, the SO splitting is non-zero for all members of the multiplet and the JT effect is quenched by strong SO coupling, as is well known for ^2E states.[9,17–20] In the former case, on the other hand, there always exists a pair of adiabatic electronic potentials which is strictly unaffected by the SO coupling.[30] The existence of an unquenched $E \times e$ JT effect in ^3E and ^5E states may explain why vibronic models which neglect SO coupling altogether can be unexpectedly successful for the interpretation of the spectra of transition-metal complexes.

Transition-metal trihalides are a well-known class of ionic crystals.[31,32] In the gas phase, transition-metal trihalides are mostly planar systems of D_{3h} symmetry with high-spin ground states.[33,34] The structures of a few transition-metal trifluorides have been determined by electron diffraction in the gas phase.[34–36] Spectroscopic information on

transition-metal trihalogenides is scarce and limited to vibrational spectra in rare-gas matrices.[37–39] A systematic study of the electronic structure of the trihalides of the first-row transition metals has been performed by Yates and Pitzer with the spin-restricted Hartree-Fock (HF) method.[33] A simple valence-state energy and hybridization model has been used to predict the structures of TiF_3 and CrF_3 by Charkin and Dyatkina[40,41] and of NiF_3 by Charkin.[42–44] Hastie, Hauge and Margrave[45] carried out a matrix infrared study of TiF_3 and determined the structure of the molecule. De Vore and Weltner[46] obtained matrix ESR spectra of TiF_3 which indicate that the molecule has a threefold symmetry axis and has an electronic ground state of ${}^2A_1{}'$ symmetry. The $E \times e$ JT coupling has been discussed by Yates and Pitzer for CoF_3, by Solomonik et al. for VF_3[47] and by Hargittai et al. for MnF_3.[34] In none of these studies, SO coupling effects were included.

In the present work, JT and SO coupling effects were analyzed with accurate first-principles methods in a series of first-row transition-metal trifluorides. While TiF_3, CrF_3 and NiF_3 are molecules containing atoms with even spin multiplicity (odd number of unpaired electrons), MnF_3 and CoF_3 are molecules with odd spin multiplicity (even number of unpaired electrons). TiF_3 has a ${}^2A_1{}'$ electronic ground state and low-lying ${}^2E''$ and ${}^2E'$ excited electronic states.[33] Both CrF_3 and NiF_3 have ${}^4A_1{}'$ ground states and low-lying ${}^4E'$ and ${}^4E''$ excited states.[33] MnF_3 has a ${}^5E'$ electronic ground state[33] and should thus be JT distorted in the ground state.[34] CoF_3 has a ${}^5A_1{}'$ ground state and a low-lying ${}^5E''$ excited electronic state.[33] The ab initio studies for MnF_3 and CoF_3 predicted strong JT activity of the degenerate bending mode, while the JT activity of the degenerate stretching mode is weak.[33] The SO splittings are expected to be of the order of 100 cm^{-1} for the first-row transition metals. They are thus of the same order of magnitude as the bending vibrational frequencies.

As Ti, Cr, Mn, Co and Ni have different positions in the first-row transition-metal series, the SO coupling ranges from $\Delta/\omega << 1$ (Ti, Cr, Mn) to $\Delta/\omega > 1$ (Co, Ni), where Δ is the SO splitting constant and ω is the harmonic vibrational frequency of the JT-active mode. Any combination of weak or strong JT effect with weak or moderate SO coupling can be found in these molecules. The first-row transition-metal trifluorides series are thus well-suited model systems for the investigation of the interplay of JT and SO coupling effects in high-spin states of trigonal systems. In case of the electronic states with strong JT coupling, inclusion of higher-order JT coupling may become important. The qualitative effects of linear, quadratic and higher-order JT couplings as well as SO splittings on the electronic spectra of high-spin E states of first-row transition-metal trifluorides have been analyzed in the present work.

In this work, the vibrational spectra in JT active states (${}^5E''$ state of MnF_3 and ${}^4E'$ state of NiF_3) are also investigated. In electronically degenerate states, a molecule may exhibit dipole moment which would be symmetry-forbidden if the electronic states were non-degenerate.[48] While the selection rules which govern the intensity of infrared (IR) transitions are well known for molecules in electronically non-degenerate states, the theory is more involved for molecules in degenerate electronic states. Usually, the electronic and vibrational spectra are well separated because of their vastly different frequencies. This separation does not apply, however, in case of JT systems, since the frequencies of electronic transitions between different sheets of the adiabtic PE surfaces are in the IR range.

The IR spectra of tetrahedral and octahedral molecules in degenerate electronic states were first discussed by Thorson.[49] Thereafter, interesting results were found by Child and Longuet-Higgins in the investigation of the IR spectra of hypothetical X_3 molecules of D_{3h} symmetry in a degenerate state.[48] Scharf and Miller showed that the symmetry selection rules of Child and Longuet-Higgins for IR vibrational transitions in electronically degenerate states are incomplete and the vibrational transitions that do not satisfy their selection rule can be exceptionally strong due to the presence of JT effect.[50] A compact set of symmetry selection rules for the JT-enhanced fundamental bands has been given by Watson.[51]

In the present work, the dipole moment surfaces (DMS) and vibronic IR spectra for JT-active E states of MnF_3 and NiF_3 are discussed. These are trigonal planar molecules and thus posses no permanent dipole moment. But displacements along their JT-active bending and stretching modes change the dipole moment of the system. For clarity, only the strongly JT-active bending mode is considered for the calculation of vibrational spectra. The effects of temperature as well as SO coupling are systematically explored. In the $^5E''$ state of MnF_3, the JT coupling is moderate and the SO splitting is weak. In the $^4E'$ state of NiF_3, on the other hand, strong JT effect and strong SO coupling are present.

The thesis is organized as follows : The second and the third chapter decribe the basic theoretical concepts and theoretical and computational methods, respectively. The electronic spectra of transition-metal trifluorides with even and odd spin multiplicities are discussed in the fourth and the fifth chapter, respectively. Details of the *ab initio* electronic-structure calculations, PE surfaces, electronic spectra are presented and analyzed therein. Chapter 6 contains the analysis of vibrational spectra for the $^5E''$ state of MnF_3 and the $^4E'$ state of NiF_3.

Chapter 2

Basic theoretical concepts

In this chapter, the basic theoretical background of the present work is discussed. The BOA, which plays key role in the description of chemistry, is described at the beginning. In Section 2.2, the basic concepts of JT theory as well as JT Hamiltonian are discussed. General theoretical backgrounds of relativistic quantum chemistry and the BP SO operator are discussed in Section 2.3. The basic concepts of nuclear dynamics (the time-independent and the time-dependent approach) are given in the last section.

2.1 The Born-Oppenheimer Approximation

The BOA is a key part of the quantum description of molecules.[3,52] The basic idea of this approximation is the separation of the electronic and the nuclear motions. Since the mass of an electron is small compared to that of the nuclei and the electrons therefore move quickly, the change in the nuclear positions can be considered to be negligible when calculating electronic wavefunctions. Therefore, the BOA allows the calculation of molecular dynamical processes to be executed in two steps. In the first step, the electronic problem is solved, keeping the nuclei fixed. For each fixed-nuclei position, the electronic energies are calculated by quantum chemical methods and thus the PE surface is obtained. In the second stage, the nuclear dynamics on one (or several) predetermined PE surfaces is performed.

The molecular Schrödinger equation can be written as

$$H\Psi_i(r,Q) = E_i\Psi_i(r,Q);\ i = 1,2,3\ldots \tag{2.1}$$

where i represents the i-th eigenstate of the system and H is the molecular Hamiltonian, which is defined as (at the nonrelativistic level of theory)

$$H = T_N + T_e + V_{NN} + V_{ee} + V_{Ne}. \tag{2.2}$$

T_N and T_e are the nuclear and electronic kinetic-energy operators (KEO), respectively. V_{NN} and V_{ee} are the electrostatic nuclear-nuclear and electron-electron repulsion terms and V_{Ne} is the nuclear-electron electrostatic attraction term.

The molecular wavefunction Ψ_i can be expanded using the following ansatz

$$\Psi_i(r,Q) = \sum_{i=1}^{N} \chi_i(Q)\Phi_i(r,Q) \tag{2.3}$$

where $\chi_i(Q)$ and $\Phi_i(r,Q)$ are nuclear and electronic wavefunctions, respectively. For a complete set of eigenstates (i.e., $N \to \infty$), the ansatz (2.3) is exact. In most applications in chemistry, N is restricted to a small number of close-lying electronic states and the effects of other electronic states are ignored. While the nuclear wavefunctions exclusively depend only on the nuclear coordinate Q, the electronic wavefunctions depend on both the electronic (r) and the nuclear coordinates. The electron-nuclear interation term V_{ne} in the molecular Hamiltonian is the main obstacle for a full separation of the electronic wavefunction from the nuclear wavefunction. In the BOA, the electronic wavefunction $\Phi_i(r,Q)$ depends parametrically on the nuclear coordinates which is denoted as $\Phi_i(r;Q)$. In the BOA, the ab initio electronic-structure algorithms solve the fixed-nuclei electronic Schrödinger equation

$$H_e\Phi_i(r;Q) = V_i(Q)\Phi_i(r;Q) \tag{2.4}$$

where the electronic Hamiltonian H_e is defined as

$$H_e = T_e + V_{NN} + V_{ee} + V_{Ne}. \tag{2.5}$$

$V_i(Q)$ is the PE obtained by solving the eigenvalue equation (2.4) for a fixed position of the nuclei. The PE surface can be obtained by varying the nuclear positions parametrically and solving Eq. (2.4) in each case.
Using the basis defined in (2.3) and the solution of electronic Schrödinger equation (2.4), one can derive the coupled nuclear Schrödinger equation[3]

$$(T_N I + V(Q) - \hat{\Lambda})\chi(Q) = E\chi(Q) \tag{2.6}$$

where I is the identity matrix. The $\hat{\Lambda}_{ij}$ are known as nonadiabatic coupling terms (NACT) and are defined as

$$\hat{\Lambda}_{ij} = -\int dr \Phi_i{}^*[T_N, \Phi_j]. \tag{2.7}$$

Using the general form of nuclear KEO as differential operator, the NACT can be split into two terms as

$$\hat{\Lambda}_{ij} = \sum_{n=1}^{M} F_{ij}^{(i)}\nabla - G_{ij}. \tag{2.8}$$

The terms F_{ij} and G_{ij} are known as the derivative coupling and the scalar coupling matrix, respectively and are defined as

$$F_{ij} = \langle\Phi_i|\nabla|\Phi_j\rangle;\ G_{ij} = \langle\Phi_i|\nabla^2|\Phi_j\rangle. \tag{2.9}$$

The solution of the nuclear Schrödinger equation is complicated by the NACT, especially for polyatomic molecules where several nuclear coordinates have to be considered. The

NACT are ignored ($\Lambda = 0$) in the so-called adiabatic approximation. The adiabatic approximation is based on the assumption that the KEO of the nuclei can be considered as a small perturbation of the electronic motion. A more useful approximation, which is known as the Born-Huang approximation, is obtained by neglecting only the off-diagonal terms of $\hat{\Lambda}_{ij}$.[53]

The adiabatic approximation may fail in many cases, especially when different electronic states are energetically close together. When two electronic states are exactly degenerate (at the point of CI), the derivative coupling terms diverge and the adiabatic approximation fails completely in the vicinity of the CI.

How can we solve the nuclear Schrödinger equation near CI which requires us to consider the NACT? Here the concept of diabatic wavefunctions enters. The diabatic wavefunctions are smooth and slowly varying functions of the nuclear coordinates and correspond to PE surfaces which may cross at the avoided crossing of the adiabatic PE surfaces. A unitary transformation matrix can be always found which transforms the adiabatic wavefunctions to diabatic ones in which the NACT are negligible at the CI. The concept of diabatic states is useful in several fields, ranging from atom-atom collisions to molecular spectroscopy.[54–56] For two coupled electronic states, the matrix Hamiltonian describing the nuclear motion in the adiabatic representation can be written as[54–56]

$$H = T_N I_2 + \begin{bmatrix} V_{11}(Q) - \hat{\Lambda}_{11} & -\hat{\Lambda}_{12} \\ -\hat{\Lambda}_{21} & V_{22}(Q) - \hat{\Lambda}_{22} \end{bmatrix}. \tag{2.10}$$

The adiabatic to diabatic transformation (ADT) can be introduced as

$$\begin{bmatrix} \phi_1^d(r,Q) \\ \phi_2^d(r,Q) \end{bmatrix} = \begin{bmatrix} \cos[\theta(Q)] & -\sin[\theta(Q)] \\ \sin[\theta(Q)] & \cos[\theta(Q)] \end{bmatrix} \begin{bmatrix} \Phi_1^{ad}(r,Q) \\ \Phi_2^{ad}(r,Q) \end{bmatrix}. \tag{2.11}$$

This transformation produces a new "nonadiabatic" operator

$$\hat{\lambda}_{ij} = \sum_{n=1}^{M} f_{ij}^{(i)} \nabla - g_{ij} \tag{2.12}$$

where

$$f_{ij} = \langle \phi_i | \nabla | \phi_j \rangle;\ g_{ij} = \langle \phi_i | \nabla^2 | \phi_j \rangle. \tag{2.13}$$

The advantage of the diabatic representation is that the so-called mixing angle $\theta(Q)$ in the transformation matrix can be chosen such that f_{ij} is small even in the vicinity of a CI.[54,55] While the PE surfaces are coupled by the nuclear KEO in the adiabatic representation, the PE surface couples different electronic states in the diabatic picture. The diabatic PE matrix can be chosen to be a continuously differentiable function of nuclear coordinates, even in the vicinity of a CI. Moreover, the nuclear wavefunctions in the diabatic representation do not carry a geometric phase factor.[57,58] This leads to a simplification of the calculation of the nuclear wavefunction. In vibronic coupling theory, diabatic potentials are usually constructed by the fitting of the eigenvalues of a diabatic model Hamiltonian to adiabatic *ab initio* data.[56]

2.2 Jahn-Teller theory and Jahn-Teller Hamiltonians

The JT effect is the most well-known example of vibronic coupling in non-linear molecules. The JT theorem is based on the group-theoretical analysis of the behaviour of the adiabatic PE surfaces of polyatomic systems near points of electronic degeneracy (CI). It states that any nonlinear molecular system in a degenerate electronic state will be unstable and will undergo distortion to form a system of lower symmetry.[1] The electronic degeneracy in case of JT effect is a consequence of molecular symmetry. The proof of JT theorem[1] came before calculations of adiabatic PE surfaces and stimulated the adiabatic PE surface calculation.

Let us consider an n-fold degenerate electronic state (n electronic states with identical energies) which is obtained by solving the electronic Schrödinger equation. How do these energies change under small displacements along an arbitrary vibrational coordinate? This can be answered by the theory of vibronic interactions without detailed calculations. The basic concepts of vibronic coupling in molecules, clusters and crystals in nonrelativistic limit, including the Renner-Teller and JT effect as special cases,[6,59] can be summarized as follows:
a. Representation of the nonrelativistic (electrostatic) Hamiltonian in a basis of diabatic electronic states.
b. Expansion of the electronic Hamiltonian in powers of normal-mode displacements at the reference geometry.
c. Use of symmetry selection rules for the determination of nonvanishing matrix elements. The operator of vibronic interactions in normal coordinates Q_{Γ_γ} is written as[6,59]

$$W(r,Q) = \sum_{\Gamma_\gamma} \left(\frac{\partial V(r,Q)}{\partial Q_{\Gamma_\gamma}} \right) Q_{\Gamma_\gamma} + \frac{1}{2} \sum_{\Gamma'_{\gamma'}} \sum_{\Gamma''_{\gamma''}} \left(\frac{\partial^2 V(r,Q)}{\partial Q_{\Gamma'_{\gamma'}} \partial Q_{\Gamma''_{\gamma''}}} \right) Q_{\Gamma'_{\gamma'}} Q_{\Gamma''_{\gamma''}} + \dots \qquad (2.14)$$

where V(r,Q) is the electron-nuclear interactions. These vibronic coupling constants connect the electronic structure and nuclear dynamics. The expansion (2.14) is valid only for small displacements from the reference point. To construct an adiabatic PE surface with large displacements of nuclear coordinates, one has to include the higher-order terms in the Taylor expansion (2.14).

The JT active vibrational modes can be identified by group theory. The JT coupling for a vibrational mode $Q_{\bar{\Gamma}}$ with an electronic state of symmetry Γ is nonzero if the symetrized product $[\Gamma \times \Gamma]$ contains the irreducible representation $\bar{\Gamma}$, where $\bar{\Gamma}$ is the symmetry of the vibrational mode $Q_{\bar{\Gamma}}$.[1] In trigonal systems, the symmetrized product $[E \times E]$ contains a and e *. The totally symmetric mode a cannot lift the degeneracy of a degenerate electronic state. The vibrational mode of e symmetry is JT active. In tetrahedral systems, the symmetrized product $[T \times T]$ contains the JT-active mode of representation e and t. Therefore, the $T \times e$ and the $T \times t$ JT effects are found in tetrahedral systems.[6] In octahedral systems, the $T \times t$, the $T \times e$ as well as the $E \times e$ JT effects are present. The three most interesting and well-studied JT effects are the $E \times e$, the $T \times e$ and the $T \times t$ JT effects where E, T are the symmetries of doubly- and triply-degenerate electronic states and e, t are the symmetries of doubly- and triply-degenerate vibrational

*Capital letters and lower case letters are used for electronic states and vibrational modes, respectively.

modes, respectively.

In this work, the $E \times e$ JT Hamiltonian for trigonal systems is of relevance. Following the basic concepts of vibronic coupling, the $E \times e$ JT Hamiltonian is expanded in terms of dimensionless normal modes Q_x, Q_y of a degenerate vibrational mode of e symmetry at the reference geometry up to second order according to Eq. 2.14

$$\begin{aligned} H_{es} &= H_{es}(0) + \frac{\partial H_{es}}{\partial Q_x}Q_x + \frac{\partial H_{es}}{\partial Q_y}Q_y + \frac{1}{2}\frac{\partial^2 H_{es}}{\partial Q_x^2}Q_x^2 + \frac{1}{2}\frac{\partial^2 H_{es}}{\partial Q_y^2}Q_y^2 + \frac{\partial^2 H_{es}}{\partial Q_x \partial Q_y}Q_xQ_y + \dots \\ &= H_0 + H_xQ_x + H_yQ_y + \frac{1}{2}H_{xx}Q_x^2 + \frac{1}{2}H_{yy}Q_y^2 + H_{xy}Q_xQ_y + \dots . \end{aligned} \tag{2.15}$$

where

$$\begin{aligned} H_0 &= H_{es}(0) \\ H_x &= \left(\frac{\partial H_{es}}{\partial Q_x}\right)_0 \\ H_{xy} &= \left(\frac{\partial^2 H_{es}}{\partial Q_x \partial Q_y}\right)_0 \ etc. \end{aligned} \tag{2.16}$$

Here H_0 transforms totally symmetric. The linear coefficients H_x and H_y transform as Q_x and Q_y, respectively. The quadratic coefficients H_{xx}, H_{yy} and H_{xy} transform as Q_x^2, Q_y^2 and Q_xQ_y, respectively.[6]

2.3 Relativistic Quantum Chemistry and the Breit-Pauli SO-operator

Relativistic effects play a major role in compounds containing heavy atoms, as the relativistic effects on energies and other physical quantities increase quadratically of the nuclear charge Z in the valence shell. The relativistic effects are of two types i.e. direct relativistic effects and indirect relativistic effects. SO coupling is a direct relativistic effect and becomes important for the spectroscopy of heavier elements e.g. transition-metal and rare-earth elements and their molecules.

SO coupling arises in Dirac theory, which is a fully relativistic theory for single-particle spin-1/2 systems.[60] The Dirac equation is written as

$$(\underline{\beta}mc^2 + c\underline{\alpha}\hat{p} + V)\Psi = \frac{\partial \Psi}{\partial t} \tag{2.17}$$

. Unlike the Schödinger equation, Dirac equation is a first-order differential equation with respect to both space and time. The Dirac Matrices $\underline{\alpha}$ and $\underline{\beta}$ are defined as

$$\underline{\alpha}_k = \begin{pmatrix} 0 & \sigma_k \\ \sigma_k & 0 \end{pmatrix} \quad k = x, y, z \tag{2.18}$$

$$\underline{\beta} = \begin{pmatrix} \mathbf{1}_2 & 0 \\ 0 & \mathbf{1}_2 \end{pmatrix}. \tag{2.19}$$

The wavefunction Ψ is a four component spinor

$$\Psi = \begin{pmatrix} \psi_{L1} \\ \psi_{L2} \\ \psi_{S1} \\ \psi_{S2} \end{pmatrix} \tag{2.20}$$

where the suffixes L, S correspond to the so-called large and small components, respectively. The Dirac equation consists of four coupled differential equation which consider the electronic and positronic degrees of freedom on equal footing.

For many-body relativistic electronic structure calculations, electron-electron interaction terms are included to single-particle Dirac Hamiltonian. The simplest form of the PE operator (nonrelativistic) is the Coulomb operator which correspond to electron-electron interaction i.e.

$$V = \sum_{k<l} \frac{1}{r_{kl}}. \tag{2.21}$$

The addition of Coulomb operator to Dirac Hamiltonian results in Dirac Coulomb operator. The Coulomb operator is not applicable in relativistic theory as it is not Lorentz invariant. In nonrelativistic theory, the Coulomb term implies the instantaneous interaction between two electrons which is not possible in relativistic theory as the speed of interaction is limited by the finite speed of light. Therefore, a retardation term is added.[61] The PE operator, after the addition of the retardation term, for a two-particle system reads as

$$V_{12} = \frac{1}{r_{12}} - \frac{1}{2r_{12}} \left((\underline{\alpha}_1 . \underline{\alpha}_2) + \frac{(\underline{\alpha}_1 . r_{12})(\underline{\alpha}_2 . r_{12})}{r_{12}^2} \right). \tag{2.22}$$

Here the Breit operator (the terms excluding the Coulomb operator in the r.h.s. of Eq. (2.22)) consists of the Gaunt term and the retardation term. The full PE operator in Eq. (2.22) is called the Coulomb-Breit operator. $\underline{\alpha}_1$ and $\underline{\alpha}_2$ are the matrices consist of Pauli-spin matrices for electron 1 and 2, respectively. The complete Hamiltonian containing the Dirac operator as well as the Coulomb-Breit operator is called DCB Hamiltonian.

Many-electron relativistic quantum-chemical calculations are considerably more expensive than their non-relativistic analogues. This is due to the fact that in any relativistic theory one has to solve Dirac equation for each electron considering also the degrees of freedom for its charge-conjugated particle on equal footing (four-component wave functions instead of two-component spin-orbitals for nonrelativistic analogue). Therefore, in most of the many-electron relativistic quantum-chemical calculations, two-component wavefunctions (which are transformed from the four component wavefunctions) are solved to reduce the computational cost.

Using the Foldy-Wouthuysen transformation, the operators which couple the large (electronic) and small (positronic) components of the wavefunction are removed and then the Dirac equation can be solved only for two-component wavefunctions (electronic).[26]

2.3.1 The Breit-Pauli spin-orbit operator

It was already mentioned that in case of molecules, metal-molecule complexes and atomic clusters, which are less rigid and often perform large-amplitude nuclear motions upon electronic excitation, the use of a microscopic spin-orbit operator is necessary instead of effective empirical SO coupling operator given in Eq. (1.1).

The theory of the interaction of the magnetic moments of the electron spin and the orbital motion in one- and two-eletron atoms was formulated by Heisenberg and Pauli,[62,63] shortly before the advent of four-component Dirac theory,[60] starting from the Schrödinger equation of a molecule in an external electric and magnetic field. The theory is then obtained by assuming that the scalar potential is purely Coulombic and the magnetic field arises from the electronic spin.

The two-component microscopic BP SO operator can be derived from the relativistic four component DCB operator using the FW transformation for chemical application.[24–26]

The so-called one- and two-electron BP SO Hamiltonian is given by (in atomic unit)[64]

$$\begin{aligned}
\hat{H}_{SO}^{BP} &= \frac{1}{2c^2}\{\sum_k \left(-\vec{\nabla}_k \left(\sum_n \frac{Z_n}{\hat{r}_{kn}}\right) \times \vec{\hat{p}}_k\right) \vec{\hat{s}}_k && (2.23)\\
&+ \sum_k \sum_{l\neq k} \left(\vec{\nabla}_k \left(\frac{1}{\hat{r}_{kl}}\right) \times \vec{\hat{p}}_k\right) \vec{\hat{s}}_k && (2.24)\\
&+ \sum_k \sum_{l\neq k} \left(\vec{\nabla}_l \left(\frac{1}{\hat{r}_{kl}}\right) \times \vec{\hat{p}}_l\right) \vec{\hat{s}}_k && (2.25)\\
&+ \sum_l \sum_{k\neq l} \left(\vec{\nabla}_k \left(\frac{1}{\hat{r}_{lk}}\right) \times \vec{\hat{p}}_k\right) \vec{\hat{s}}_l\} && (2.26)
\end{aligned}$$

where n represents the nuclei, k and l represent the electrons, Z_n is the charge of the nucleus n and c is the speed of light. Here, (2.23) is an one-electron operator, describing the interaction of the spin magnetic moment of an electron k with the magnetic moment that arises from its orbitting in the field of nucleus n. (2.24) is the two-electron analogue relating the motion of electron k in the field of electron l. Terms (2.25) and (2.26) describe the coupling between the spin magnetic moment of electron k and the orbital magnetic moment of electron l and vice versa. In most cases, the BP operator is written by contracting the spin-same (2.24) and spin-other-orbit parts (2.25, 2.26) of the two-electron Hamiltonian into a single term and reads[64]

$$\hat{H}_{SO}^{BP} = \frac{1}{2c^2}\sum_k \{\sum_n Z_n \left(\frac{\vec{\hat{r}}_{kn}}{\hat{r}_{kn}^3} \times \vec{\hat{p}}_k\right) - \sum_{l\neq k} \frac{\vec{\hat{r}}_{kl}}{\hat{r}_{kl}^3} \times (\vec{\hat{p}}_k - 2\vec{\hat{p}}_l)\}\vec{\hat{s}}_k. \qquad (2.27)$$

Since the BP SO operator implicitly contains coupling terms between electronic and positronic states, it is unbound from below and thus can be employed safely only in perturbation theory.

To include the SO coupling effects in vibronic coupling theory, the SO operator is

treated exactly in the same manner as the electrostatic Hamiltonian, i.e,
a. Representation of BP operator in a basis of (nonrelativistic) diabatic electronic states.
b. Expansion of the BP operator in powers of normal-mode displacements at the reference geometry.
c. Use of symmetry selection rules to determine the nonvanishing matrix elements.
The use of nonrelativistic basis functions in a. is appropriate only when the SO coupling is a relatively weak perturbation of the nonrelativistic Hamiltonian, which typically is the case of first and second-row transition metals.[30,65]

2.4 Electronic and vibrational spectra: time-independent and time-dependent approaches

In this section, two different approaches (time-independent and time-dependent) to calculate the vibronic structure of electronic spectra and vibrational spectra are discussed. While electronic spectra correspond to transitions from a nondegenerate initial state to the JT-active state of interest, vibrational spectra correspond to transitions from initial vibrational levels to final vibrational levels within the same JT-active electronic state. Since both the electronic and vibrational spectra are of vibronic character, it is better to refer them as "external vibronic spectra" and "internal vibronic spectra", respectively.

2.4.1 Time-independent approach

Let us assume that a molecule initially in the state Ψ_i is excited by a periodic perturbation described by the interaction operator $\hat{H}'$ into a manifold of JT-active electronic state E. The spectral intensity, i.e. the probability of transition from the initial electronic state Ψ_i to the final electronic state Ψ_f can be calculated by using the well-known Fermi-Golden rule[66]

$$I_f = \sum_i |\langle \Psi_f | \hat{H}' | \Psi_i \rangle|^2 \delta(E_f - E_i - \omega) \tag{2.28}$$

where $E_f - E_i$ is the difference between the energy eigenvalues of the final and the initial state and ω is the frequency of the electromagnetic radiation. Ψ_f is the final vibronic eigenstate. In case of calculation of external vibronic spectra and at T = 0 K, Ψ_i is the vibrational ground state of an external nondegenerate electronic state. For the calculation of internal vibronic spectra and at T = 0 K, Ψ_i is the ground vibronic eigenstate within the E state. In the time-independent approach, the vibronic wavefunctions are represented in a finite electronic-vibrational product basis.

2.4.2 Time-dependent approach

In the time-dependent picture, the absorption/emission spectrum is obtained as the Fourier transform of the autocorrelation function[67,68]

$$P(\omega) \sim \frac{1}{2\pi} \int_{-\infty}^{\infty} dt \langle \Psi(Q,0)|\Psi(Q,t)\rangle e^{i\omega t} \tag{2.29}$$

where $\langle \Psi(Q,0)|\Psi(Q,t)\rangle$ is the autocorrelation function. $|\Psi(Q,0)\rangle$ is the wave function prepared by the electronic transition from a nondegenerate initial electronic state to the JT-active state of interest. $|\Psi(Q,t)\rangle$ is obtained by solving the time-dependent Schrödinger equation (TDSE)

$$i\frac{\partial}{\partial t}|\Psi(Q,t)\rangle = \hat{H}|\Psi(Q,t)\rangle. \tag{2.30}$$

If the Hamiltonian is time-independent, the analytic solution of the above equation is

$$|\Psi(Q,t)\rangle = e^{-iHt}|\Psi(Q,0)\rangle = U(t,0)|\Psi(Q,0)\rangle, \tag{2.31}$$

where $U(t,0) = e^{-iHt}$ is the time-evolution operator.

The time-dependent approach is an alternative to the time-independent theory discussed in Section 2.4.1. The solution of TDSE is obtained by the time-dependent wavepacket propagation of the initial wavefunction $|\Psi(Q,0)\rangle$.[69] This approach also relies on the representation of nuclear wavefunctions in finite basis. Here, the wave-packet is interpolated on discrete grid points and the integrals over the interpolating functions are determined.[70] Since last three decades, the application of time-dependent method in molecular dynamics studies has drastically increased due to availability of high-performance computers.[71,72] Different wavepacket propagation scheme can be employed to obtain $\Psi(Q,t)$ by solving Eq. (2.30) and thus to calculate the autocorrelation function. A wavepacket is a coherent superposition of stationary states, each being multiplied by the time-evolution factor e^{-iHt}. The basic idea is to create a wavepacket in any one of the JT-active state and then propagating it with respect to time using the time-evolution operator.

Chapter 3

Theoretical and computational methods

In this chapter, the theoretical and computational methods, which are used in this work, are discussed. In Section 3.1, the derivations of model JT Hamiltonian as well as model Breit-Pauli SO Hamiltonian are discussed. The definition of symmetry coordinates and the transformation from symmetry coordinates to normal coordinates are described in Section 3.2. The description of nuclear dynamics (both in the time-independent and time-dependent approaches) to calculate external vibronic spectra are given in Section 3.3. In the last section, the calculation of vibrational spectra, using the time-independent method, is discussed.

3.1 Multimode Jahn-Teller Hamiltonian with spin-orbit coupling

For first-row transition metals, the SO interaction can be considered as a relatively weak perturbation of the nonrelativistic (electrostatic) Hamiltonian. The electronic Hamiltonian can be written as a sum of the electrostatic Hamiltonian and SO operator

$$H_e = H_{es} + H_{SO}. \tag{3.1}$$

The electrostatic and SO Hamiltonians will be discussed separately in first two subsections and will then be added in Subsection 3.1.3.

3.1.1 Electrostatic Hamiltonian for trigonal systems

Let us consider a trigonal molecule XY_3 of D_{3h} symmetry with one, two, three or four unpaired electrons. The transition-metal trifluorides (MF_3) are XY_3 types of molecules in which the metal M is at the center and three F atoms are situated at the three corners of an equilateral triangle. All of the four nuclei of MF_3 are located in xy plane. The six vibrational modes of MF_3 belong to the following symmetry species in the D_{3h} point group,

$$\Gamma_{vib} = a_1{}' + a_2{}'' + 2e'. \tag{3.2}$$

The symmetrized square of the E' or E'' representions is

$$[E']^2 = [E'']^2 = {A_1}' + E', \tag{3.3}$$

which indicates that the vibrational modes of e' symmetry can lift the degeneracy of E electronic states leading to the $E \times e$ JT effect.[1] An MF_3 molecules thus possess two JT-active vibrational modes (the bending and the stretching modes) of e' symmetry.
For the purpose of symmetry analysis, H_{es} in Eq. (3.1) for many-electron systems can be approximated by the following effective operator (in atomic units)

$$H_{es} = \sum_k H_{es}^{(k)} + \sum_{k<l} \frac{1}{r_{kl}}, \tag{3.4}$$

$$H_{es}^{(k)} = -\frac{1}{2}\nabla^2 - e\Phi(r_k), \tag{3.5}$$

$$\Phi(r_k) = \sum_{n=1}^{3} \frac{\tilde{q}_{Y_n}}{r_{kn}} + \frac{\tilde{q}_X}{r_{k4}}. \tag{3.6}$$

Here the electron-electron correlation in Eq. (3.4) is restricted to the correlation between unpaired electrons. $\tilde{q}_{Y_n}$ is the effective nuclear charge of the three equivalent atoms and $\tilde{q}_X$ is the effective nuclear charge of the atom X. The r_{kn} and r_{kl} are the electron-nuclei and electron-electron distances, respectively, defined as

$$r_{kn} = |r_k - Q_n|, \ n = 1, 2, 3, 4; \tag{3.7}$$

$$r_{kl} = |r_k - r_l|, \tag{3.8}$$

where r_k and r_l are the radius vectors of the k-th and l-th unpaired electrons, respectively and Q_n, $n = 1, 2, 3, 4$, denote the positions of the nuclei. For simplicity, the case with one unpaired electron will be discussed in the following. The unpaired electron is described in an effective single-particle picture. For a XY_3 molecule with one unpaired electron Eq. (3.4) simplifies to

$$H_{es} = -\frac{1}{2}\nabla^2 - e\Phi(r), \tag{3.9}$$

$$\Phi(r) = \sum_{n=1}^{3} \frac{\tilde{q}_{Y_n}}{r_n} + \frac{\tilde{q}_X}{r_4}, \tag{3.10}$$

where

$$r_n = |r - Q_n|, \ n = 1, 2, 3, 4. \tag{3.11}$$

To take the advantage of the D_{3h} symmetry of the molecule in the electrostatic Hamiltonian, symmetry-adapted linear combinations of atom-centered electronic basis functions

are generated. A pair of electronic basis functions transforming as x and y in D_{3h} symmetry, is

$$\psi_x = \frac{1}{\sqrt{6}}[2\chi_1 - \chi_2 - \chi_3] \tag{3.12a}$$

$$\psi_y = \frac{1}{\sqrt{2}}[\chi_2 - \chi_3] \tag{3.12b}$$

where the atom-centered basis functions are defined as

$$\chi_n = \chi(\vec{r_n}),; \; n = 1, 2, 3, 4. \tag{3.13}$$

Introducing the spin of the electron, we obtain four non-relativistic spin-orbital basis functions

$$\begin{aligned} {\psi_x}^+ &= \psi_x\alpha \\ {\psi_x}^- &= \psi_x\beta \\ {\psi_y}^+ &= \psi_y\alpha \\ {\psi_y}^- &= \psi_y\beta \end{aligned} \tag{3.14}$$

where α, β represent the spin projections 1/2 and -1/2 respectively.

Using the Taylor expansion of electrostatic JT Hamiltonian (2.15), the transformation properties of H_0, $H_{x(y)}$, H_{xy} mentioned in Section 2.2 and the invariance condition of electrostatic Hamiltonian under symmetry transformations, the well-known electrostatic vibronic matrix is obtained by taking matrix elements of the Hamiltonian up to second order with the electronic basis functions ψ_x, ${\psi_y}$[6–8]

$$H_{es} = \frac{1}{2}\omega(Q_x^2 + Q_y^2)I_2 + \begin{pmatrix} \kappa Q_x + \frac{1}{2}g(Q_x^2 - Q_y^2) & \kappa Q_y - gQ_xQ_y \\ \kappa Q_y - gQ_xQ_y & -\kappa Q_x - \frac{1}{2}g(Q_x^2 - Q_y^2) \end{pmatrix}. \tag{3.15}$$

Introducing the complex electronic basis functions

$$\psi_+ = \frac{1}{\sqrt{2}}(\psi_x + i\psi_y) \quad \psi_- = \frac{1}{\sqrt{2}}(\psi_x - i\psi_y), \tag{3.16}$$

and polar nuclear coordinates

$$\rho e^{i\theta} = Q_+ = Q_x + iQ_y \quad \rho e^{-i\theta} = Q_- = Q_x - iQ_y, \tag{3.17}$$

the electrostatic Hamiltonian up to second order reads[6,73]

$$H_{es} = \frac{1}{2}\omega\rho^2 I_2 + \begin{pmatrix} 0 & \kappa\rho e^{i\theta} + \frac{1}{2}g\rho^2 e^{-2i\theta} \\ \kappa\rho e^{-i\theta} + \frac{1}{2}g\rho^2 e^{2i\theta} & 0 \end{pmatrix} \tag{3.18}$$

where ω, κ and g are the vibrational frequency of the e mode, the linear and quadratic JT coupling constants, respectively.

The adiabatic PE functions are obtained by diagonalizing the electrostatic Hamiltonian H_{es} in Eq. (3.15). The adiabatic PE functions are :

$$V_- = \frac{1}{2}\omega({Q_x}^2 + {Q_y}^2) - \sqrt{W^2 + Z^2} \tag{3.19}$$

$$V_+ = \frac{1}{2}\omega({Q_x}^2 + {Q_y}^2) + \sqrt{W^2 + Z^2} \tag{3.20}$$

where W and Z, which correspond to the diagonal and the offdiagonal elements of non-reltivistic JT Hamiltonian are, in the approximation of linear-plus-quadratic JT coupling, given by

$$W = \kappa Q_x + \frac{1}{2}g({Q_x}^2 - {Q_y}^2) \tag{3.21}$$

$$Z = \kappa Q_y - gQ_xQ_y. \tag{3.22}$$

In the complex representation, adiabatic PE functions read

$$V_- = \frac{1}{2}\omega\rho^2 - |q| \tag{3.23}$$

$$V_+ = \frac{1}{2}\omega\rho^2 + |q| \tag{3.24}$$

where, in the approximation of linear-plus-quadratic JT coupling,

$$q = \kappa\rho e^{i\theta} + \frac{1}{2}g\rho^2 e^{-2i\theta}. \tag{3.25}$$

So far, the electrostatic Hamiltonian matrix is derived using an expansion up to second-order in dimensionless normal-modes. In many cases, the JT effect is so strong that the standard JT expansion up to second order is not sufficient to describe the *ab initio* PE surfaces accurately. This happens particularly in cases where large amplitude motion become important. The first systematic treatment of the $E \times e$ JT problem considering the large-amplitude nuclear displacement was developed by Viel and Eisfeld.[74] It was shown that a higher-order expansion (beyond second-order) can significantly improve the accuracy of the JT PE surfaces.[74] The sixth-order expansion of electrostatic JT Hamiltonian (extension of (2.15) up to sixth-order) in the real representation reads[74]

$$H_{es} = \sum_{n=0}^{6} \frac{1}{n!}\left[\begin{pmatrix} U^{(n)} & 0 \\ 0 & U^{(n)} \end{pmatrix} + \begin{pmatrix} W^{(n)} & Z^{(n)} \\ Z^{(n)} & -W^{(n)} \end{pmatrix}\right]. \tag{3.26}$$

The adiabatic PE functions including the higher-order JT coupling terms, obtained after diagonalizing the higher-order electrostatic Hamiltonian in Eq. (3.26), are

$$V_- = \sum_{n=0}^{6} \frac{1}{n!}2U^{(n)} - \sqrt{\left(\sum_{n=0}^{6} \frac{1}{n!}W^{(n)}\right)^2 + \left(\sum_{n=0}^{6} \frac{1}{n!}Z^{(n)}\right)^2} \tag{3.27}$$

$$V_+ = \sum_{n=0}^{6} \frac{1}{n!}2U^{(n)} + \sqrt{\left(\sum_{n=0}^{6} \frac{1}{n!}W^{(n)}\right)^2 + \left(\sum_{n=0}^{6} \frac{1}{n!}Z^{(n)}\right)^2} \tag{3.28}$$

where $U^{(n)}$ represents the expansion of the trace and $W^{(n)}$, $Z^{(n)}$ are the diagonal and the off-diagonal JT coupling terms. The expressions for $U^{(n)}$, $W^{(n)}$ and $Z^{(n)}$ are given in Appendix A (up to sixth order for a single e-mode).[74]

3.1.2 The spin-orbit Hamiltonian for trigonal systems

The Breit-Pauli operator for a four-atomic many electron system with D_{3h} symmetry reads as

$$H_{SO} = \sum_k H_{SO}^{(k)} + \sum_{k<l} H_{SO}^{(kl)}, \tag{3.29}$$

$$H_{SO}^{(k)} = -ig_e\beta_e^2 \mathbf{S}_k \sum_{n=1}^{4} \frac{\tilde{q}_n}{r_{kn}^3}(r_{kn} \times \nabla_k), \tag{3.30}$$

$$H_{SO}^{(kl)} = ig_e\beta_e^2 \frac{1}{r_{kl}^3} \left[\mathbf{S}_k[r_{kl} \times (\nabla_k - 2\nabla_l)] + \mathbf{S}_l[r_{kl} \times (\nabla_l - 2\nabla_k)]\right] \tag{3.31}$$

with

$$\mathbf{S}_k = \frac{1}{2}\left(\mathbf{i}\sigma_x^{(k)} + \mathbf{j}\sigma_y^{(k)} + \mathbf{k}\sigma_z^{(k)}\right). \tag{3.32}$$

The two-electron part of the BP SO operator becomes relevant for electronic states with more than one unpaired electrons (triplet, quartet or quintet states). For simplicity, here we discuss the BP SO operator for system with one unpaired electron. The extension to more than one unpaired electron is straightforward.

For one unpaired electron, equation (3.29) simplifies to

$$H_{SO} = -ig_e\beta_e^2 \mathbf{S}. \sum_{n=1}^{4} \frac{\tilde{q}_n}{r_n^3}(r_n \times \nabla), \tag{3.33}$$

with

$$\mathbf{S} = \frac{1}{2}(\mathbf{i}\sigma_x + \mathbf{j}\sigma_y + \mathbf{k}\sigma_z). \tag{3.34}$$

Here σ_x, σ_y, σ_z are the Pauli spin matrices acting on the spin eigenstates of the electron,

$$\beta_e = \frac{1}{2c} \tag{3.35}$$

is the Bohr magneton, g_e is the g-factor of the electron ($g_e = 2.0023$) and $\tilde{q}_n$ is the effective nuclear charge. **i**, **j** and **k** are the cartesian unit vectors. The BP operator has the same structure as empirical SO operator in Eq. (1.1) but it depends explicitly on the electron-nuclear distances r_n for each nucleus n. Although the magnetic interaction energy is of the order r_n^{-2} and thus of shorter range than the electrostatic interaction, it can result in a nonnegligible dependence of the SO operator on the nuclear coordinates. This effect is neglected when empirical SO operators are employed.

For the symmetry analysis, it is useful to write the BP operator in determinantal form[75]

$$H_{SO} = \frac{1}{2}ig_e\beta_e^2 \begin{vmatrix} \sigma_x & \sigma_y & \sigma_z \\ \Phi_x & \Phi_y & \Phi_z \\ \frac{d}{dx} & \frac{d}{dy} & \frac{d}{dz} \end{vmatrix}, \tag{3.36}$$

where Φ is the electron-nuclear interaction defined in Eq. (3.10) and

$$\Phi_x = \frac{\partial \Phi}{\partial x},\ etc. \tag{3.37}$$

The invariance condition of the SO Hamiltonian is

$$Z_n H_{SO} Z_n^{-1} = H_{SO} \tag{3.38}$$

where Z_n is a symmetry operation in an extended symmetry group which can be obtained by multiplying a 2×2 unitary transformation with the symmetry operations of the D_{3h} symmetry group. Each of the usual spatial symmetry operation X_n of the D_{3h} point group is thus complemented by a 2×2 matrix U_n which operates on the spin matrices.

$$Z_n = X_n U_n^{\dagger} \tag{3.39}$$

where

$$U_n U_n^{\dagger} = \mathbf{1_2}. \tag{3.40}$$

For each of the 12 symmetry elements of the D_{3h} point group, an associated unitary 2×2 matrix can be determined using the determinantal form of Eq. (3.36). The resulting group of order 24 is the symmetry group of SO operator and is known as spin-double group D'_{3h}.[76]

Moreover, H_{SO} has time-reversal symmetry. The time reversal operator is[77]

$$\tau = -i\sigma_y \hat{cc} = \begin{pmatrix} 0 & -1 \\ 1 & 0 \end{pmatrix} \hat{cc}. \tag{3.41}$$

Here, $\hat{cc}$ correspond to the operation of complex conjugation.

Following the basic concepts in Subsection 2.3.1, the SO Hamiltonian is expanded as

$$H_{SO} = h_0 + h_x Q_x + h_y Q_y + \ldots. \tag{3.42}$$

The expansion is taken up to the first order, assuming that the SO coupling is weak compared to the electrostatic interactions. The individual SO operators can be written as

$$\begin{aligned} h_0 &= h^x \sigma_x + h^y \sigma_y + h^z \sigma_z \\ h_x &= h_x^x \sigma_x + h_x^y \sigma_y + h_x^z \sigma_z \\ h_y &= h_y^x \sigma_x + h_y^y \sigma_y + h_y^z \sigma_z \end{aligned} \tag{3.43}$$

with

$$\begin{aligned} h^x &= i g_e \beta_e^2 \tilde{q} \left(\frac{\partial \Phi}{\partial y} \frac{\partial}{\partial z} - \frac{\partial \Phi}{\partial z} \frac{\partial}{\partial y} \right) \\ h^y &= i g_e \beta_e^2 \tilde{q} \left(\frac{\partial \Phi}{\partial z} \frac{\partial}{\partial x} - \frac{\partial \Phi}{\partial x} \frac{\partial}{\partial z} \right) \\ h^z &= i g_e \beta_e^2 \tilde{q} \left(\frac{\partial \Phi}{\partial x} \frac{\partial}{\partial y} - \frac{\partial \Phi}{\partial y} \frac{\partial}{\partial x} \right) \end{aligned} \tag{3.44}$$

and

$$h_x^x = \left(\frac{\partial h_x}{\partial Q_x}\right)_0,$$
$$h_y^x = \left(\frac{\partial h_x}{\partial Q_y}\right)_0, etc. \tag{3.45}$$

The matrix elements of H_{SO} can be calculated with the spin-orbital basis functions of Eq. (3.14). The resulting matrix is written as[75]

$$H_{SO} = i \begin{pmatrix} 0 & \Delta_z & 0 & \Delta_x - i\Delta_y \\ -\Delta_z & 0 & -\Delta_x + i\Delta_y & 0 \\ 0 & \Delta_x + i\Delta_y & 0 & -\Delta_z \\ -\Delta_x - i\Delta_y & 0 & \Delta_z & 0 \end{pmatrix}, \tag{3.46}$$

where Δ_x, Δ_y and Δ_z are real constants. In the complex representation (Eq. (3.16)), H_{SO} takes the form[65]

$$H_{SO} = \begin{pmatrix} \Delta_z & 0 & \Delta_x - i\Delta_y & 0 \\ 0 & -\Delta_z & 0 & -\Delta_x + i\Delta_y \\ \Delta_x + i\Delta_y & 0 & -\Delta_z & 0 \\ 0 & -\Delta_x - i\Delta_y & 0 & \Delta_z \end{pmatrix}. \tag{3.47}$$

The parameters Δ_x, Δ_y and Δ_z do not depend on the nuclear geometry (up to first order).[65]

It is straightforward to find a unitary 4×4 matrix S which diagonalizes H_{SO} in Eq. (3.47), yielding[65]

$$S^\dagger H_{SO} S = \begin{pmatrix} \Delta & 0 & 0 & 0 \\ 0 & -\Delta & 0 & 0 \\ 0 & 0 & -\Delta & 0 \\ 0 & 0 & 0 & \Delta \end{pmatrix}, \tag{3.48}$$

with

$$\Delta = \sqrt{\Delta_x^2 + \Delta_y^2 + \Delta_z^2}. \tag{3.49}$$

In case of molecules with D_{3h} symmetry, $\Delta_x = \Delta_y = 0$. In this case, Eq. (3.46) simplifies to

$$H_{SO} = i \begin{pmatrix} 0 & \Delta_z & 0 & 0 \\ -\Delta_z & 0 & 0 & 0 \\ 0 & 0 & 0 & -\Delta_z \\ 0 & 0 & \Delta_z & 0 \end{pmatrix}, \tag{3.50}$$

and Eq. (3.47) simplifies to

$$H_{SO} = \begin{pmatrix} \Delta_z & 0 & 0 & 0 \\ 0 & -\Delta_z & 0 & 0 \\ 0 & 0 & -\Delta_z & 0 \\ 0 & 0 & 0 & \Delta_z \end{pmatrix}. \tag{3.51}$$

3.1.3 The $E \times e$ vibronic Hamiltonian with SO coupling

Combining the results of Subsections 3.1.1 and 3.1.2, the full Hamiltonian H_{JTSO} for a single-mode $^2E \times e$ JT system in complex representation reads as[65]

$$H_{JTSO} = (T_N + \frac{1}{2}\omega\rho^2)I_4 + I_2 \otimes \gamma_c + A_2 \otimes \sigma_z, \tag{3.52}$$

where

$$T_N = -\frac{1}{2}\omega\left(\frac{1}{\rho}\frac{\partial}{\partial\rho}\rho\frac{\partial}{\partial\rho} + \frac{1}{\rho^2}\frac{\partial^2}{\partial\theta^2}\right)$$

is the KEO,

$$\gamma_c = \begin{pmatrix} 0 & q \\ q^* & 0 \end{pmatrix} \tag{3.53}$$

with q defined in Eq. (3.25) and

$$A_2 = \begin{pmatrix} \Delta_z & 0 \\ 0 & -\Delta_z \end{pmatrix}. \tag{3.54}$$

In real representation, the $^2E \times e$ JT-SO Hamiltonian is

$$H_{JTSO} = \left(-\frac{1}{2}\omega\left(\frac{\partial^2}{\partial Q_x^2} + \frac{\partial^2}{\partial Q_y^2}\right) + \frac{1}{2}\omega(Q_x^2 + Q_y^2)\right) I_4 + I_2 \otimes \gamma_r + A_2 \otimes \sigma_y, \tag{3.55}$$

where

$$\gamma_r = \begin{pmatrix} W & Z \\ Z & -W \end{pmatrix} \tag{3.56}$$

with W and Z defined in Eqs. (3.21, 3.22). The two-mode $^2E \times e$ JT-SO Hamiltonian in real representation for a molecule with D_{3h} symmetry reads

$$H_{JTSO} = \left(-\frac{1}{2}\sum_{i=3}^{4}\omega_i\left(\frac{\partial^2}{\partial Q_{ix}^2} + \frac{\partial^2}{\partial Q_{iy}^2}\right) + \frac{1}{2}\omega_i(Q_{ix}^2 + Q_{iy}^2)\right) I_4 + I_2 \otimes \gamma_r + A_2 \otimes \sigma_y. \tag{3.57}$$

The subscript i ennumerates the JT-active bending and stretching modes. W and Z, which correspond to the diagonal and the offdiagonal elements of nonreltivistic JT coupling term γ_r, read in the case of two-mode linear-plus-quadratic JT coupling as[56,74]

$$W = \sum_{i=3}^{4}\kappa_i Q_{ix} + \frac{1}{2}\sum_{i=3}^{4} g_i({Q_{ix}}^2 - {Q_{iy}}^2), \tag{3.58}$$

$$Z = \sum_{i=3}^{4}\kappa_i Q_{iy} - \sum_{i=3}^{4} g_i Q_{ix} Q_{iy}. \tag{3.59}$$

3.1.4 The $E \times e$ vibronic Hamiltonian with SO coupling for high-spin states

It is straightforward to derive the generalized JT-SO Hamiltonians for a ${}^M E$ state of a molecule with D_{3h} symmetry ($M = 3, 4, 5$). Let us consider a molecule with D_{3h} symmetry containing two unpaired electrons. The six spin-adapted non-relativistic two-electron basis functions for a ${}^3E$ state are

$$\begin{aligned} \psi_{\pm}^{(1)} &= |\Phi_A \alpha \Phi_{\pm} \alpha\rangle, \\ \psi_{\pm}^{(0)} &= \frac{1}{\sqrt{2}}[|\Phi_A \alpha \Phi_{\pm} \beta\rangle + |\Phi_A \beta \Phi_{\pm} \alpha\rangle], \\ \psi_{\pm}^{(-1)} &= |\Phi_A \beta \Phi_{\pm} \beta\rangle. \end{aligned} \tag{3.60}$$

Here Φ_A and $\Phi_{\pm}$ are the molecular orbitals and α, β are the spin-orbitals. These orthonormal basis functions are eigenfunctions of S^2 with eigenvalue 2 and of S_z with eigenvalues $0, \pm 1$.
Using these six diabatic two-electron basis functions and expanding H_{es} and H_{SO} in a Taylor series in powers of normal-mode displacements, the 6×6 ${}^3E \times e$ JT-SO Hamiltonian considering a single vibrational mode of e symmetry is[30]

$$H_{JTSO} = (T_N + \frac{1}{2}\omega\rho^2) I_6 + I_3 \otimes \gamma_c + A_3 \otimes \sigma_z, \tag{3.61}$$

where σ_z is one of the Pauli-spin matrices and

$$A_3 = \begin{pmatrix} \Delta_z & \delta e^{i\phi} & 0 \\ \delta e^{-i\phi} & 0 & \delta e^{i\phi} \\ 0 & \delta e^{-i\phi} & -\Delta_z \end{pmatrix} \tag{3.62}$$

with

$$\delta = \sqrt{\Delta_x^2 + \Delta_y^2}, \tag{3.63}$$

and

$$\phi = tan^{-1}\left(\frac{\Delta_y}{\Delta_x}\right). \tag{3.64}$$

The calculation of the matrix elements of the JT-SO Hamiltonian is simplified by the existence of the three-fold symmetry axis, the time-reversal symmetry as well as the Hermiticity of the Hamiltonian. For D_{3h} symmetry, $\Delta_x = \Delta_y = 0$ and A_3 simplifies to

$$A_3 = \begin{pmatrix} \Delta_z & 0 & 0 \\ 0 & 0 & 0 \\ 0 & 0 & -\Delta_z \end{pmatrix}. \tag{3.65}$$

For a molecule with three unpaired electrons in the molecular orbitals $\Phi_{\pm}$, Φ_{A_1}, Φ_{A_2},

the diabatic non-relativistic electronic basis functions are

$$\psi_{\pm}^{(3/2)} = |\Phi_{A_1}\alpha\Phi_{A_2}\alpha\Phi_{\pm}\alpha\rangle,$$

$$\psi_{\pm}^{(1/2)} = \frac{1}{\sqrt{3}}[|\Phi_{A_1}\alpha\Phi_{A_2}\alpha\Phi_{\pm}\beta\rangle + |\Phi_{A_1}\alpha\Phi_{A_2}\beta\Phi_{\pm}\alpha\rangle + |\Phi_{A_1}\beta\Phi_{A_2}\alpha\Phi_{\pm}\alpha\rangle], \tag{3.66}$$

$$\psi_{\pm}^{(-1/2)} = \frac{1}{\sqrt{3}}[|\Phi_{A_1}\alpha\Phi_{A_2}\beta\Phi_{\pm}\beta\rangle + |\Phi_{A_1}\beta\Phi_{A_2}\alpha\Phi_{\pm}\beta\rangle + |\Phi_{A_1}\beta\Phi_{A_2}\beta\Phi_{\pm}\alpha\rangle],$$

$$\psi_{\pm}^{(-3/2)} = |\Phi_{A_1}\beta\Phi_{A_2}\beta\Phi_{\pm}\beta\rangle.$$

They are eigenfunctions of S^2 with eigenvalue $\frac{15}{4}$ and of S_z with eigenvalues $\pm\frac{1}{2}$, $\pm\frac{3}{2}$.

Using these eight diabatic three-electron basis functions, expanding the H_{es} and H_{SO} in Taylor series and calculating the matrix elements by making use of the three-fold symmetry of the system, the time-reversal symmetry as well as the Hermiticity of the Hamiltonian, the ${}^4E \times e$ JT-SO Hamiltonian is obtained[30]

$$H_{JTSO} = (T_N + \frac{1}{2}\omega\rho^2)I_8 + I_4 \otimes \gamma_c + A_4 \otimes \sigma_z, \tag{3.67}$$

with

$$A_4 = \begin{pmatrix} \Delta_z^{(2)} & \delta_2 e^{i\phi_2} & 0 & 0 \\ \delta_2 e^{-i\phi_2} & \Delta_z^{(1)} & \delta_1 e^{i\phi_1} & 0 \\ 0 & \delta_1 e^{-i\phi_1} & -\Delta_z^{(1)} & \delta_2 e^{i\phi_2} \\ 0 & 0 & \delta_2 e^{-i\phi_2} & -\Delta_z^{(2)} \end{pmatrix}, \tag{3.68}$$

where $\Delta_z^{(1)}$ and $\Delta_z^{(2)}$ are real-valued matrix elements of SO operator and $\delta_k, \phi_k = 1, 2$ are defined in analogy to Eqs. (3.63, 3.64). Eq. (3.68) simplifies, in case of molecules with D_{3h} symmetry, to

$$A_4 = \begin{pmatrix} \Delta_z^{(2)} & 0 & 0 & 0 \\ 0 & \Delta_z^{(1)} & 0 & 0 \\ 0 & 0 & -\Delta_z^{(1)} & 0 \\ 0 & 0 & 0 & -\Delta_z^{(2)} \end{pmatrix}, \tag{3.69}$$

where the relation between $\Delta_z^{(2)}$ and $\Delta_z^{(1)}$ is

$$\Delta_z^{(2)} = 3\Delta_z^{(1)}. \tag{3.70}$$

The orthonormal, spin-adapted non-relativistic electronic basis functions for a system with four unpaired electrons in molecular orbitals $\Phi_{\pm}$, Φ_{A_1}, Φ_{A_2}, Φ_{A_3} (constructed in the similar way as for $M = 2, 3, 4$), are eigenfunctions of S^2 with eigenvalue 6 and of S_z with eigenvalues $0, \pm 1, \pm 2$. Using the ten diabatic four-electron basis functions, expanding the H_{es} and H_{SO} in Taylor series and calculating the matrix elements by making use of the three-fold symmetry of the system, the time-reversal symmetry as well as the Hermiticity

of the Hamiltonian, the 10×10 ${}^5E \times e$ JT-SO Hamiltonian is obtained[30]

$$H_{JTSO} = (T_N + \frac{1}{2}\omega\rho^2)I_{10} + I_5 \otimes \gamma_c + A_5 \otimes \sigma_z \tag{3.71}$$

where

$$H_{SO} = \begin{pmatrix} \Delta_z^{(2)} & \delta_2 e^{i\phi_2} & 0 & 0 & 0 \\ \delta_2 e^{-i\phi_2} & \Delta_z^{(1)} & \delta_1 e^{i\phi_1} & 0 & 0 \\ 0 & \delta_1 e^{-i\phi_1} & 0 & \delta_1 e^{i\phi_1} & 0 \\ 0 & 0 & \delta_1 e^{-i\phi_1} & -\Delta_z^{(1)} & \delta_2 e^{i\phi_2} \\ 0 & 0 & 0 & \delta_2 e^{-i\phi_2} & -\Delta_z^{(2)} \end{pmatrix}. \tag{3.72}$$

In case of molecules with D_{3h} symmetry A_5 simplifies to

$$A_5 = \begin{pmatrix} \Delta_z^{(2)} & 0 & 0 & 0 & 0 \\ 0 & \Delta_z^{(1)} & 0 & 0 & 0 \\ 0 & 0 & 0 & 0 & 0 \\ 0 & 0 & 0 & -\Delta_z^{(1)} & 0 \\ 0 & 0 & 0 & 0 & -\Delta_z^{(2)} \end{pmatrix}. \tag{3.73}$$

where the relation between $\Delta_z^{(2)}$ and $\Delta_z^{(1)}$ is

$$\Delta_z^{(2)} = 2\Delta_z^{(1)} \tag{3.74}$$

The generalized form of a two-mode ${}^M E \times e$ JT-SO Hamiltonian ($M = 2, 3, 4, 5 \ldots$) is written in the complex representation as[30]

$$H_{JTSO} = \sum_{i=3}^{4}(T_{iN} + \frac{1}{2}\omega_i\rho_i^2)I_{2M} + I_M \otimes \gamma_c + A_M \otimes \sigma_z \tag{3.75}$$

In real representation, the same is written as

$$H_{JTSO} = \sum_{i=3}^{4}(-\frac{1}{2}\omega_i(\frac{\partial^2}{\partial Q_{ix}^2} + \frac{\partial^2}{\partial Q_{iy}^2}) + \frac{1}{2}\omega_i(Q_{ix}^2 + Q_{iy}^2))I_{2M} + I_M \otimes \gamma_r + A_M \otimes \sigma_y. \tag{3.76}$$

The general BP SO operators A_M (in Eqs. (3.62, 3.68, 3.72) can easily be block-diagonalized by a unitary transformation which does not dependent on the nuclear coordinates, as discussed before.[30]

The adiabatic PE functions are obtained by diagonalizing the electronic Hamiltonian H_e (excluding the kinetic energy part of H_{JTSO}). The adiabatic PE functions in the real representation for electronic states with different spin multiplicities are given below.

For $M = 2$:

$$V_{1,2} = \frac{1}{2}\sum_{i=3}^{4}\omega_i({Q_{ix}}^2 + {Q_{iy}}^2) - \sqrt{\Delta^2 + W^2 + Z^2} \tag{3.77}$$

$$V_{3,4} = \frac{1}{2}\sum_{i=3}^{4}\omega_i({Q_{ix}}^2 + {Q_{iy}}^2) + \sqrt{\Delta^2 + W^2 + Z^2}. \tag{3.78}$$

For $M = 3$:

$$V_{1,2} = \frac{1}{2}\sum_{i=3}^{4}\omega_i({Q_{ix}}^2 + {Q_{iy}}^2) - \sqrt{\Delta^2 + W^2 + Z^2} \tag{3.79}$$

$$V_3 = \frac{1}{2}\sum_{i=3}^{4}\omega_i({Q_{ix}}^2 + {Q_{iy}}^2) - \sqrt{W^2 + Z^2} \tag{3.80}$$

$$V_4 = \frac{1}{2}\sum_{i=3}^{4}\omega_i({Q_{ix}}^2 + {Q_{iy}}^2) + \sqrt{W^2 + Z^2} \tag{3.81}$$

$$V_{5,6} = \frac{1}{2}\sum_{i=3}^{4}\omega_i({Q_{ix}}^2 + {Q_{iy}}^2) + \sqrt{\Delta^2 + W^2 + Z^2}. \tag{3.82}$$

For $M = 4$:

$$V_{1,2} = \frac{1}{2}\sum_{i=3}^{4}\omega_i({Q_{ix}}^2 + {Q_{iy}}^2) - \sqrt{9\Delta^2 + W^2 + Z^2} \tag{3.83}$$

$$V_{3,4} = \frac{1}{2}\sum_{i=3}^{4}\omega_i({Q_{ix}}^2 + {Q_{iy}}^2) - \sqrt{\Delta^2 + W^2 + Z^2} \tag{3.84}$$

$$V_{5,6} = \frac{1}{2}\sum_{i=3}^{4}\omega_i({Q_{ix}}^2 + {Q_{iy}}^2) + \sqrt{\Delta^2 + W^2 + Z^2} \tag{3.85}$$

$$V_{7,8} = \frac{1}{2}\sum_{i=3}^{4}\omega_i({Q_{ix}}^2 + {Q_{iy}}^2) + \sqrt{9\Delta^2 + W^2 + Z^2}. \tag{3.86}$$

For $M = 5$,

$$V_{1,2} = \frac{1}{2}\sum_{i=3}^{4}\omega_i({Q_{ix}}^2 + {Q_{iy}}^2) - \sqrt{4\Delta^2 + W^2 + Z^2} \tag{3.87}$$

$$V_{3,4} = \frac{1}{2}\sum_{i=3}^{4}\omega_i({Q_{ix}}^2 + {Q_{iy}}^2) - \sqrt{\Delta^2 + W^2 + Z^2} \tag{3.88}$$

$$V_5 = \frac{1}{2}\sum_{i=3}^{4}\omega_i({Q_{ix}}^2 + {Q_{iy}}^2) - \sqrt{W^2 + Z^2} \tag{3.89}$$

$$V_6 = \frac{1}{2}\sum_{i=3}^{4}\omega_i({Q_{ix}}^2 + {Q_{iy}}^2) + \sqrt{W^2 + Z^2} \tag{3.90}$$

$$V_{7,8} = \frac{1}{2}\sum_{i=3}^{4}\omega_i({Q_{ix}}^2 + {Q_{iy}}^2) + \sqrt{\Delta^2 + W^2 + Z^2} \tag{3.91}$$

$$V_{9,10} = \frac{1}{2}\sum_{i=3}^{4}\omega_i({Q_{ix}}^2 + {Q_{iy}}^2) + \sqrt{4\Delta^2 + W^2 + Z^2}. \tag{3.92}$$

It is noticed that SO coupling lifts the degeneracy of the potentials at the reference geometry of D_{3h} symmetry (that is, $Q_{ix} = Q_{iy} = 0$). For $M = 2$, the degeneracy of the potentials is lifted by the SO splitting 2Δ. For $M = 4$, the degeneracy of the potentials is lifted by the SO splittings 2Δ and 6Δ, respectively. Each of these SO-split potentials is two-fold degenerate (Kramers degeneracy). It is seen that the adiabatic potentials V_3, V_4 for $M = 3$ and V_5, V_6 for $M = 5$ are unaffected by the SO coupling, while the degeneracies of the remaining potentials at $Q_{ix} = Q_{iy} = 0$ are lifted by SO splittings (2Δ for $M = 3$ and 2Δ and 4Δ, respectively, for $M = 5$). The remaining degeneracies ($V_1 = V_2$, etc.) apply for an isolated ${}^M E$ state where $M = 3, 5$. These degeneracies can be lifted by SO configuration interaction with other electronic states.

3.2 Symmetry-adapted nuclear-displacement coordinates and dimensionless normal coordinates for XY_3 molecules

The transition-metal trifluorides MF_3 (M = Ti, Cr, Mn, Co, Ni), considered in this work, are planar trigonal molecules with D_{3h} symmetry. The three F atoms are labeled 1, 2 and 3 in a clockwise manner and the metal atom at the centre is atom 4. The bond angles are denoted as α_1, α_2 and α_3. The bond lengths are labeled as r_{i4} ($i = 1, 2, 3$).

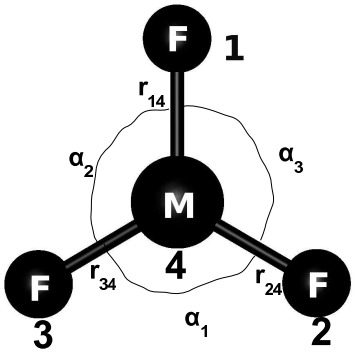

The six symmetry-adapted nuclear-displacement coordinates are the totally symmetric stretching mode a_1', the symmetric bending umbrella mode a_2'', the asymmetric doubly degenerate stretching mode and the asymmetric doubly degenerate bending mode of e' symmetry. The five symmetry-adapted coordinates in terms of internal streching and bending coordinates for trigonal planar molecule of D_{3h} symmetry are defined as follows[6]

$$S_1 = \frac{1}{\sqrt{3}}(\Delta r_{14} + \Delta r_{34} + \Delta r_{24}) \tag{3.93a}$$

$$S_{3x} = \frac{1}{\sqrt{6}}(2\Delta r_{14} - \Delta r_{24} - \Delta r_{34}) \tag{3.93b}$$

$$S_{3y} = \frac{1}{\sqrt{2}}(\Delta r_{24} - \Delta r_{34}) \tag{3.93c}$$

$$S_{4x} = \frac{1}{\sqrt{6}}R(2\Delta\alpha_1 - \Delta\alpha_2 - \Delta\alpha_3) \tag{3.93d}$$

$$S_{4y} = \frac{1}{\sqrt{2}}R(\Delta\alpha_2 - \Delta\alpha_3) \tag{3.93e}$$

where R is the M-F equilibrium distance and Δr_{i4} and $\Delta\alpha_i$ are displacements of internal bond distances and bond angles, respectively. Displacements along S_{3x} or S_{4x} preserve C_{2v} symmetry, whereas distortions along S_{3y} or S_{4y} lead to structures with C_s symmetry.

While symmetry coordinates are useful for the representation of PE surface, the calculation of spectra is simpler with normal coordinates, as the KEO is diagonal in normal coordinates. Normal coordinates are linear combinations of the symmetry-adapted coordinates. The transformation from symmetry coordinates to dimensionless normal coordinates is[78]

$$Q = \left(\frac{2\pi\omega c}{\hbar}\right)^{\frac{1}{2}} L^{-1} S \tag{3.94}$$

where Q is the vector of dimensionless normal coordinates and S is the vector of symmetry coordinates. L is the transformation matrix of Wilson's FG matrix method.[78] Vibrational frequencies are calculated using the FG matrix method. The detailed derivation is given in Appendix B.

3.3 Calculation of external vibronic spectra using the time-independent method

The vibronic spectra have been calculated by solving the time-independent Schrödinger equation for the JT-SO Hamiltonian H. The initial and final vibronic wave functions $|\Psi_i\rangle$ and $|\Psi_f\rangle$ are expanded in a basis set, which is constructed as the product of electronic ($|\psi_+\rangle$,$|\psi_-\rangle$) and vibrational ($|n,l\rangle$) basis functions considering a single mode of e symmetry[79]

$$|\Psi_i\rangle = \sum_{n,l}(C^i_{+,n,l}|\psi_+\rangle|nl\rangle + C^i_{-,n,l}|\psi_-\rangle|nl\rangle) \tag{3.95}$$

$$|\Psi_f\rangle = \sum_{n,l}(C^f_{+,n,l}|\psi_+\rangle|nl\rangle + C^f_{-,n,l}|\psi_-\rangle|nl\rangle). \tag{3.96}$$

Here $|\psi_\pm\rangle = |\psi_x\rangle \pm i|\psi_y\rangle$ and the $|n,l\rangle$ are the eigenfunctions of the two-dimensional isotropic harmonic oscillator ($n = 0, 1, 2\ldots$, $l = -n, -n+2, \ldots, n-2, n$).

The expansion of the initial and the final vibronic states is done in complex (electronic) and polar (vibrational) basis sets. This representation is useful especially when the electronic spectra are calculated for linear or linear-plus quadratic JT Hamiltonians. An alternative representation is the real (ψ_x, ψ_y) representation, where the initial and

final JT eigenstates are represented as (considering single e mode)

$$|\Psi_i\rangle = \sum_{v_x,v_y} (C^i_{x,v_x,v_y}|\psi_x\rangle|v_x\rangle|v_y\rangle + C^i_{y,v_x,v_y}|\psi_y\rangle|v_x\rangle|v_y\rangle) \tag{3.97}$$

$$|\Psi_f\rangle = \sum_{v_{x'},v_{y'}} (C^f_{x,v_{x'},v_{y'}}|\psi_x\rangle|v_{x'}\rangle|v_{y'}\rangle + C^f_{y,v_{x'},v_{y'}}|\psi_y\rangle|v_{x'}\rangle|v_{y'}\rangle). \tag{3.98}$$

Here $|\psi_x\rangle$, $|\psi_y\rangle$ are electronic basis function in real representation and $|v_x\rangle|v_y\rangle$ are vibrational basis functions of two-dimensional harmonic oscillator in x, y representation.

The Hamiltonian matrix (in polar representation) is constructed using the following vibrational selection rules[79]

$$\langle n,l|\rho e^{i\phi}|n+1,l-1\rangle = \langle n+1,l-1|\rho e^{-i\phi}|n,l\rangle = \sqrt{\frac{1}{2}(n-l+2)} \tag{3.99}$$

$$\langle n,l|\rho e^{-i\phi}|n+1,l+1\rangle = \langle n+1,l+1|\rho e^{i\phi}|n,l\rangle = \sqrt{\frac{1}{2}(n+l+2)}. \tag{3.100}$$

For linear JT coupling, there exists a vibronic angular-momentum operator J which commutes with the JT Hamiltonian.[79] The eigenvalues j of J are thus good quantum numbers. In this case, the Hamiltonian matrix is constructed and diagonalized for each value of j. Assuming a nondegenerate and vibrationless initial state, the selection rule is $j = \pm\frac{1}{2}$, that is, only vibronic levels with $j = \pm\frac{1}{2}$ carry intensity.[79] The SO splitting Δ enters in the diagonal part of the Hamiltonian matrix, see Eq. (3.48).

For linear-plus-quadratic JT coupling, j is not a good quantum number. In this case, Hamiltonian matrix for all possible j values has to be constructed and diagonalized. In the linear-plus-quadratic approximation, the selection rule is $j = \pm\frac{1}{2} mod(3)$.[73]

The matrix elements of the JT Hamiltonian in real representation are calculated using the following vibrational selection rules

$$\langle v_{x'}|Q_x|v_x\rangle = \frac{1}{\sqrt{2}}\left(\sqrt{v_x+1}\delta_{v_{x'},v_x+1} + \sqrt{v_x}\delta_{v_{x'},v_x-1}\right) \tag{3.101}$$

$$\langle v_{y'}|Q_y|v_y\rangle = \frac{1}{\sqrt{2}}\left(\sqrt{v_y+1}\delta_{v_{y'},v_y+1} + \sqrt{v_y}\delta_{v_{y'},v_y-1}\right). \tag{3.102}$$

Since the Hamiltonian matrix is constructed without exploiting the D_{3h} symmetry, number of vibrational basis functions needed for a converged spectrum in this case is larger than in the case of the polar representation. The vibrational frequencies and normal modes of the nondegenerate initial state are assumed to be the same as the vibrational frequencies and normal modes of the degenerate JT-active state of interest.

Using these expansions, the elements of the Hamiltonian matrix are computed and diagonalized explicitly with a standard diagonalization method for real-symmetric matrices. The vibrational basis is increased until convergence and the desired accuracy is achieved. The eigenvalues represent the vibronic energy levels and the intensities are obtained from the square of the first component of each eigenvector, assuming that the molecule is initially in its vibrational ground state. The spectral intensity is plotted as a function of the energy of the final vibronic state.

3.4 Calculation of external vibronic spectra using the Chebyshev wave-packet propagation method

Higher-order JT couplings, and multimode JT effects are ignored in the calculation of vibronic spectra using time-independent approach, as the inclusion of these effects increases the computational cost drastically, making the achievement of convergence almost impossible. A time-dependent wave-packet propagation based approach is used to calculate the vibronic spectra including the higher-order JT coupling and two-mode JT effects.

In the time-dependent approach, the target function is the autocorrelation function which is defined as

$$C(t) = \langle \Psi(Q,0) | \Psi(Q,t) \rangle = C(-t). \tag{3.103}$$

where the final wavefunction at time t, $\Psi(Q,t)$ is obtained by the operation of the evolution operator $U(t,0)$ on the initial wavefunction $\Psi(Q,0)$. The simplest scheme for propagating the wavefunction in Eq.(2.31) is to expand the evolution operator in a Taylor series. The numerical scheme based on this approach is not stable, because it does not conserve time-reversal symmetry of the Schrödinger equation. A better solution is the explicit second-order differencing (SOD) scheme, i.e.

$$\Psi(t+\tau) = \Psi(t-\tau) - 2i\tau\hat{H}\Psi(t) \tag{3.104}$$

which is also the time-propagation scheme used in the finite difference method. To overcome the error accumulation in the phase (which restricts the accuracy), a new propagation scheme was introduced by Tal-Ezer and Kosloff[71] in which the evolution operator is expanded in a Chebyshev series

$$e^{(-i\hat{H}t)} \approx \sum_{k=0}^{N} a_k \phi_k(-i\hat{H}t), \tag{3.105}$$

where the a_k are expansion coeeficients and the ϕ_k are the complex Chebyshev polynomials. A mapping of $H \to H_s$ is needed to normalize the Hamiltonian so that the spectrum (i.e. the range of possible eigenvalues it can give) is limited in the range of [-1, 1]. The mapping is given by[72]

$$\hat{H_s} = \frac{\hat{H} - (\Delta E/2 + V_{min})\hat{\mathbf{I}}}{\Delta E/2}, \tag{3.106}$$

where ΔE, the range of Hamiltonian operator, is

$$\Delta E = E_{max} - E_{min}, \tag{3.107}$$

and $V_{min} \leq E_{min}$. In this mapping, the Chebyshev series can be explicitly rewritten as

$$e^{(-i\hat{H}t)} = e^{-i(\Delta E/2 + V_{min})t} \sum_{k=0}^{N} (2 - \delta_{0k}) J_k \left(\frac{\Delta E t}{2}\right) \phi_k(-i\hat{H_s}). \tag{3.108}$$

The ϕ_k obey the recursion formula

$$\phi_{k+1} = -2i\hat{H}_s\phi_k + \phi_{k-1} \tag{3.109}$$

The propagated wavefunction Ψ_k is given by

$$\Psi_k = \phi_k(-i\hat{H}_s)\Psi(t=0). \tag{3.110}$$

The Ψ_k obey the same recursion relation as ϕ_k, i.e.

$$\Psi_{k+1} = -2i\hat{H}_s\Psi_k + \Psi_{k-1}. \tag{3.111}$$

If the initial wavefunction is real and Hermitian symmetry is taken into account, the complete propagation can be performed in real number space (as the Hamiltonian matrix is real and symmetric)

$$\begin{aligned} C(t) &= \frac{1}{2}(\langle\Psi(x,0)|\Psi(x,t)\rangle + \langle\Psi(x,0)|\Psi(x,-t)\rangle) && (3.112)\\ &= \frac{1}{2}(\langle\Psi(x,0)|e^{(-i\hat{H}t)} + e^{i\hat{H}t}|\Psi(x,0)\rangle) && (3.113)\\ &= (\langle\Psi(x,0)|\cos(\hat{H}t)|\Psi(x,0)\rangle). && (3.114) \end{aligned}$$

As the cosine operator is just the real part of the exponential time-evolution operator and one can perform the propagation of an initially real wave-packet using only real arithmetic, the propagation scheme is known as the real wave-packet method.[72] The iterative procedure

$$\Psi(t+\tau) = 2\cos(\hat{H}\tau)\Psi(t) - \Psi(t-\tau) \tag{3.115}$$

involves the operation of cosine of $\hat{H}$ on the wavepacket, which is costly to perform. A mapping is introduced to overcome this problem in the real wavepacket method

$$f(\hat{H}_s) = -\frac{1}{\tau}\cos^{-1}(\hat{H}_s) \tag{3.116}$$

where $\hat{H}_s$ is the shifted Hamiltonian defined in Eq. (3.106). Under this map (Eq. (3.116)), the discretized cosine operator $\cos(Hk\tau)$ $(t \to k\tau)$ is equivalent to the definition of the series of Chebyshev polynomials

$$T_k(\hat{H}_s) = \cos(k\cos^{-1}(\hat{H}_s)) \tag{3.117}$$

and the propagated wavefunction can be written as

$$\Psi_k = T_k(\hat{H}_s)\Psi_0;\ k = 0, 1, \ldots. \tag{3.118}$$

Using the following recursion relation of Chebyshev polynomials

$$T_k(H_s) = 2H_sT_{k-1}(H_s) - T_{k-2}(H_s), \tag{3.119}$$

Eq.(3.118) takes the form

$$\Psi_k = 2H_s\Psi_{k-1} - \Psi_{k-2} \tag{3.120}$$

and the autocorrelation function can be written as

$$C_k = \langle\Psi_0|T_k(H_s)|\Psi_0\rangle. \tag{3.121}$$

A modified TDSE

$$i\frac{\partial\Psi_f(x,t)}{\partial t} = f(\hat{H}_s)\Psi_f(x,t) \tag{3.122}$$

is then solved instead of solving the actual TDSE. The iterative equation leads to the following simplified equation

$$\Psi_f(t+\tau) = 2\hat{H}_s\psi_f(t) - \Psi_f(t-\tau). \tag{3.123}$$

The Hamiltonian employed in the propagations is defined in terms of mass-weighted normal coordinates

$$H = -\frac{1}{2}\sum_{i=1}^{n}\frac{\partial^2}{\partial q_i^2} + V(q_1, q_2, \ldots, q_n) \tag{3.124}$$

where n is the number of nuclear degrees of freedom and should be limited to $n \leq 5$ to calculate the autocorrelation function effectively. The matrix $V(q_1, q_2, \ldots, q_n)$ is a function of n nuclear coordinates and represents the PE operator in mass-weighted normal coordinates. A discrete variable representation (DVR) grid is used to construct the Hamiltonian. As interpolating primitive basis functions, Whittaker's Cardinal $(\mathrm{sinc}(x))$[70] function on an equidistant grid is used. The grid is a tensor grid of all considered degrees of freedom. The matrix elements of the simple and sparse KEO,[70] in this grid representation, are given by

$$T^{(i)}_{j,j+k} = \begin{cases} -\frac{1}{6}\left(\frac{\pi}{\Delta q_i}\right)^2 & k = 0 \\ -\frac{(-1)^k}{(k\Delta q_i)^2} & k \neq 0. \end{cases} \tag{3.125}$$

A $m \times m$ KE matrix is obtained for each degrees of freedom where m is the number of grid points along the coordinates q_i with the interval of Δq_i. The HEG (Harris, Engerholm and Gwinn) contraction scheme[80] has been used to optimize the grid in each coordinate. The primitive initial grid was reduced by an energy cut-off criterion.[81] The energy cut-off for each one-dimensional subproblem is higher than the maximum energy eigenvalue in the final spectrum. The KEO matrix T is constructed on the fly during the Chebyshev iteration, referencing only the nonzero elements. The PE matrix is constructed using the standard LAPACK[82] packed storage format.

In case of JT-SO Hamiltonian, the method needs to be extended as the model SO Hamiltonian contains complex-valued matrix elements in the real-valued basis representation.[83] The extended real Chebyshev propagator for complex Hamiltonian is discussed in Appendix D.

The time-dependent autocorrelation function is given by

$$C(t) = e^{-i(\Delta E/2+V_{min})t} \sum_{k=0}^{N} (2-\delta_{0k})(-i)^k J_k(\frac{\Delta E t}{2}) C_k \tag{3.126}$$

where J_k is the k-th Bessel function of the first kind[71] and C_k is the k-th Chebyshev autocorrelation function obtained from Eq. (3.121).

The spectrum is obtained as the Fourier transformation of the time-dependent autoaorrelation function. In this work, the spectral intensity is convoluted with a Gaussian function with full width at half maximum (FWHM) of 0.5 meV and 10 meV, to obtain "high-resolution" and "low-resolution", respectively. As is known Fourier transformation of a Gaussian function also is a Gaussian function, the convolution is done in the time domain.

3.5 Calculation of internal vibronic spectra using the time-independent method

Nonzero intensitites in vibronic IR spectra are possible only for molecules in which the JT-active modes are dipolar active, i.e., when there is a change of the dipole moment along the JT-active mode. These type of molecular systems are called 'dipolar-unstable polyatomic systems'.[6] In case of a JT-active E state, two types of dipole moment exist i.e. the pure vibrational dipole moments and the internal electronic transition dipole moment (transition moment between the two components of the E state).

When simulating IR spectra, it is necessary to consider finite temperatures, since the vibronic level spacings are very small and higher levels are populated even at low temperatures.

The internal vibronic spectrum is calculated using the Fermi-Golden rule[66]

$$I_f = \sum_i p_i |\langle \Psi_f | \hat{H'} | \Psi_i \rangle|^2 \delta(E_f - E_i - \omega) \tag{3.127}$$

where p_i is the statistical weight factor defined as

$$p_i = g_i \frac{e^{-\frac{E_i}{k_B T}}}{Z} \tag{3.128}$$

with g_i , E_i, k_B, T and Z as the degeneracy factor, the energy eigenvalue of the initial state, the Boltzmann constant, the temperature of the system and the partition function, respectively. If temperature is zero, only the ground vibrational state is populated and thus p_i is $\delta_{i,0}$. Ψ_i and Ψ_f are the initial and final vibronic states, respectively and $\hat{H'}$ is the interaction Hamiltonian described as

$$\hat{H'} = \vec{e}\vec{\mu}. \tag{3.129}$$

Here, $\vec{e}$ is the unit vector of the polarization of the electromagnetic wave. $\vec{\mu}$ can be separated as the vector of the dipole moment of the electrons ($\vec{\mu_e}$) and nuclei ($\vec{\mu_n}$) of the

polyatomic system, respectively[6]

$$\vec{\mu} = \vec{\mu}_e(r) + \vec{\mu}_n(Q). \tag{3.130}$$

In Condon approximation:

$$\vec{\mu}_e = \vec{\mu}_e^{(0)}. \tag{3.131}$$

Incorporating Eq. (3.129) into Eq. (3.127) and using Eqs. (3.130) and (3.131), we obtain

$$\begin{aligned} I_f &= \sum_i p_i |\langle \Psi_f | \vec{\mu}_e^{(0)} | \Psi_i \rangle \vec{e} + \langle \Psi_f | \vec{\mu}_n(Q) | \Psi_i \rangle \vec{e}|^2 \delta(E_f - E_i - \omega) \\ &= \sum_i p_i |(\vec{\mu}_e^{fi} + \vec{\mu}_n^{fi}) \vec{e}|^2 \delta(E_f - E_i - \omega) \end{aligned} \tag{3.132}$$

In principle, the dipole moment vector is composed of three components along x, y and z direction in three-dimensional space i.e.

$$\vec{\mu_e} = \begin{pmatrix} \mu_{ex} \\ \mu_{ey} \\ \mu_{ez} \end{pmatrix} \quad \vec{\mu_n} = \begin{pmatrix} \mu_{nx} \\ \mu_{ny} \\ \mu_{nz} \end{pmatrix} \tag{3.133}$$

As the transition-metal trifluorides of D_{3h} symmetry are in the xy plane, z-component of the dipole moment vector is zero. The unit vector of polarization of electric field can also be written in terms of three components as

$$\vec{e} = \begin{pmatrix} e_x \\ e_y \\ e_z \end{pmatrix}. \tag{3.134}$$

Here e_x, e_y and e_z are given as

$$e_x = \sin\theta\cos\phi; \quad e_y = \sin\theta\sin\phi; \quad e_z = \cos\theta \tag{3.135}$$

in three-dimensional space. Since the calculation is done in the molecular frame, the statistical averaging over all direction of unit vector of polarization $\vec{e}$

$$\langle e_\alpha e_\beta \rangle = \frac{1}{3}\delta_{\alpha\beta} \tag{3.136}$$

is used in Eq. 3.132 to obtain

$$I_f = \sum_i p_i |\mu_{ex}^{fi} e_x + \mu_{ey}^{fi} e_y + \mu_{nx}^{fi} e_x + \mu_{ny}^{fi} e_y|^2 \delta(E_f - E_i - \omega) \tag{3.137}$$

$$= \sum_i p_i \frac{1}{3} (|\mu_{ex}^{fi} + \mu_{nx}^{fi}|^2 + |\mu_{ey}^{fi} + \mu_{ny}^{fi}|^2) \delta(E_f - E_i - \omega) \tag{3.138}$$

The components of the dipole moment operators μ_{nx} and μ_{ny} are expanded in Taylor series along the JT-active vibrational modes Q_x and Q_y as

$$\begin{aligned}\mu_{nx} &= {\mu_{nx}}^{(0)} + \frac{\partial \mu_{nx}}{\partial Q_x} Q_x + \frac{\partial \mu_{nx}}{\partial Q_y} Q_y \\ &= \mu'_{nx,x} Q_x + \mu'_{nx,y} Q_y \quad ({\mu_{nx}}^{(0)} = 0 \text{ by symmetry})\end{aligned} \tag{3.139}$$

$$\begin{aligned}\mu_{ny} &= {\mu_{ny}}^{(0)} + \frac{\partial \mu_{ny}}{\partial Q_x} Q_x + \frac{\partial \mu_{ny}}{\partial Q_y} Q_y \\ &= \mu'_{ny,x} Q_x + \mu'_{ny,y} Q_y \quad ({\mu_{ny}}^{(0)} = 0 \text{ by symmetry})\end{aligned} \tag{3.140}$$

Matrix elements of nuclear dipole moment operators with electronic basis functions are

$$\langle \psi_x | \left(\mu'_{nx,x} Q_x + \mu'_{nx,y} Q_y \right) | \psi_x \rangle = \left(\mu'_{nx,x,xx} Q_x + \mu'_{nx,y,xx} Q_y \right) \tag{3.141}$$

$$\langle \psi_y | \left(\mu'_{nx,x} Q_x + \mu'_{nx,y} Q_y \right) | \psi_y \rangle = \left(\mu'_{nx,x,yy} Q_x + \mu'_{nx,y,yy} Q_y \right) \tag{3.142}$$

$$\langle \psi_x | \left(\mu'_{ny,x} Q_x + \mu'_{ny,y} Q_y \right) | \psi_y \rangle = \left(\mu'_{ny,x,xy} Q_x + \mu'_{ny,y,xy} Q_y \right) \tag{3.143}$$

$$\langle \psi_y | \left(\mu'_{ny,x} Q_x + \mu'_{ny,y} Q_y \right) | \psi_x \rangle = \left(\mu'_{ny,x,yx} Q_x + \mu'_{ny,y,yx} Q_y \right). \tag{3.144}$$

Since the expansions of μ_{ey}^{fi} and μ_{ny}^{fi} in vibronic basisfunctions are similar to that of the μ_{ex}^{fi} and μ_{nx}^{fi}, respectively, the expansions of only μ_{ex}^{fi} and μ_{nx}^{fi} in vibronic basisfunctions are discussed in Appendix E. The vector components $C^{*f}_{x,v_{x'},v_y}$ and C^{i}_{x,v_x,v_y} in Eqs. (F.2, F.5) are the components of the eigenvector obtained by the diagonalization of the JT (or JT-SO) Hamiltonian discussed in Section 3.3.

The resulting stick spectrum is convoluted with a Lorentzian function with a FWHM of 8 meV to simulate a spectrum recorded with medium resolution.

For the calculation of internal vibronic spectra of electronic states with odd spin multiplicities (e.g. $M = 5$) with inclusion of SO coupling, two decoupled (split by SO coupling 4Δ and 2Δ, respectively) and one coupled (zero SO splitting) adiabatic PE surfaces are considered and solved individually and then the calculated intensities are superimposed. Since only the ground vibrational state of lowest adiabatic surface (surface corresponds to Eq. (3.87)) is initially populated at T = 0 K and the three SO-split adiabtaic surfaces are not coupled by dipole moment operator, transitions in and within the lowest adiabatic surface and its pair (surface correspond to Eq. (3.92)) are calculated to obtain the internal vibronic spectrum of ${}^5E''$ state at T = 0 K with inclusion of SO coupling. As temperature increases, apart from the ground vibrational state of the lowest adiabatic surface, the ground vibrational states of other two adiabatic surfaces (Eqs. (3.88) and (3.89)) are also initially populated. Therefore, transitions in and within each of the three adiabatic PE surfaces and their pairs (Eqs. (3.92), (3.91) and (3.90), respectively) contribute to the final spectrum.

In case of the calculation of internal vibronic spectra for states with even spin multiplicities (e.g. $M = 4$), transitions within two decoupled (by SO splittings 6Δ and 2Δ) adiabatic PE surfaces are considered. At T = 0 K, only the ground vibrational state of the lowest adiabatic surface (surface corresponds to Eq. (3.83)) is initially populated.

Chapter 4

Application to transition-metal trifluorides with even spin multiplicities

In this chapter, the details of the *ab initio* calculations, the PE surfaces, the JT and SO coupling parameters and the external vibronic spectra are discussed for the $^2E'$ and $^2E''$ states of TiF_3 and the $^4E'$ states of CrF_3 and NiF_3. For CrF_3 and NiF_3, the $^4E''$ states are excluded from the discussion as the results are less interesting due to weak JT coupling. The individual JT effects, the relevance of higher-order JT coupling parameters, and the two-mode JT effect are discussed in detail for the $^2E'$ state of TiF_3 and the $^4E'$ state of NiF_3 in order to explain the mechanisms giving rise to the rather complex vibronic spectra. For the remaining cases, the final electrostatic (spin-free) JT spectra are compared with the JT spectra including SO-coupling effects. The two non-JT-active modes (the totally symmetric stretching mode and the umbrella mode) are ignored in the calculation of the spectra. The possible pseudo-JT (PJT) couplings of the ^2E or ^4E states with each other or with other electronic states are also ignored.

4.1 Details of the *ab initio* electronic structure calculations

Ab initio electronic-structure calculations have been performed to determine the JT and SO coupling parameters. The PE surfaces of the low-lying excited states of TiF_3, CrF_3 and NiF_3 have been determined with the state-averaged complete-active-space self-consisted-field (CASSCF) method. The atomic natural orbital (ANO) basis set of Bauschlicher[84] was chosen for the Ti, Cr and Ni atoms, while Dunning's correlation-consistent polarized valence quadruple-zeta (cc-pVQZ) basis set[85] was used for F. All *ab initio* calculations have been performed in C_s symmetry.

The electronic configurations of the ground states of Ti^{3+}, Cr^{3+} and Ni^{3+} are $[Ar]3d^14s^0(^2D)$, $[Ar]3d^34s^0(^4D)$ and $[Ar]3d^74s^0$ (^4D), respectively, and the electronic configuration of F^- is $[He]2s^22p^6$ (^1S). The minimal active space includes 5 valence orbitals (the five $3d$-orbitals of the metal) with 1, 3 and 7 electron(s) for TiF_3, CrF_3 and NiF_3, respectively. The re-

molecule	state	active space	VEE (cm^{-1})	YP[a](cm^{-1})	relative CPU time
TiF_3	$^2E''$	(25,17)	2548		≈ 100
		(1,5)	2420	2260	≈ 1
	$^2E'$	(25,17)	17852		≈ 100
		(1,5)	17991	16260	≈ 1
CrF_3	$^4E'$	(27,17)	7770		≈ 18
		(3,5)	5437	4370	≈ 1
NiF_3	$^4E'$	(31,17)	8178		≈ 3
		(7,5)	7866	6670	≈ 1

Table 4.1: Comparison of active spaces, vertical electronic excitation energies and relative CPU times for the $^2E'$ and $^2E''$ states of TiF_3 and the $^4E'$ states of CrF_3 and NiF_3. [a]VEE by Yates and Pitzer[33]

maining 24 orbitals with 48 electrons were considered to be doubly-occupied core orbitals. To estimate the accuracy of these CASSCF data, calculations with a larger active space also have been performed. The large active space consists of 17 orbitals (five $3d$-orbitals on the metal atom as well as one $2s$ and three $2p$ orbitals on each of the F atoms).

The vertical excitation energies (VEE) (the difference between the energy of the excited ^ME state and the $^MA_1$ ground state at the equilibrium geometry of the latter) are collected in Table 4.1. The CASSCF results with the smaller active space are similar, but systematically higher, than the restricted open-shell Hartree-Fock (ROHF) results of Yates and Pitzer.[33] The only experimental result we are aware of is an ESR value of $\approx$ 2000 cm^{-1} for the $^2E''$ state of TiF_3.

For the $^2E'$ and $^2E''$ states of TiF_3 and the $^4E'$ state of NiF_3, the results obtained with the small and large active spaces are in reasonably good agreement. For the $^4E'$ state of CrF_3, on the other hand, the excitation energy is considerably more sensitive to the size of the active space. The larger active space yields a VEE which is higher by about 2300 cm^{-1}. In this case, also the deviation of the small-CAS excitation energy from the ROHF result of Yates and Pitzer is largest. These findings indicate that the electronic structure of CrF_3 may not be accurately described with the smaller active space.

The relative computation times of the CASSCF calculations also are indicated in Table 4.1. Since the costs of the large-CAS calculations are substantially higher (with the exception of NiF_3), the small active space have been chosen for the exploration of the JT PE surfaces. It has been verified that the values of the linear and quadratic JT couplings as well as the SO splittings are less sensitive to the size of the active space than the VEE.

The matrix elements of the SO operator have been computed at the CASSCF level using the full two-electron BP operator. All electronic-structure calculations have been performed using the MOLPRO program package.[86]

Dynamical electron-correlation effects were not included in the present work. This could be a topic of further studies, using the MRCI or CASPT2 methods. However, from *ab initio* calculations of vibrational or vibronic coupling constants for numerous systems, it is known that the energy gradients are less sensitive to dynamical electron-correlation effects than the VEE. For SO splittings, it is well known that they are little affected by dy-

namical electron-correlation effects, since SO coupling is primarily a one-electron operator.

4.2 Titanium trifluoride (TiF_3)

4.2.1 The $^2E'$ state

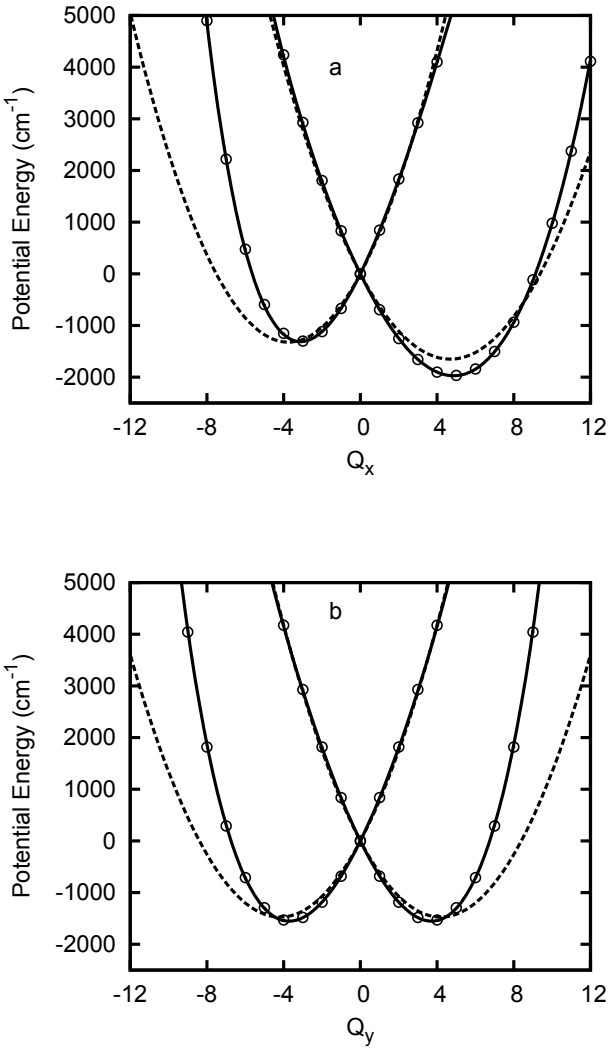

Figure 4.1: PE curves of the $^2E'$ electronic excited state of TiF_3 along the dimensionless bending normal coordinates Q_x (a) and Q_y (b). Circles correspond to *ab initio* data. The solid and dashed lines represent the fitted adiabatic potentials of the sixth-order and second-order JT model Hamiltonians, respectively.

Fig. 4.1 shows the PE curves of the $^2E'$ electronic excited state of TiF_3 along the

state	Δ (cm^{-1})	mode	ω (cm^{-1})	κ (cm^{-1})	g (cm^{-1})
$^2E'$	112.88	bending	151.635	758.468	20.929
		stretching	809.027	195.289	-23.541
$^2E''$	69.80	bending	179.267	396.068	-12.980
		stretching	766.237	493.566	-18.566

Table 4.2: SO and JT coupling parameters for the $^2E'$ and $^2E''$ states of TiF_3.

dimensionless bending normal coordinates Q_x (a) and Q_y (b). The circles correspond to *ab initio* data, while the dashed and solid lines are the PE functions of the second-order and sixth-order JT Hamiltonians, respectively, which have been fitted to the *ab initio* data. From Fig. 4.1a and b, it is clear that a JT expansion up to second order is not sufficient to describe the JT potential-energy functions along the bending mode of the $^2E'$ state of TiF_3, whereas the expansion up to sixth order results in an excellent fit to the *ab initio* data. The deviations of the second-order-fitted potentials from the sixth-order-fitted potentials in the large interval (from -12 to 12) reflect the breakdown of the validity of the second-order Taylor expansion in the larger interval of the bending modes Q_x and Q_y. The degeneracy of the $^2E'$ state is split substantially upon bending as the consequence of a very strong linear JT effect. The asymmetry of the two minima in Fig. 4.1a measures the strength of the quadratic JT coupling. Fig. 4.2 shows the PE curves of the $^2E'$ electronic excited state of TiF_3 along the dimensionless stretching normal coordinates Q_x (a) and Q_y (b). The circles correspond to *ab initio* data, while the solid lines are the PE functions of the fourth-order JT Hamiltonian, which have been fitted to the *ab initio* data (in this case, the fourth-order JT expansion is sufficient).

Fig. 4.3 shows the PE curves of the $^2E'$ state of TiF_3 along the dimensionless bending normal coordinate Q_x with inclusion of SO coupling. The symbols correspond to *ab initio* data and the solid lines are the PE functions of the sixth-order JT Hamiltonian including SO coupling. It is seen that the adiabatic PE functions of the model provide an excellent fit of the *ab initio* data over a large range of the bending normal mode.

The vibrational frequencies, the linear and quadratic JT coupling parameters of the bending and stretching modes, as well as the SO splittings are given in Table 4.2 for the $^2E'$ and $^2E''$ states of TiF_3. Details of the extraction of JT and SO coupling parameters using a least-squares fitting procedure are discussed in Appendix C. Higher-order fitting procedure is also described there. The anharmonicity constants and the higher-order JT coupling parameters are given in Tables 4.3 and 4.4, respectively.

It is seen that the dimensionless JT coupling parameters κ/ω and g/ω are much larger for the bending mode than for the stretching mode.

For TiF_3, the transitions from the nondegenerate electronic ground state to the $^2E'$ and $^2E''$ JT-active excited states are considered. For clarity, the vibronic spectra of the primarily JT-active bending mode alone are considered first. Figs. 4.4a and b show the external vibronic spectra of the $^2E'$ state obtained with the second-order and sixth-order JT Hamiltonians, respectively. The characteristic double-hump structure of the overall envelope of the spectrum reflects the existence of a strong first-order JT coupling. The main vibrational progression of the low-resolution spectra results from the strong linear

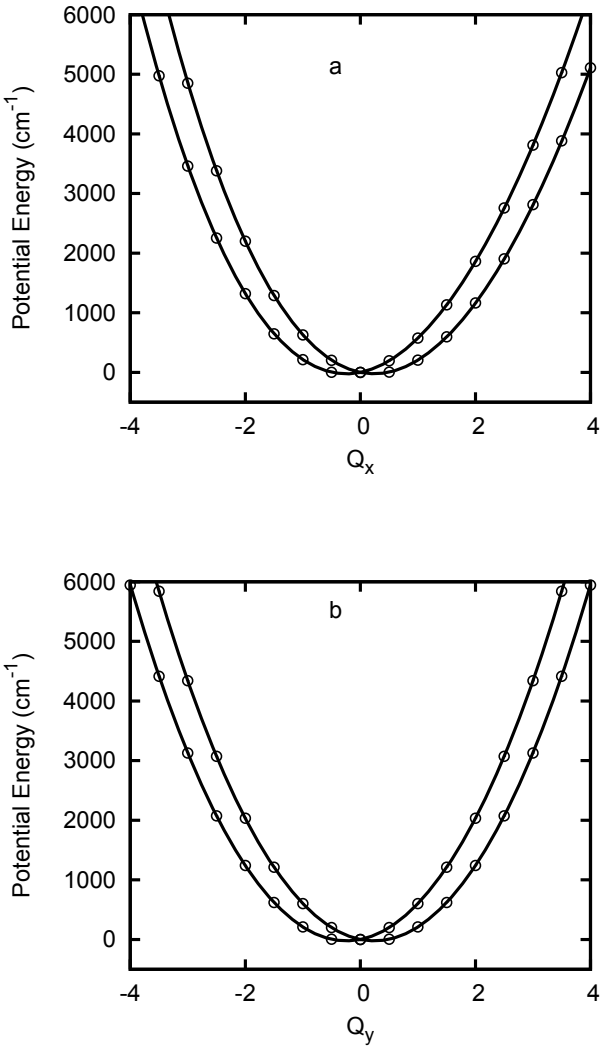

Figure 4.2: PE curves of the $^2E'$ electronic excited state of TiF_3 along the dimensionless stretching normal coordinates Q_x (a) and Q_y (b). Circles correspond to *ab initio* data. The solid lines represent the fitted adiabatic potentials of the fourth-order JT model Hamiltonian.

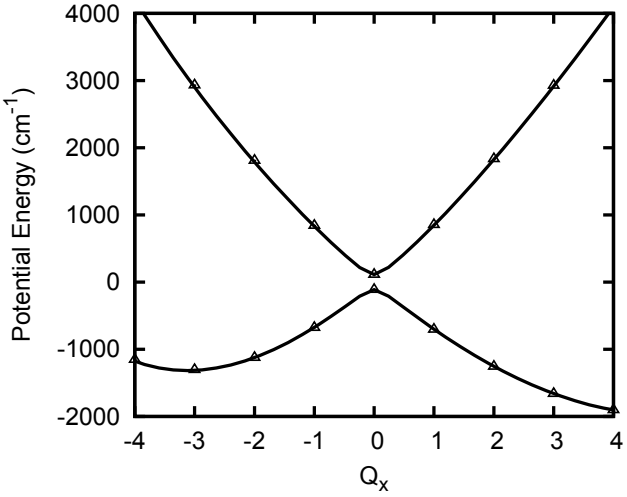

Figure 4.3: PE curves of the $^2E'$ state of TiF_3 along the dimensionless bending normal coordinate Q_x with inclusion of SO coupling. The symbols correspond to *ab initio* data and the solid lines are the PE functions of the sixth-order JT Hamiltonian including SO coupling.

Molecule	state	mode	${a_1}^{(3)}$	${a_1}^{(4)}$	${a_1}^{(5)}$	${a_1}^{(6)}$	${a_2}^{(6)}$
TiF_3	$^2E'$	bending	-8.374	8.098	-1.757	0.038	0.924
		stretching	-47.533	27.842	-	-	-
	$^2E''$	bending	-5.100	2.908	-1.295	0.044	0.868
		stretching	-47.993	32.075	-	-	-
CrF_3	$^4E'$	bending	-12.618	8.562	0.035	-0.092	-0.178
		stretching	-47.213	20.733	-	-	-
NiF_3	$^4E'$	bending	-4.802	7.489	-1.854	0.051	0.944
		stretching	-54.020	36.121	-	-	-

Table 4.3: Anharmonicity constants ${a_1}^{(n)}$, ${a_2}^{(n)}$ (in cm^{-1}) for the $^2E'$ and $^2E''$ states of TiF_3 and the $^4E'$ states of CrF_3 and NiF_3.

Molecule	state	mode	$\lambda_1^{(3)}$	$\lambda_1^{(4)}$	$\lambda_2^{(4)}$	$\lambda_1^{(5)}$	$\lambda_2^{(5)}$	$\lambda_1^{(6)}$	$\lambda_2^{(6)}$
TiF_3	$^2E'$	bending	-18.181	-4.396	3.188	0.408	0.053	0.647	-0.521
		stretching	2.882	-2.829	5.451	-	-	-	-
	$^2E''$	bending	-3.347	-0.126	0.272	-0.011	0.017	0.003	0.00
		stretching	7.631	-7.039	6.217	-	-	-	-
CrF_3	$^4E'$	bending	-19.779	7.458	-10.691	0.467	0.479	-0.719	0.873
		stretching	3.854	0.569	8.701	-	-	-	-
NiF_3	$^4E'$	bending	-8.803	-0.124	-1.205	-0.012	0.430	-0.010	0.0
		stretching	2.389	0.643	-1.237	-	-	-	-

Table 4.4: Higher-order JT coupling parameters $\lambda_1^{(n)}$, $\lambda_2^{(n)}$ (in cm^{-1}) for the $^2E'$ and $^2E''$ states of TiF_3 and the $^4E'$ states of CrF_3 and NiF_3.

JT coupling of the bending mode. The line splittings, which are clearly visible in the high-resolution spectra, are caused by the strong quadratic JT coupling.

The comparison of Figs. 4.4a, b shows that higher-order JT couplings have a significant effect both on the vibronic fine structure as well as on the envelope of the external vibronic spectrum. The envelope of the sixth-order spectrum is more structured and the lines of the high-resolution sixth-order spectrum are more clumped than in the second-order spectrum. The reason is the strong positive anharmonicity of the *ab initio* bending potentials, see Fig. 4.1. The latter arises from the "intramolecular collision" of neighbouring fluorine atoms at large amplitudes of the bending mode. The extension of the spectrum at the lower-energy edge due to inclusion of higher-order JT coupling parameters can be understood from Fig. 4.1. The stronger stabilization of the PE minima for the sixth-order JT Hamiltonian (solid line in Fig. 4.1) than for the second-order JT Hamiltonian (dashed line in Fig. 4.1) results in transitions at lower energies for the sixth-order Hamiltonian, as is seen in Figs. 4.4a and b. The pure-bending vibronic spectrum of the $^2E'$ state obtained with inclusion of SO coupling is shown in Fig. 4.4c. The spectrum remains almost unchanged, since the SO coupling is rather weak. The insets in Fig. 4.4 show the first two peaks of the low-resolution spectra on an expanded energy scale. No splitting of the origin line of the high-resolution spectrum due to inclusion of the SO coupling is observed, since the SO splitting is completely quenched by the very strong JT coupling near the origin of the absorption band. The extraction of the SO-coupling constant from the origin region of an experimental high-resolution vibronic spectrum would thus be impossible in this case.

Fig.4.5 shows external vibronic spectra of the $^2E'$ state of TiF_3 obtained with the inclusion of both bending and stretching modes, without (a) and with (b) inclusion of SO coupling. The comparison of Fig. 4.5a with Fig. 4.4b reveals the effect of the JT coupling of the stretching mode. It is seen that only the spectrum arising from the upper surface is moderately affected by the inclusion of stretching mode. The insets show the first two peaks of the low-resolution spectra on an expanded energy scale. Fig. 4.5b represents the final result of our *ab initio* simulation of the external vibronic spectrum of the $^2E'$ state of TiF_3. The overall spectrum is little affected by the inclusion of the rather weak SO coupling.

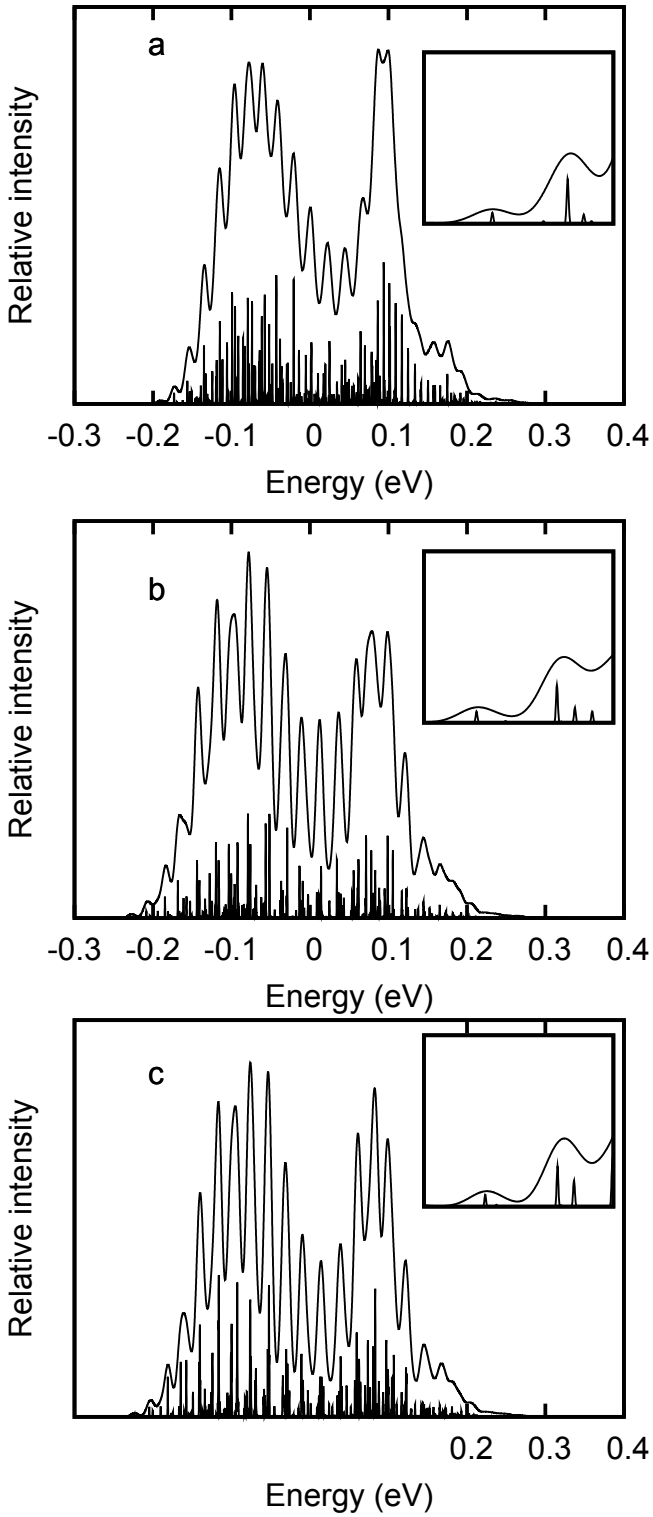

Figure 4.4: External vibronic spectrum of the $^2E'$ excited state of TiF_3 considering only the bending mode and the second-order JT Hamiltonian (a), the sixth-order JT Hamiltonian (b) and the sixth-order JT Hamiltonian with SO coupling (c). The insets show the first two peaks of the low-resolution envelope on an expanded energy scale.

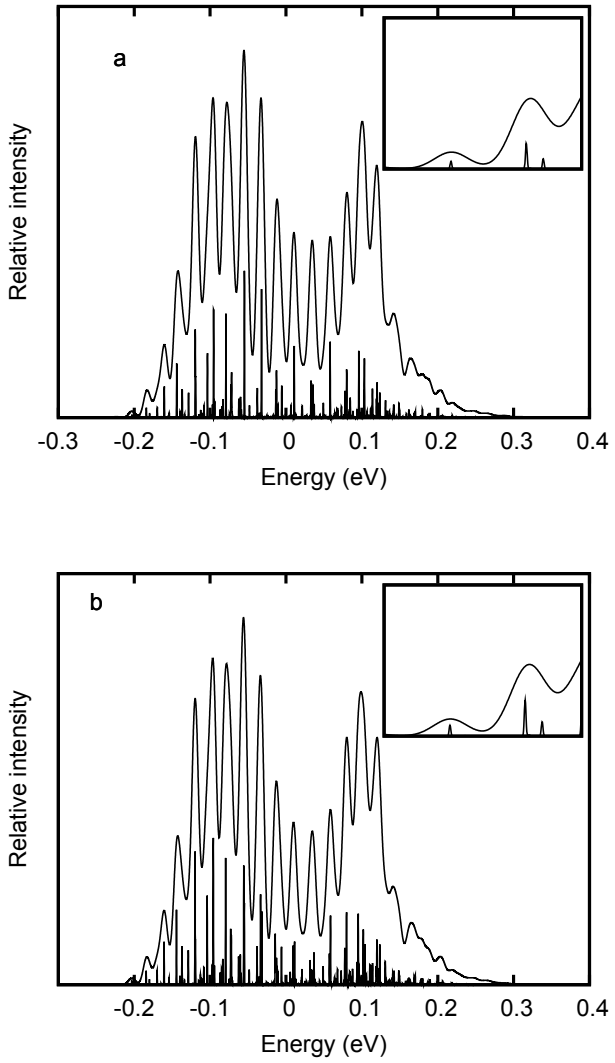

Figure 4.5: External vibronic spectrum of the $^2E'$ excited state of TiF_3, obtained with the two-mode JT Hamiltonian including higher-order JT couplings without SO coupling (a) and with SO coupling (b). The insets show the first two peaks of the low-resolution envelope on an expanded energy scale.

4.2.2 The $^2E''$ state

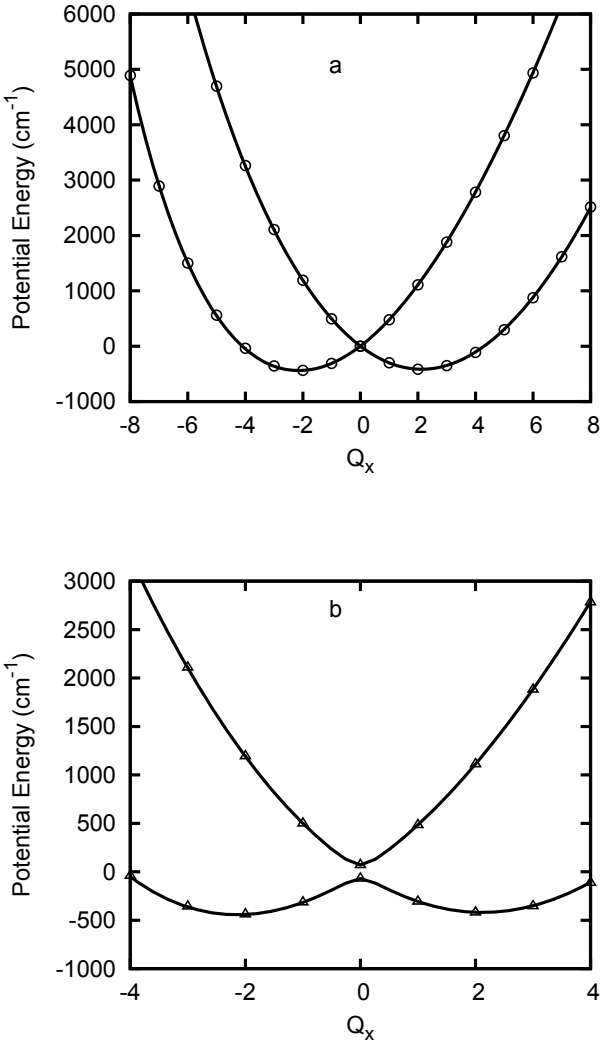

Figure 4.6: PE curves of the $^2E''$ state of TiF_3 along the dimensionless bending normal coordinate Q_x without SO coupling (a) and with SO coupling (b). Symbols correspond to *ab initio* data. The solid lines represent the fitted adiabatic potentials of the sixth-order JT Hamiltonian.

Fig. 4.6 shows the PE curves of the $^2E''$ excited state of TiF_3 as a function of the bending coordinate Q_x, calculated without SO coupling (a) and with SO coupling (b). The symbols correspond to *ab initio* data and the solid lines are the adiabatic potentials of the sixth-order JT Hamiltonian. It is seen that the *ab initio* data are reproduced by the sixth-order JT-SO Hamiltonian with high accuracy. It is also noticed that the JT coupling

in the $^2E''$ excited state is weaker than in the $^2E'$ excited state. The SO coupling in the $^2E''$ state is weaker as well (see Table 4.2).

Fig. 4.7 shows the computed external vibronic spectra of the $^2E''$ excited state of

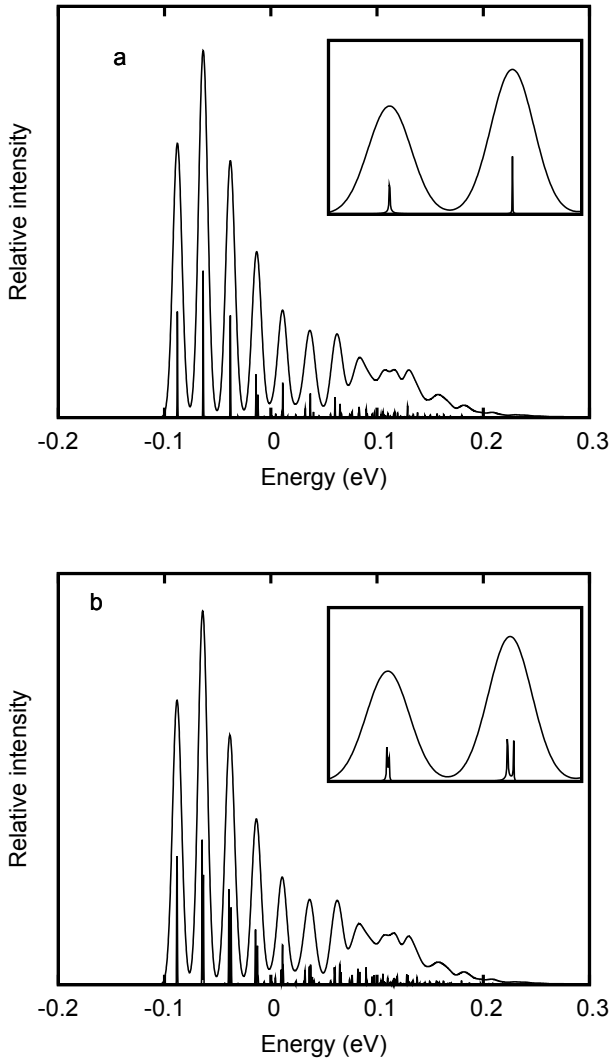

Figure 4.7: External vibronic spectrum of the $^2E''$ excited state of TiF_3, obtained with the two-mode JT model Hamiltonian including higher-order JT couplings without SO coupling (a) and with SO coupling (b).The insets show the first two peaks of the low-resolution envelope on an expanded energy scale.

TiF_3, obtained with the two-mode JT Hamiltonian including higher-order JT couplings without SO coupling (a) and with SO coupling (b). The insets show the first two peaks of the low-resolution spectra on an expanded energy scale. As a consequence of the weaker JT coupling in the $^2E''$ state, the vibrational progression in the spectra is relatively short and there is only a weak indication of a second hump of the envelope. The rather weak SO splitting increases the density of bright vibronic levels, while the effect of SO coupling

molecule	state	Δ (cm^{-1})	mode	ω (cm^{-1})	κ (cm^{-1})	g (cm^{-1})
CrF_3	$^4E'$	76.23	bending	189.700	697.453	54.631
			stretching	806.446	198.932	-91.445
NiF_3	$^4E'$	234.21	bending	182.582	573.073	29.091
			stretching	796.708	166.685	-16.953

Table 4.5: SO and JT coupling parameters for the $^4E'$ states of CrF_3 and NiF_3.

on the low-resolution spectrum is minor, see Fig. 4.7b. The absence of line splittings in the three lowest peaks of the spectrum in Fig. 4.7a indicates that the quadratic JT coupling is very weak. The high-resolution spectrum in the inset of Fig. 4.7b reveals the SO splitting of the first two peaks of the JT vibrational progression. These splittings are much smaller than the nominal SO splitting $2\Delta = 140$ cm^{-1}. The SO quenching factor[16] is ≈ 0.03 and 0.07 for the first and the second peaks, respectively. The SO splitting thus is strongly quenched by the moderately strong JT coupling in the $^2E'$ state of TiF_3.

4.3 Chromium trifluoride (CrF_3): The $^4E'$ state

Fig. 4.8 shows the PE curves of the $^4E'$ first excited state of CrF_3 as a function of the bending coordinate Q_x, calculated without SO coupling (a) and with SO coupling (b). The symbols correspond to *ab initio* data and the solid lines are the adiabatic potentials of the sixth-order JT Hamiltonian which have been fitted to the *ab initio* data. The pronounced splitting of the degeneracy of the $^4E'$ state along the bending mode reflects a strong linear JT effect, while the asymmetry of the two minima reflects a significant quadratic JT coupling. The JT PE curves in Fig. 4.8b reveal the SO-induced splitting of the $^4E'$ state into four doubly degenerate potentials, see Eqs. (3.83-3.86).
The vibrational frequencies, the JT coupling parameters (up to second order) and the SO splittings of the $^4E'$ state of CrF_3 are given in Table 4.5. The anharmonicity constants and higher-order JT coupling parameters are given in Tables 4.3 and 4.4, respectively.

Upon closer inspection of Fig. 4.8a, it is seen that the PE function of the sixth-order JT model deviates noticeably from the ab initio data (for $6.0 \leq Q_x \leq 9.0$). The origin of this anomaly is the PJT coupling of the $^4E'$ excited state with the $^4{A_1}'$ ground state of CrF_3. This phenomenon is discussed in more detail in Appendix G.

Fig. 4.9 shows the external vibronic spectra of the $^4E'$ state of CrF_3 computed with the two-mode JT Hamiltonian including higher-order JT couplings without SO coupling (a) and with SO coupling (b). The double-hump shape of the overall spectral envelope in Fig. 4.9a is the signature of a strong linear JT effect in the bending mode. Quadratic JT coupling and the stretch-bend nonseparability make the high-resolution spectrum rather complex. Inclusion of the SO coupling ($\Delta = 76$ cm^{-1}) increases the density of vibronic levels, but the effect on the low-resolution spectra is limited to the upper hump, see Fig. 4.9b. The high resolution spectra are shown in color (red and blue) in Fig. 4.9b to aid the interpretation. The red spectrum corresponds to the SO splitting 2Δ, while the blue

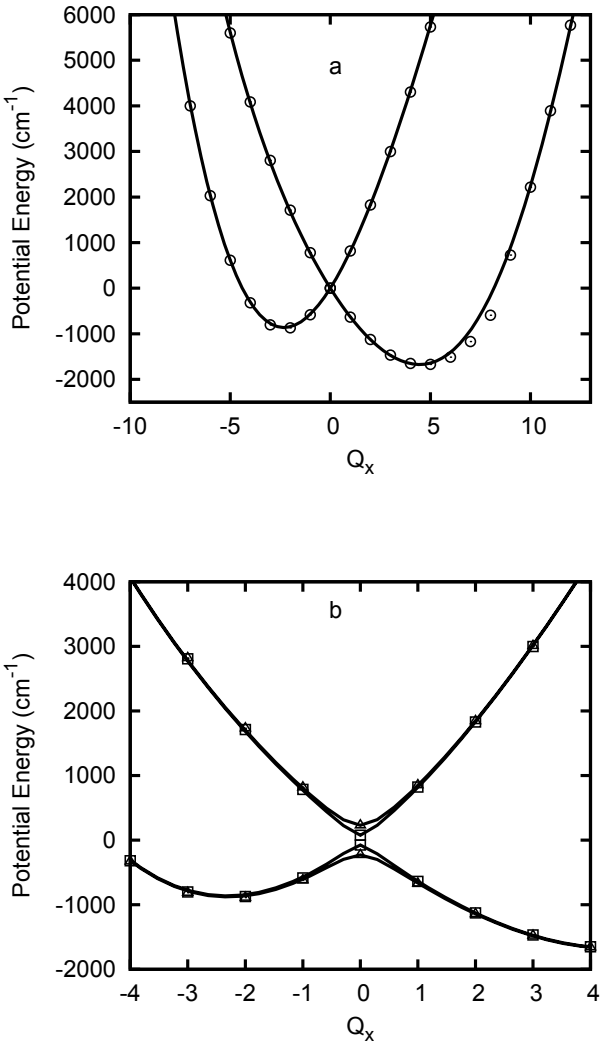

Figure 4.8: PE curves of the $^4E'$ state of CrF_3 along the dimensionless bending normal coordinate Q_x without SO coupling (a) and with SO coupling (b). Symbols correspond to *ab initio* data. The solid lines represent the fitted adiabatic potentials of the sixth-order JT model Hamiltonian.

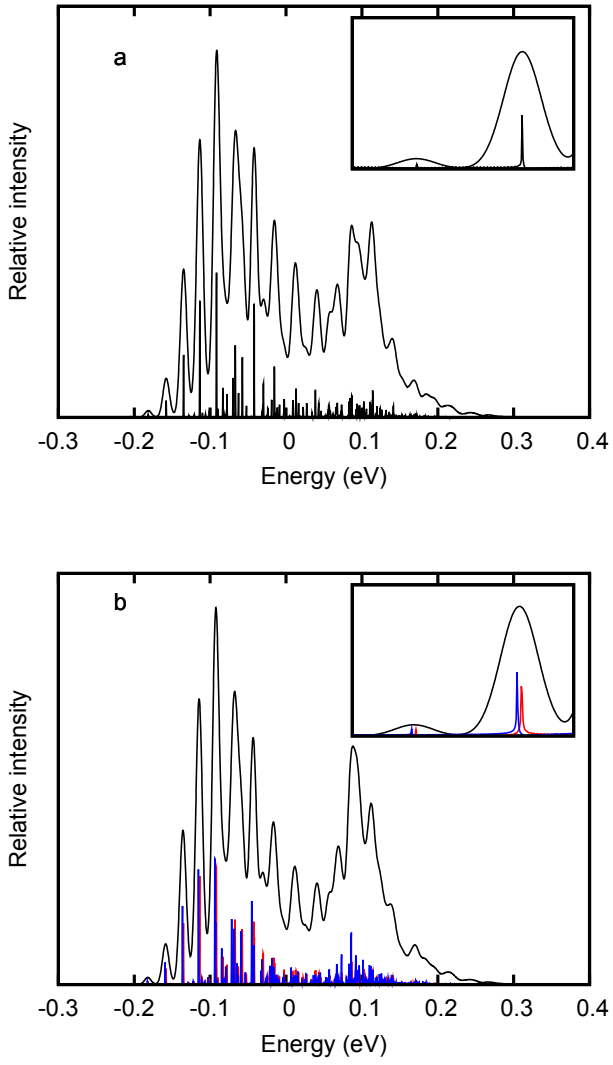

Figure 4.9: External vibronic spectrum of the $^4E'$ state of CrF_3, obtained with the two-mode JT model Hamiltonian including higher-order JT couplings without SO coupling (a) and with SO coupling (b). The insets show the first two peaks of the low-resolution envelope on an expanded energy scale. To aid the assignment, the sub-spectra corresponding to a SO splitting 2Δ and 6Δ are shown in red and blue, respectively, in (b).

spectrum corresponds to the SO splitting 6Δ (see Eqs. (3.83- 3.86) and Fig. 4.8b). The insets show the first two peaks of the low-resolution spectra on an expanded energy scale. It is seen that each line under the low-resolution peak split into two lines upon inclusion of SO coupling. The two lowest lines (blue and red) result from the transition to the lowest level of the two lowest PE surfaces associated with the SO splittings 6Δ and 2Δ, respectively, see Eqs. (3.83-3.86).

4.4 Nickel trifluoride (NiF_3): The $^4E'$ state

The $^4E'$ state of NiF_3 is interesting as it exhibits strong JT coupling as well as strong SO coupling. Since the interpretation of its vibronic spectrum turns out to be quite difficult, we discuss the PE functions and the external vibronic spectra in more detail.

Fig. 4.10 shows the PE curves of the $^4E'$ state of NiF_3 as a function of the bending coordinates Q_x (a) and Q_y (b). It is seen that the sixth-order JT model reproduces the *ab initio* data with high accuracy.

Fig. 4.11 shows the PE curves as a function of the bending coordinate Q_x calculated with inclusion of SO coupling. The symbols correspond to *ab initio* data and the solid lines are the adiabatic potentials of the sixth-order JT Hamiltonian with SO coupling. The electrostatic JT PE curves split into four doubly degenerate curves (see Eqs. (3.83-3.86)) upon inclusion of SO coupling.

The vibrational frequencies, the JT coupling parameters (up to second order) and the SO splittings are given in Table 4.5 for the bending and stretching modes. Both the linear and the quadratic JT coupling constants in the $^4E'$ excited state of NiF_3 are large for the bending mode. The SO coupling is strong as well ($\Delta = 234$ cm^{-1}). As found for the other transition-metal trifluorides, the dimensionless JT coupling parameters κ/ω and g/ω are much larger for the degenerate bending mode than for the degenerate stretching mode (see Table 4.5).

Fig. 4.12 shows computed external vibronic spectra of the $^4E'$ state of NiF_3. The spectrum in Fig. 4.12a has been obtained with the electrostatic second-order JT Hamiltonian, including only the bending mode. It exhibits the characteristic double-hump shape which is the hallmark of a strong linear JT effect. The rather complicated fine structure reflects the strong quadratic JT coupling. The spectrum in Fig. 4.12b has been obtained with the electrostatic sixth-order JT Hamiltonian, including only the bending mode. It is seen that the higher-order JT couplings have a significant effect both on the spectral envelope as well as on the vibronic fine structure. The spectrum in Fig. 4.12c has been obtained with inclusion of the SO coupling. The red and blue high-resolution spectra correspond to the SO splittings 2Δ and 6Δ, respectively. The detailed interpretation of the red and blue spectra is given in the discussion of the final spectrum. The strong SO coupling increases the separation of the two humps of the electrostatic JT spectrum. They qualitatively correspond to the lower and upper pairs adiabatic PE surfaces in Fig. 4.11.

The external vibronic spectrum of the $^4E'$ state of NiF_3 obtained with the two-mode electrostatic JT Hamiltonian including higher-order JT couplings is shown in Fig.

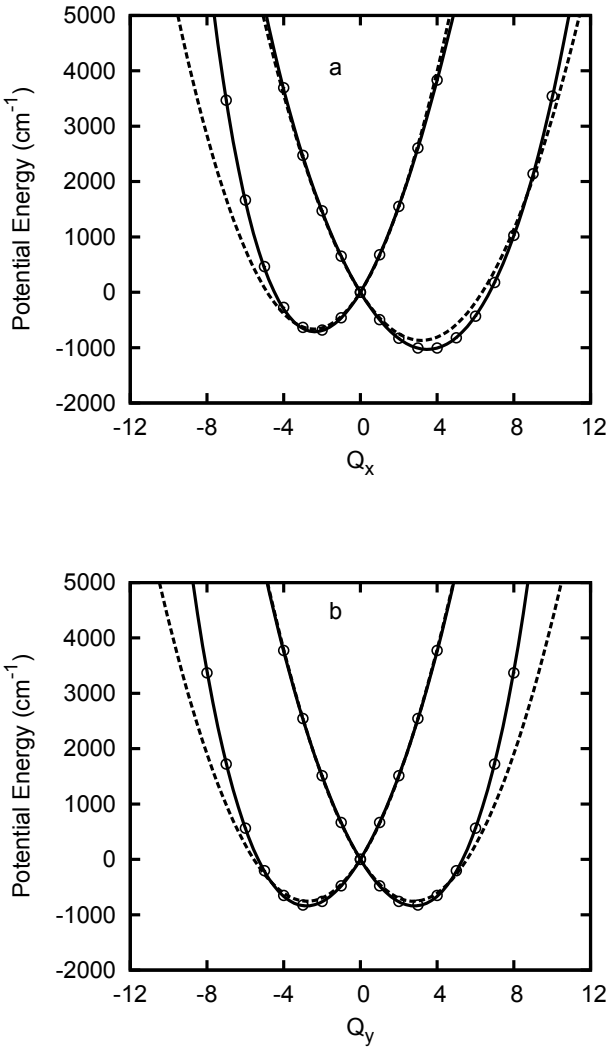

Figure 4.10: PE curves of the ${}^4E''$ state of NiF_3 along the dimensionless bending normal coordinates Q_x (a) and Q_y (b). Circles correspond to *ab initio* data. The solid and dashed lines represent the fitted adiabatic potentials of the sixth-order and second-order JT model Hamiltonians, respectively.

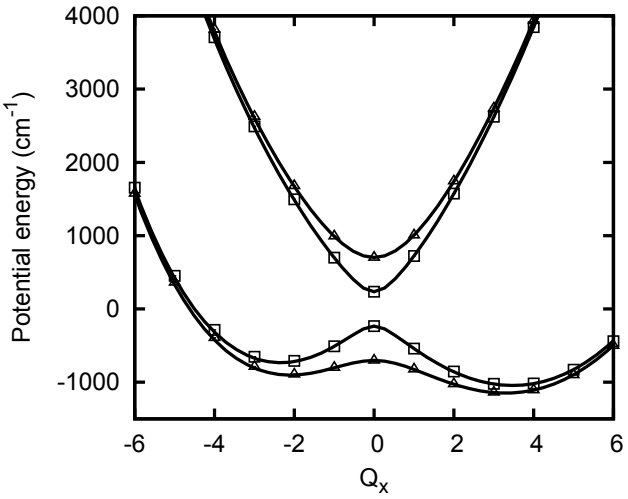

Figure 4.11: PE curves of the $^4E''$ state of NiF_3 along the dimensionless bending normal coordinate Q_x with inclusion of SO coupling . Symbols correspond to *ab initio* data. The solid lines represent the fitted adiabatic potentials of the sixth-order JT model Hamiltonian including SO coupling.

4.13a. The corresponding spectrum obtained with inclusion of SO coupling is shown in Fig. 4.13b, which is the final result of our calculations. To aid the interpretation, the two components of the high-resolution spectrum are shown in color (red and blue) in Fig. 4.13b.

The comparison of Fig. 4.13a with Fig. 4.12b reveals that the inclusion of the degenerate stretching mode has a minor effect on the spectra. The colored spectra in Fig. 4.13b reveal the impact of SO coupling. The red spectrum corresponds to the SO splitting 2Δ, while the blue spectrum corresponds to the SO splitting 6Δ (see Eqs. (3.83 - 3.86) and Fig. 4.11). The JT effect is moderately quenched by SO coupling in the red spectrum, but is strongly quenched in the blue spectrum, especially in the upper adiabatic electronic state.

The insets in Fig. 4.13 show the first two peaks of the low-resolution spectra on an expanded energy scale. The splitting of the second peak in Fig. 4.13a (and Fig. 4.12b) is the result of quadratic JT coupling. The splitting of the second peak in Fig. 4.13b results from both quadratic JT coupling and SO coupling. The difference between the lowest blue peak and the lowest red peak of high-resolution spectra in Fig. 4.13b is an approximate measure of the difference between the two lowest potential-energy curves at their minima (see Fig. 4.11).

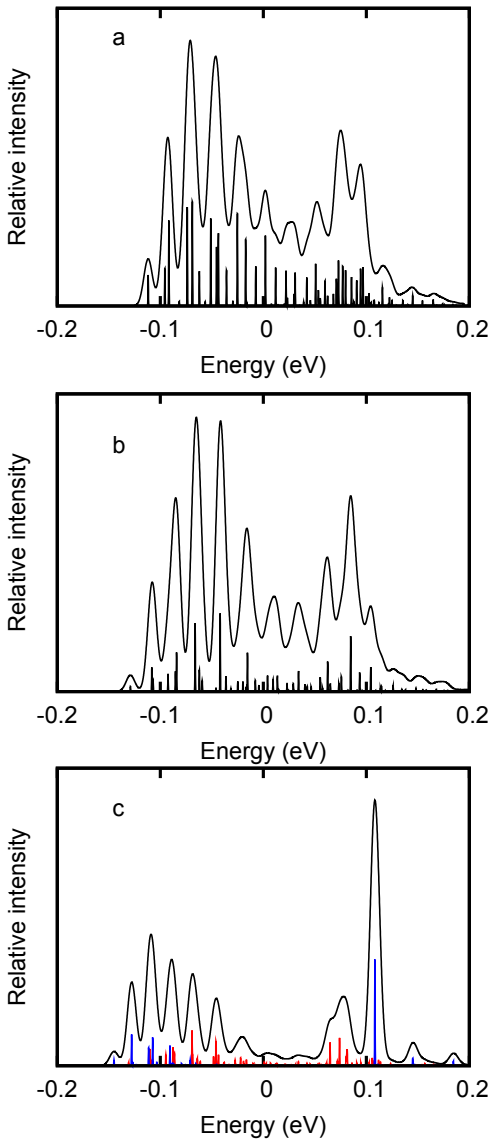

Figure 4.12: External vibronic spectrum of the $^4E'$ state of NiF_3 considering only the bending mode and the second-order JT Hamiltonian (a), the sixth-order JT Hamiltonian (b) and the sixth-order JT Hamiltonian with SO coupling (c). To aid the assignment, the sub-spectra corresponding to a SO splitting 2Δ and 6Δ are shown in red and blue, respectively, in (c).

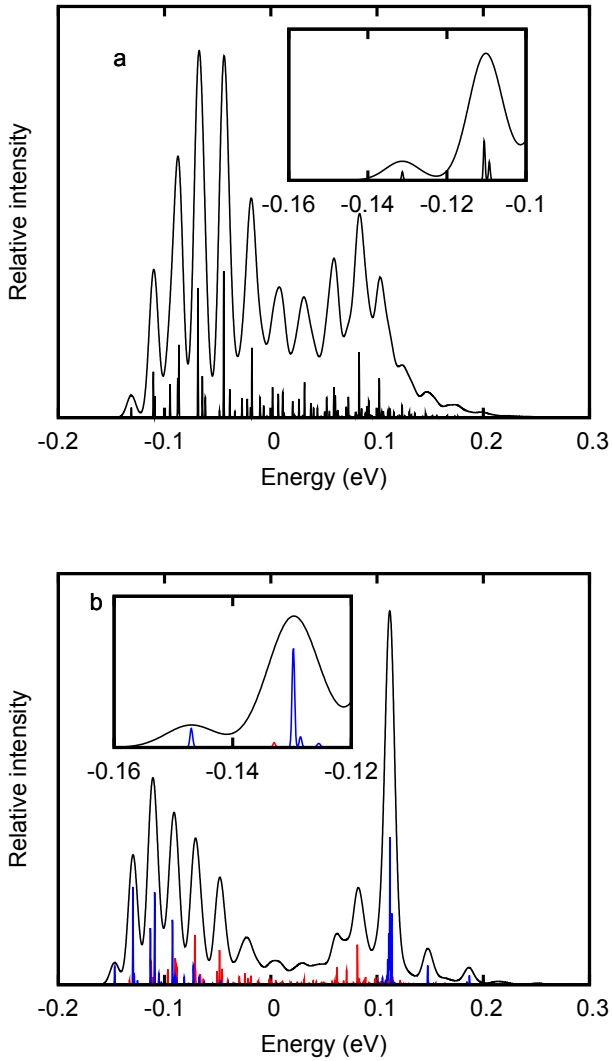

Figure 4.13: External vibronic spectrum of the $^4E'$ state of NiF_3, obtained with the two-mode JT model Hamiltonian including higher-order JT couplings without SO coupling (a) and with SO coupling (b). The insets show the first two peaks of the low-resolution envelope on an expanded energy scale.

Chapter 5

Application to transition-metal trifluorides with odd spin multiplicities

In this chapter, the details of the *ab initio* calculations, the PE surfaces, JT and SO coupling parameters and the external vibronic spectra are discussed for the ${}^5E'$ and ${}^5E''$ states of MnF_3 and CoF_3. For the first example (the ${}^5E'$ state of MnF_3), the individual JT effects, the relevance of higher-order JT coupling parameters, and the two-mode JT effect are discussed in detail, in order to explain the mechanisms giving rise to the rather complex vibronic spectra. For the remaining cases, the final electrostatic (spin-free) JT spectra are compared with the JT spectra including SO coupling effects. The two non-JT-active modes (the totally symmetric stretching mode and the umbrella mode) as well as any possible PJT couplings of the ${}^5E$ states of interest with other electronic states are ignored in this calculation.

5.1 Details of the *ab initio* electronic structure calculations

The PE surfaces of the ground state and low-lying excited states of MnF_3 and CoF_3 have been determined with the all-electron full-valence state-averaged CASSCF method. The all-electron ANO basis set of Bauschlicher[84] was chosen for the Mn and Co atoms, while Dunning's cc-pVQZ basis set[85] was used for F.
The electronic configurations of the ground states of Mn^{3+} and Co^{3+} are $[Ar]3d^4 4s^0$ (${}^5D$) and $[Ar]3d^6 4s^0$ (${}^5D$), respectively, and the electronic configuration of F^- is $[He]2s^2 2p^6$ (${}^1S$). The active space includes 17 valence orbitals with 28 electrons for MnF_3, and 17 valence orbitals with 30 electrons for CoF_3. The remaining 12 orbitals with 24 electrons were considered to be doubly occupied core orbitals.

All *ab initio* calculations have been performed in C_s symmetry. The matrix elements of the SO operator have been computed at the CASSCF level using the full two-electron BP operator. All electronic-structure calculations have been performed with the MOLPRO program package.[86]

Dynamical electron-correlation effects are not included in the present work. This could be a topic of further studies, using the MRCI or CASPT2 methods. However, from *ab initio* calculations of vibrational or vibronic coupling constants for numerous systems, it is known that the energy gradients are less sensitive to dynamical electron-correlation effects than the VEE. For SO splittings, it is well known that they are little affected by dynamical electron-correlation effects, since SO coupling is primarily a one-electron operator.

5.2 Manganese trifluoride (MnF_3)

5.2.1 The $^5E'$ state

Fig. 5.1 shows the PE curves of the $^5E'$ electronic ground state of MnF_3 along the dimensionless bending normal coordinates Q_x (a) and Q_y (b). The circles correspond to *ab initio* data, while the dashed and solid lines are the PE functions of the second-order and sixth-order JT Hamiltonians, respectively, which have been fitted to the *ab initio* data. Figs. 5.1a, b clearly reveal that a JT expansion up to second order is not sufficient to describe the JT PE functions of the $^5E'$ state of MnF_3, whereas the expansion up to sixth order results in an excellent fit to the *ab initio* data. The pronounced splitting of the degeneracy of the $^5E'$ state along the bending mode reveals a very strong linear JT effect, whereas the asymmetry of the two minima in Fig. 5.1a is a measure of the quadratic JT coupling.

Fig. 5.2 shows the corresponding PE curves of the $^5E'$ state of MnF_3 along the dimensionless stretching normal coordinate Q_x (a) and Q_y (b). The circles correspond to *ab initio* data, while the dashed and solid lines are the PE functions of the second-order and fourth-order JT Hamiltonians, respectively, which have been fitted to the *ab initio* data. It is seen that the JT coupling of the stretching mode is much weaker than the JT coupling of the bending mode. Nevertheless, the quadratic expansion of the JT surfaces is not sufficient for an accurate fitting of the *ab initio* data, see Fig. 5.2a.

Fig. 5.3 shows the PE curves of the $^5E'$ state of MnF_3 along the dimensionless bending normal coordinate Q_x with inclusion of SO coupling. The symbols correspond to *ab initio* data and the solid lines are the PE functions of the sixth-order JT Hamiltonian including SO coupling. In the model Hamiltonian, the SO splitting is included in zeroth order of the normal-mode expansion (first-order terms vanish by symmetry and the second-order or higher-order terms are neglected). It is seen that the adiabatic PE functions of the model nevertheless provide an excellent fit of the *ab initio* data over a large range of the bending normal mode. Fig. 5.3 shows the splitting of the PE curves near the reference geometry into six curves upon inclusion of SO coupling. Two of these curves are unaffected by the SO coupling ($\Delta = 0$, see Eqs. (3.89, 3.90)). The remaining four potentials, exhibiting splittings of Δ and 2Δ, are two-fold degenerate (see Eqs. (3.87, 3.88, 3.91, 3.92)).

The vibrational frequencies, linear and quadratic JT coupling parameters of the bending and stretching modes as well as the SO splittings are given in Table 5.1 for the $^5E'$ and $^5E''$ states of MnF_3. Details of the extraction of JT and SO coupling parameters using a least-squares fitting procedure are discussed in Appendix C. Higher-order fitting procedure is also described there. The anharmonicity constants and the higher-order JT

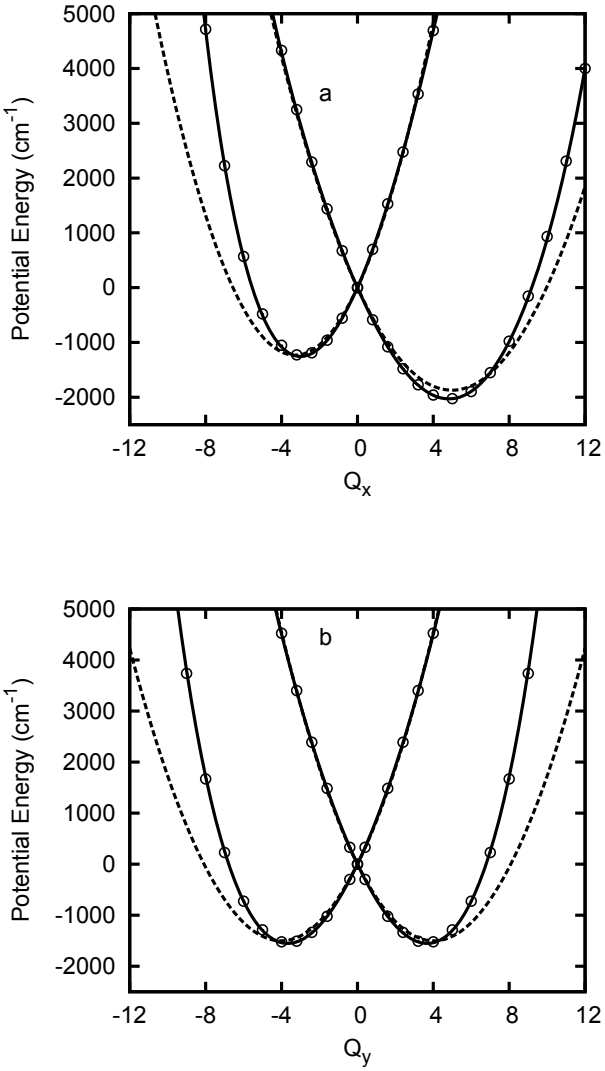

Figure 5.1: PE curves of the ${}^5E'$ state of MnF_3 along the dimensionless bending normal coordinates Q_x (a) and Q_y (b). Circles correspond to *ab initio* data. The solid and dashed lines represent the fitted adiabatic potentials of the sixth-order and second-order JT model Hamiltonians, respectively.

state	Δ (cm^{-1})	mode	ω (cm^{-1})	κ (cm^{-1})	g (cm^{-1})
${}^5E'$	145.45	bending	175.85	788.20	42.20
		stretching	768.88	231.63	-57.75
${}^5E''$	82.47	bending	175.90	311.01	-17.35
		stretching	824.27	525.01	-25.73

Table 5.1: SO and JT coupling parameters for the ${}^5E'$ and ${}^5E''$ states of MnF_3.

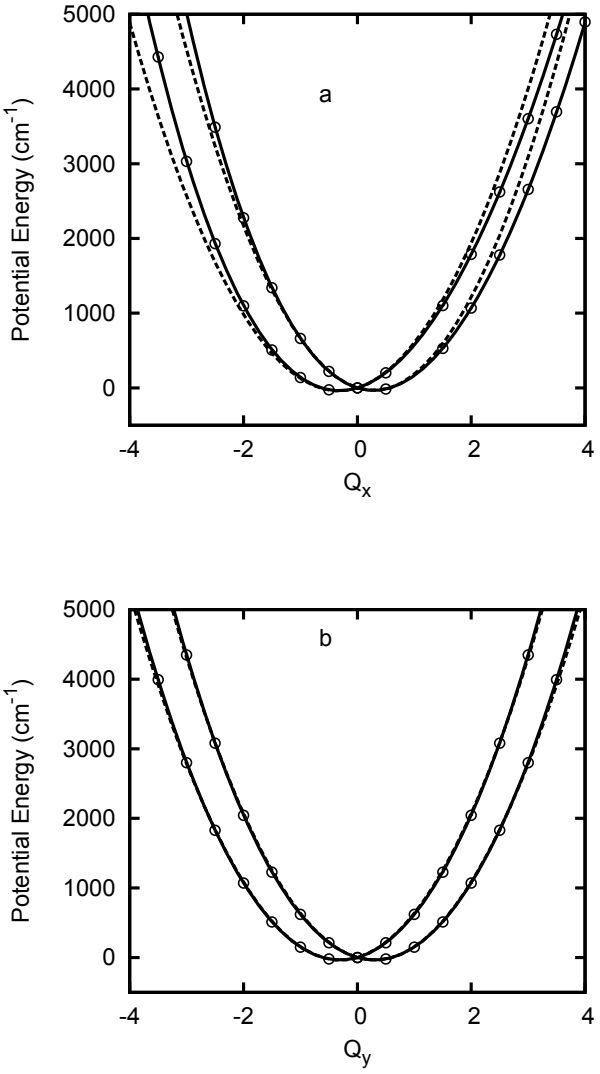

Figure 5.2: PE curves of the ${}^5E'$ state of MnF_3 along the dimensionless stretching normal coordinates Q_x (a) and Q_y (b). Circles correspond to *ab initio* data. The solid and dashed lines represent the fitted adiabatic potentials of the fourth-order and second-order JT model Hamiltonians, respectively.

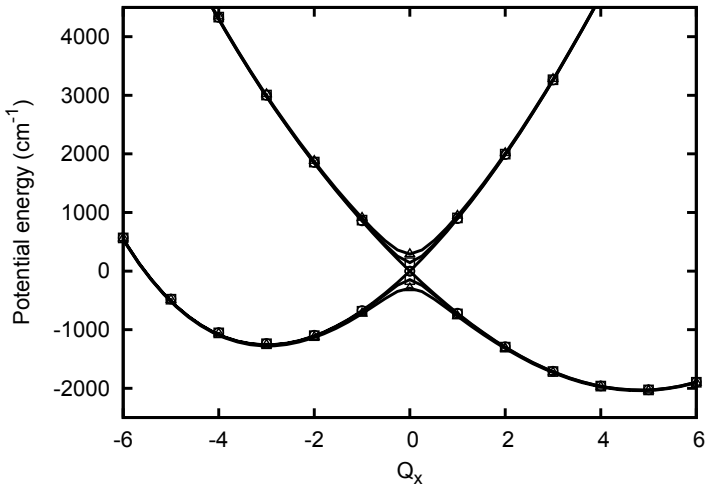

Figure 5.3: PE curves of the $^5E'$ state of MnF_3 along the dimensionless bending normal coordinate Q_x with inclusion of SO coupling. Symbols correspond to *ab initio* data. The solid lines represent the fitted adiabatic potentials of the sixth-order JT model Hamiltonian including SO coupling.

coupling parameters are given in Tables 5.2 and 5.3, respectively.

It is seen that the SO splitting Δ is approximately equal to the bending vibrational frequency. The dimensionless JT parameters κ/ω and g/ω are much larger for the bending mode than for the stretching mode. The JT stabilization energy (E_{JT}) of the $^5E'$ state in the quadratic approximation is 2250 cm^{-1}, which is in qualitative agreement with previous results.[34,87]

For MnF_3, we consider the fluorescence emission spectrum from a nondegenerate excited electronic state to the $^5E'$ electronic ground state. For clarity, the external vibronic spectra of the primarily JT-active bending mode are considered first. Figs. 5.4a and b show the external vibronic spectra obtained with the second-order and sixth-order JT

Molecule	state	mode	$a_1^{(3)}$	$a_1^{(4)}$	$a_1^{(5)}$	$a_1^{(6)}$	$a_2^{(6)}$
MnF_3	$^5E'$	bending	-4.069	6.729	-2.055	0.051	1.066
		stretching	-49.984	34.208	-	-	-
	$^5E''$	bending	-5.645	4.694	-2.061	0.102	2.006
		stretching	-52.038	33.044	-	-	-
CoF_3	$^5E'$	bending	-6.108	5.893	-1.569	0.055	0.991
		stretching	-52.216	32.124	-	-	-
	$^5E''$	bending	-6.259	5.089	-1.636	0.065	1.384
		stretching	-53.822	35.926	-	-	-

Table 5.2: Anharmonicity constants $a_1^{(n)}$, $a_2^{(n)}$ (in cm^{-1}) for the $^5E'$ and $^5E''$ states of MnF_3 and CoF_3.

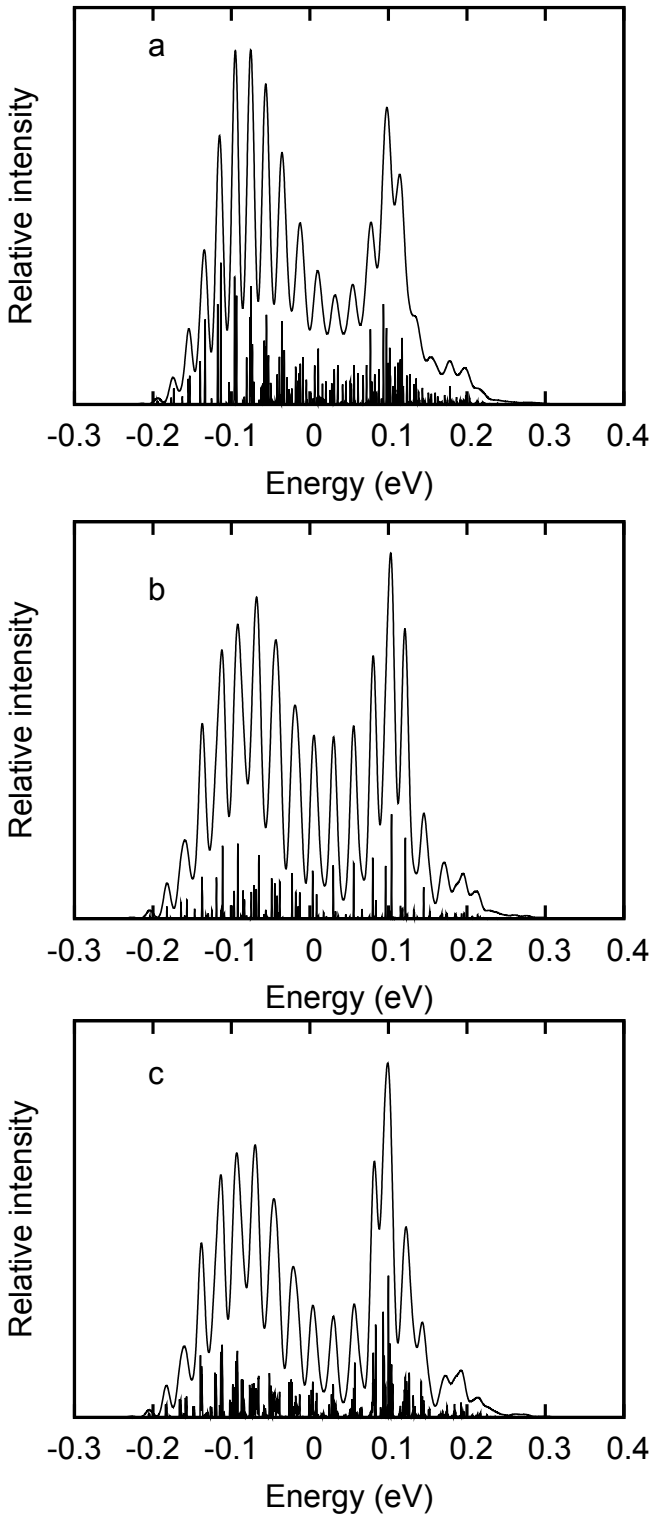

Figure 5.4: External vibronic spectrum of the ${}^5E'$ ground state of MnF_3 considering the bending mode and the second-order JT Hamiltonian (a) the sixth-order JT Hamiltonian (b) and the sixth-order JT Hamiltonian with SO coupling (c).

Molecule	state	mode	$\lambda_1^{(3)}$	$\lambda_1^{(4)}$	$\lambda_2^{(4)}$	$\lambda_1^{(5)}$	$\lambda_2^{(5)}$	$\lambda_1^{(6)}$	$\lambda_2^{(6)}$
MnF_3	$^5E'$	bending	-14.315	0.370	-2.034	0.032	0.931	-0.086	-0.034
		stretching	7.948	-0.422	1.376	-	-	-	-
	$^5E''$	bending	-3.407	-0.538	0.795	-0.022	-0.083	0.200	-0.173
		stretching	7.150	-2.832	2.313	-	-	-	-
CoF_3	$^5E'$	bending	-10.090	0.166	-1.020	0.014	0.469	-0.047	-0.004
		stretching	3.903	-0.097	0.452	-	-	-	-
	$^5E''$	bending	-2.396	0.055	0.094	0.005	-0.014	0.00	0.013
		stretching	7.631	0.815	-1.924	-	-	-	-

Table 5.3: Higher-order JT coupling parameters $\lambda_1^{(n)}$, $\lambda_2^{(n)}$ (in cm^{-1}) for the $^5E'$ and $^5E''$ states of MnF_3 and CoF_3.

Hamiltonians, respectively. The characteristic double-hump structure of the overall envelope of the spectrum reflects the existence of a strong first-order JT coupling. The main vibrational progression of the low-resolution spectrum results from the strong linear JT coupling of the bending mode. The line splittings, which are clearly visible in the high-resolution spectrum, are caused by the strong quadratic JT coupling. The comparison of Figs. 5.4a and b shows that higher-order JT couplings have a significant effect both on the vibronic fine structure as well as on the envelope of the external vibronic spectrum. The envelope of the sixth-order spectrum is more structured and the lines of the high-resolution sixth-order spectrum are more clumped than in the second-order spectrum. The reason is the strong positive anharmonicity of the ab initio bending potentials, see Fig. 5.1. The latter arises from the "intramolecular collision" of neighbouring fluorine atoms at large amplitudes of the bending mode.

The pure-bending vibronic spectrum obtained upon inclusion of the SO coupling is shown in Fig. 5.4c. Inclusion of the SO coupling results in a further pronounced increase of the density of vibronic levels, reflected in an apparent broadening of the peaks of the main progression of the low-resolution spectrum. It should be noted that the full JT-SO spectrum (Fig. 5.4c) is a superposition of three JT-SO spectra with SO splittings 0, Δ, 2Δ. The spectrum in Fig. 5.4b is thus contained in Fig. 5.4c.

Fig. 5.5 shows external vibronic spectra of the $^5E'$ ground state of MnF_3 obtained with the inclusion of both bending and stretching modes, without (a) and with (b) inclusion of SO coupling. The comparison of Fig. 5.5a with Fig. 5.4b reveals the effect of the JT coupling of the stretching mode. While the vibronic line density increases due to the nonseparability of bending and stretching modes in the JT Hamiltonian, the envelope of the low-resolution spectrum is little affected by the comparatively weak JT coupling of the stretching mode.

Fig. 5.5b represents the final result of our *ab initio* simulation of the external vibronic spectrum of the $^5E'$ state of MnF_3. The inclusion of the relatively weak SO splitting leads to a slight increase of the line density and a more pronounced double-hump shape of the overall spectrum. Since the SO splitting is completely quenched by the strong JT coupling near the origin of the absorption/emission band, the extraction of the SO coupling constant from an experimental high-resolution vibronic spectrum would be impossible.

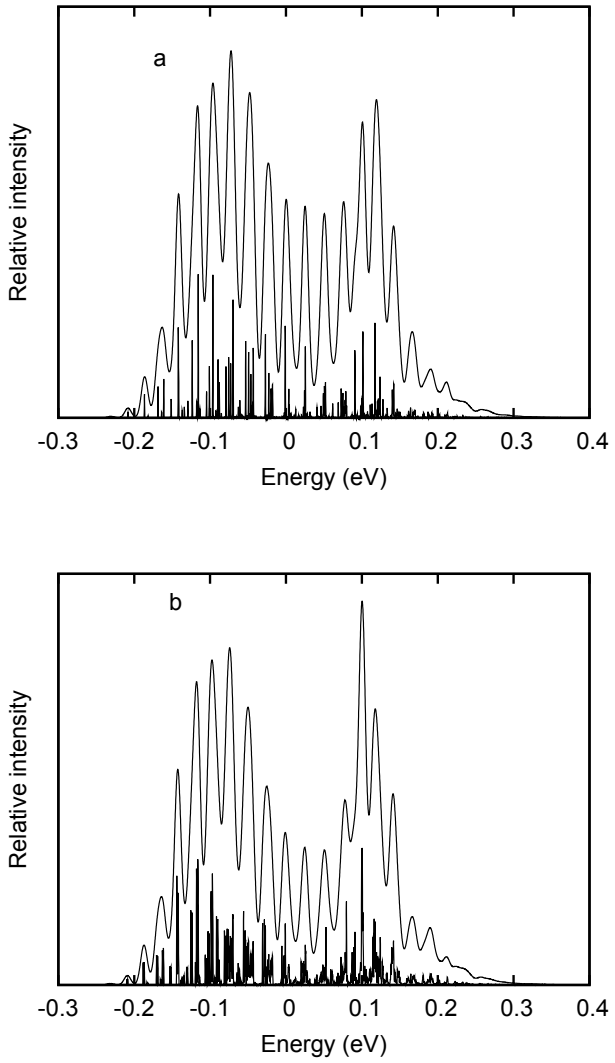

Figure 5.5: External vibronic spectrum of the ${}^5E'$ ground state of MnF_3, obtained with the two-mode JT Hamiltonian including higher-order JT couplings without SO coupling (a) and with SO coupling (b).

5.2.2 The $^5E''$ state

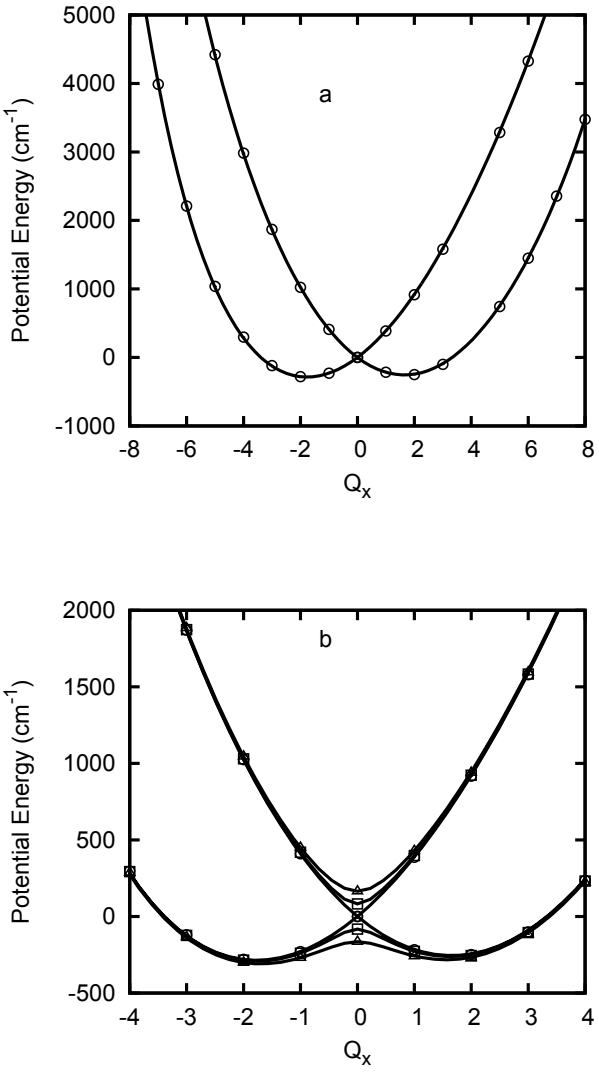

Figure 5.6: PE curves of the $^5E''$ state of MnF_3 along the dimensionless bending normal coordinate Q_x without SO coupling (a) and with SO coupling (b). Symbols correspond to *ab initio* data. The solid lines represent the fitted adiabatic potentials of the sixth-order JT Hamiltonian.

Fig. 5.6 shows the PE curves of the $^5E''$ excited state of MnF_3 as a function of the bending coordinate Q_x, calculated without SO coupling (a) and with SO coupling (b). The symbols correspond to *ab initio* data and the solid lines are the adiabatic potentials of the sixth-order JT Hamiltonian. It is seen that the *ab initio* data are reproduced by the sixth-order JT-SO Hamiltonian with high accuracy. It is also noticed that the JT coupling in the $^5E''$ excited state is weaker than in the $^5E'$ ground state. The JT stabilization energy of the $^5E''$ state is 250 cm^{-1}. The SO coupling in the $^5E''$ state is also weaker than in

the ground state. The vibrational frequencies, the JT coupling parameters (up to second order) and the SO splittings for the ${}^5E''$ state are given in Table 5.1.

Fig. 5.7 shows the computed external vibronic spectra of the ${}^5E''$ excited state of

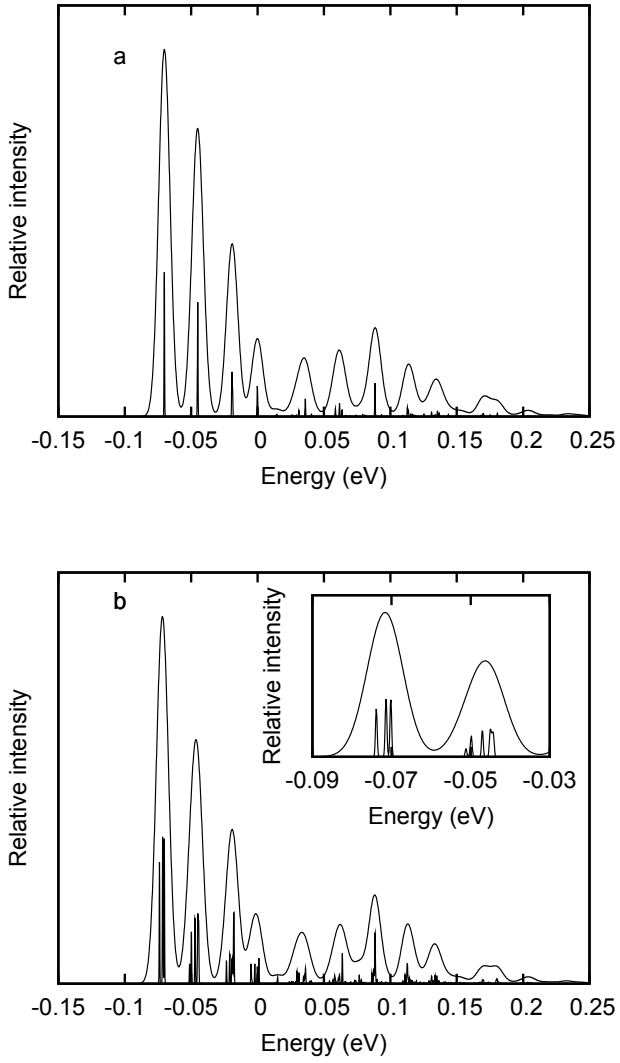

Figure 5.7: External vibronic spectrum of the ${}^5E''$ ground state of MnF_3, obtained with the two-mode JT model Hamiltonian including higher-order JT couplings without SO coupling (a) and with SO coupling (b). The inset in (b) shows the first two peaks of the low-resolution envelope on an expanded energy scale.

MnF_3, obtained with the JT Hamiltonian including higher-order JT couplings without SO coupling (a) and with SO coupling (b). As a consequence of the weaker JT coupling in the ${}^5E''$ state, the progression in the spectra is relatively short and there is only a weak indication of a second hump of the envelope. The rather weak SO splitting increases the density of bright vibronic levels, while the effect of SO coupling on the low-resolution spectrum is minor, see Fig. 5.7b. The absence of line splittings in the lower peaks of the

state	Δ (cm^{-1})	mode	ω (cm^{-1})	κ (cm^{-1})	g (cm^{-1})
$^5E'$	292.93	bending	183.70	548.40	28.42
		stretching	779.55	164.40	-32.52
$^5E''$	154.79	bending	192.92	264.44	-12.46
		stretching	798.68	415.95	-21.11

Table 5.4: SO and JT coupling parameters for the $^5E'$ and $^5E''$ states of CoF_3.

spectrum in Fig. 5.7a indicates that the quadratic JT coupling is very weak. The inset in Fig. 5.7b shows the first two peaks of the low-resolution spectrum on an expanded energy scale. The three-fold splitting of the lowest band reflects the quasi-degeneracy of the three lowest PE curves near their minima, see Fig. 5.7b. In this case, it would be possible to extract the SO coupling constant from an experimental high-resolution spectrum, provided the quenching of the SO splitting by the two-mode JT effect is taken into account.

5.3 Cobalt trifluoride (CoF_3)

5.3.1 The $^5E'$ state

Fig. 5.8 shows the PE curves of the $^5E'$ first excited state of CoF_3 as a function of the bending coordinate Q_x, calculated without SO coupling (a) and with SO coupling (b). The symbols correspond to *ab initio* data and the solid lines are the adiabatic potentials of the sixth-order JT Hamiltonian which have been fitted to the *ab initio* data. The large splitting of the degeneracy of the $^5E'$ state along the bending mode reflects a strong linear JT effect, whereas the asymmetry of the two minima reflects a significant quadratic JT coupling. The JT potential-energy curves in Fig. 5.8b reveal the SO-induced splitting of the $^5E'$ state into six different curves, four of which are doubly degenerate, see Eqs. (3.87-3.92). The size of the SO coupling constant Δ in the $^5E'$ state of CoF_3 is significantly larger than in the $^5E'$ state of MnF_3.
The vibrational frequencies, the JT coupling parameters (up to second order) and the SO splittings of the $^5E'$ state of CoF_3 are given in Table 5.4. The anharmonicity constants and higher-order JT coupling parameters are given in Tables 5.2 and 5.3, respectively. As found for the $^5E'$ state of MnF_3, the dimensionless JT coupling parameters κ/ω and g/ω are much larger for the degenerate bending mode than for the degenerate stretching mode. E_{JT} for the $^5E'$ state is 964 cm^{-1} in the quadratic approximation.

Fig. 5.9 shows the external vibronic spectrum of the $^5E'$ state of CoF_3 computed with the JT Hamiltonian including higher-order JT couplings without SO coupling (a) and with SO coupling (b). The double-hump shape of the overall spectral envelope in Fig. 5.9a is the signature of a strong linear JT effect in the bending mode. Quadratic JT coupling and the stretch-bend nonseparability lead to splittings of the peaks of the main progression. The significant difference in the shape and structure of the spectra in Figs. 5.9a and 5.9b is caused by the strong SO coupling (293 cm^{-1}) in the $^5E'$ state of CoF_3. Again, the SO splitting is completely quenched near the band origin by the strong JT

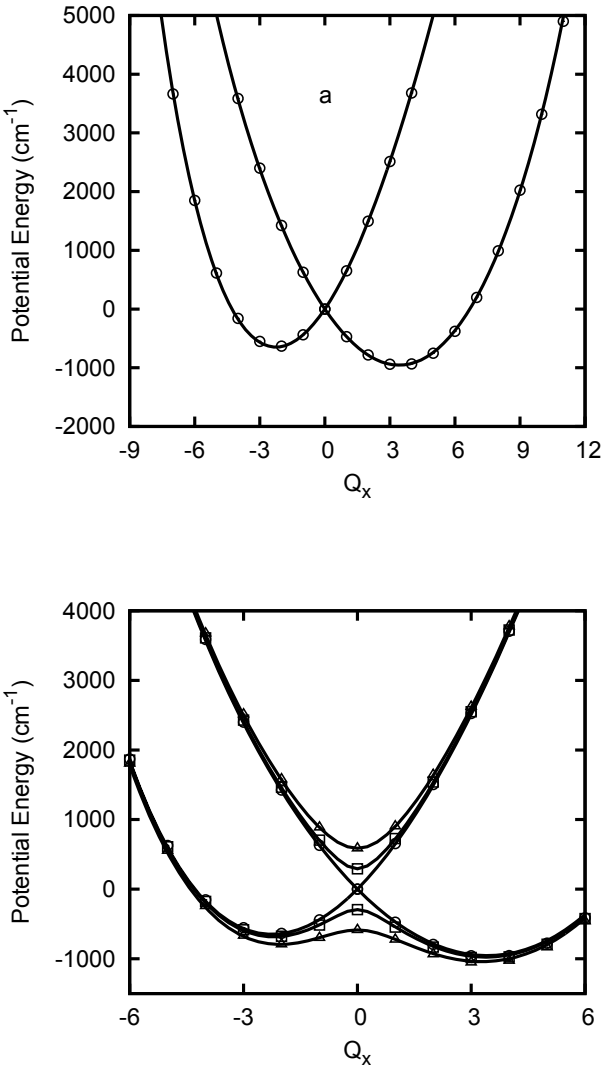

Figure 5.8: PE curves of the ${}^5E'$ state of CoF_3 along the dimensionless bending normal coordinate Q_x without SO coupling (a) and with SO coupling (b). Symbols correspond to *ab initio* data. The solid lines represent the fitted adiabatic potentials of the sixth-order JT model Hamiltonian.

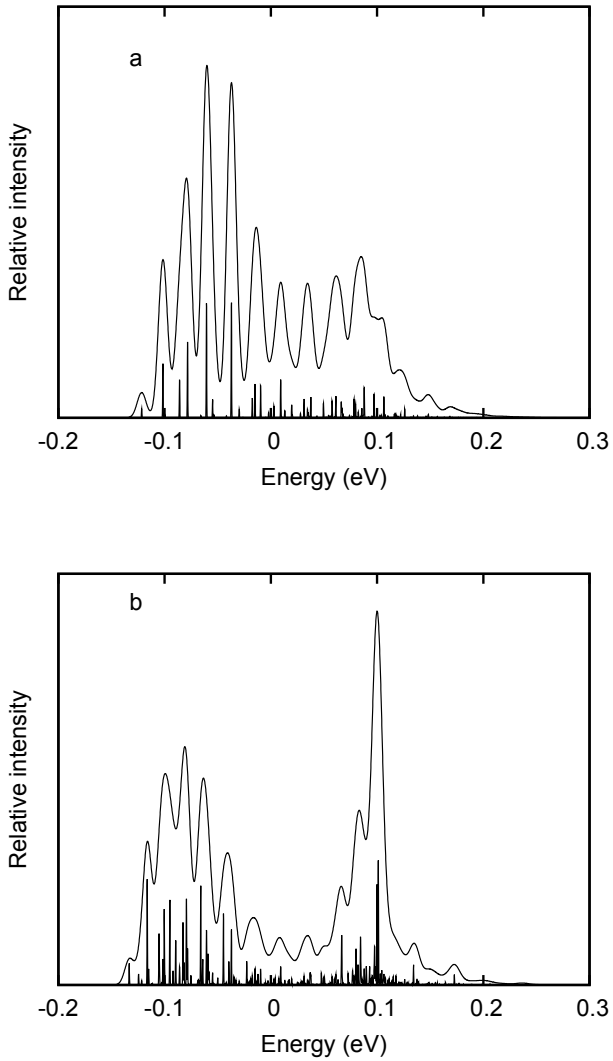

Figure 5.9: External vibronic spectrum of the $^5E'$ state of CoF_3, obtained with the two-mode JT model Hamiltonian including higher-order JT couplings without SO coupling (a) and with SO coupling (b).

coupling of the bending mode.

5.3.2 The $^5E''$ state

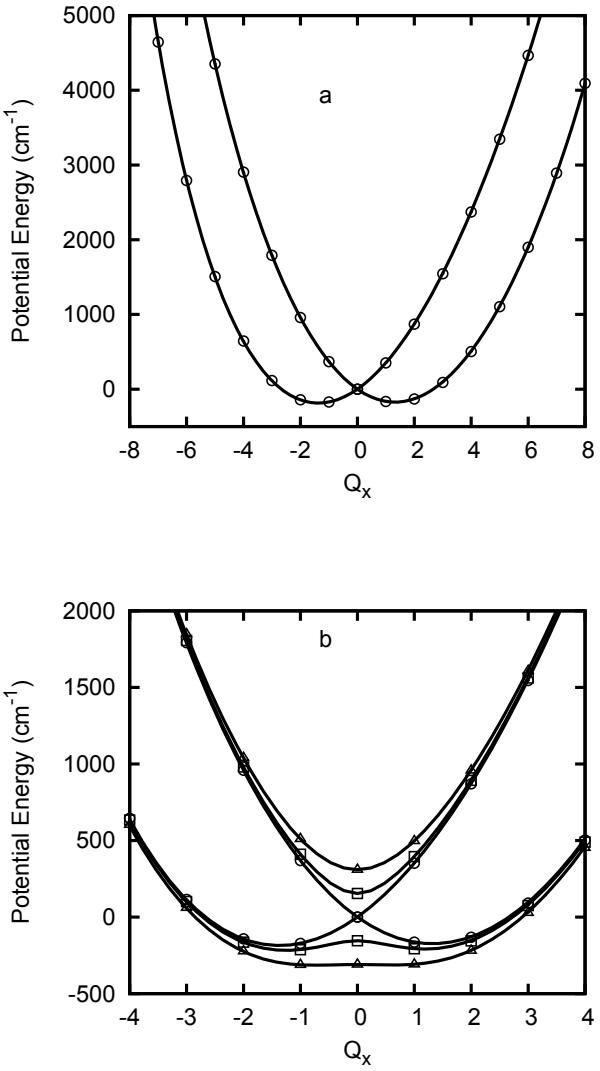

Figure 5.10: PE curves of the $^5E''$ state of CoF_3 along the dimensionless bending normal coordinate Q_x without SO coupling (a) and with SO coupling (b). Symbols correspond to *ab initio* data. The solid lines represent the fitted adiabatic potentials of the sixth-order JT model Hamiltonian.

Fig. 5.10 shows the PE curves of the $^5E''$ state of CoF_3 as a function of the bending coordinate Q_x calculated without SO coupling (a) and with SO coupling (b). The symbols correspond to *ab initio* data and the solid lines are the adiabatic potentials of the sixth-order The vibrational frequencies, the JT coupling parameters (up to second order) and

the SO splittings are given in Table 5.2 for both bending and stretching modes. The linear and quadratic JT couplings in the $^5E''$ excited state of CoF_3 are weaker than the JT couplings in the $^5E'$ state. The SO coupling is weaker as well. The JT stabilization energy in the quadratic approximation is 170 cm^{-1}, in very good agreement with the previous value of 164 cm^{-1} reported by Yates and Pitzer.[33]

Fig. 5.11 shows the external vibronic spectrum of the $^5E''$ state of CoF_3 computed

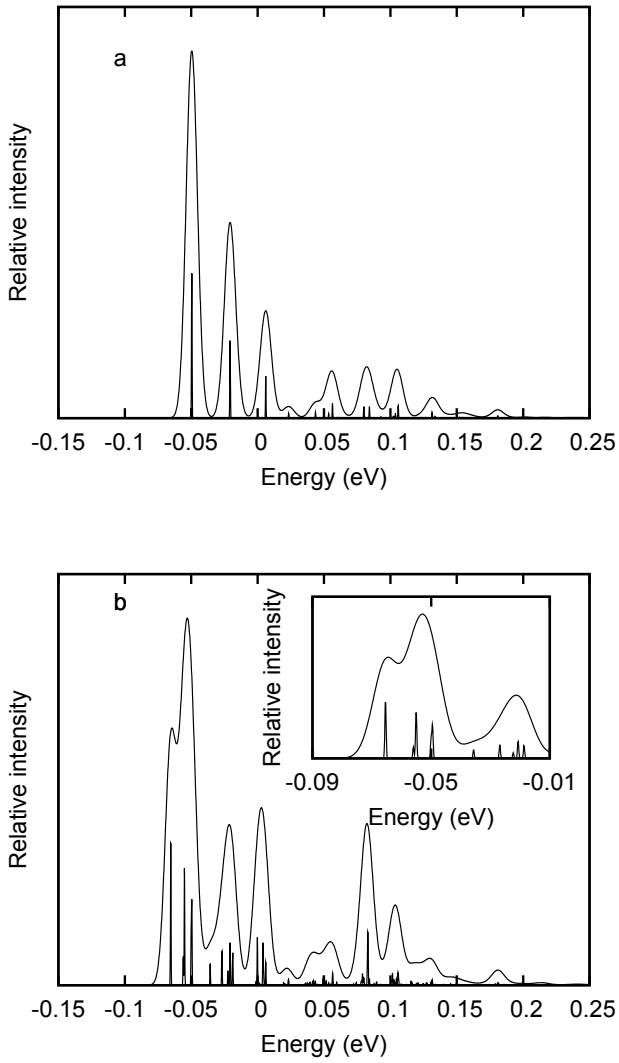

Figure 5.11: External vibronic spectrum of the $^5E''$ state of CoF_3, obtained with the two-mode JT model Hamiltonian including higher-order JT couplings without SO coupling (a) and with SO coupling (b). The inset in (b) shows the first two peaks of the low-resolution envelope on an expanded energy scale.

with the JT Hamiltonian including higher-order JT couplings without (a) and with (b) inclusion of SO coupling. The spectra are characteristic of a moderate JT effect with moderate SO coupling. In this case, the SO splitting is only partially quenched by the

JT coupling near the band origin, see Fig. 5.11b. The inset in Fig. 5.11b shows the first two peaks of the low-resolution spectrum on an expanded energy scale. Like in Fig. 5.7b, the splitting of the lowest band into three lines mirrors the quasi-degeneracy of the three PE functions near their minima, see Fig. 5.10b.

Chapter 6

Vibronic infrared spectra of MnF_3 and NiF_3

In this chapter, internal vibronic spectra for the $^5E''$ state of MnF_3 and the $^4E'$ state of NiF_3 are discussed. Details of the *ab initio* calculation of the DMS are given in Section 6.1. In Section 6.2, the DMS and the internal vibronic spectra of the $^5E''$ state of MnF_3 are discussed. The DMS and internal vibronic spectra for the $^4E'$ state of NiF_3 are discussed in Section 6.3. The effects of temperature as well as SO coupling are also analyzed. For brevity and clarity, only the strongly JT-active bending modes are considered in the following.

6.1 *Ab initio* calculation of dipole moment surfaces

Dipole moments are one-electron operators and expectation values can be obtained directly from *ab initio* electronic structure calculations. The expectation values of dipole moment operator and the transition dipole moments (TDM) were calculated with the CASSCF method using the MOLPRO[86] program package. The dipole moments were calculated as functions of the JT-active degenerate bending vibrational modes Q_x and Q_y. The active spaces and other details of the *ab initio* calculations were discussed in Section 5.1.

6.2 MnF_3 - The $^5E''$ state

6.2.1 Dipole moment and transition dipole moment surfaces

The adiabatic-to-diabatic mixing angle (see Eq. (E.1)) as a function of the vibrational bending coordinates Q_x and Q_y is shown in Fig. 6.1. It reveals the high sensitivity of the wavefunctions to the nuclear conformation in the vicinity of a CI. Along a branch cut, which extends from the CI to either smaller or larger Q_x (the choice of the branch cut is arbitrary), the mixing angle changes sign. The derivatives of the mixing angle give rise to the singular non-adiabatic-coupling matrix elements.

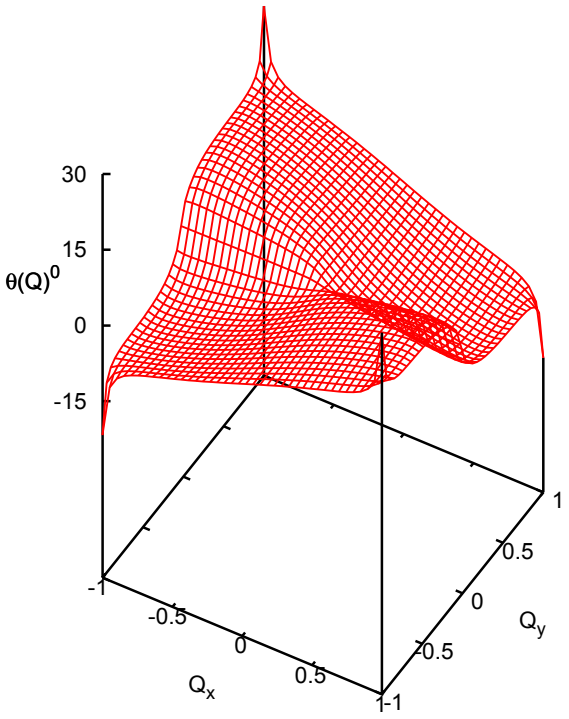

Figure 6.1: Adiabatic to diabatic mixing angle ($\theta(Q)$) as a function of the vibrational bending coordinates Q_x and Q_y.

Figs. 6.2 and 6.3 show the matrix elements (with electronic basis functions ψ_x, ψ_y)

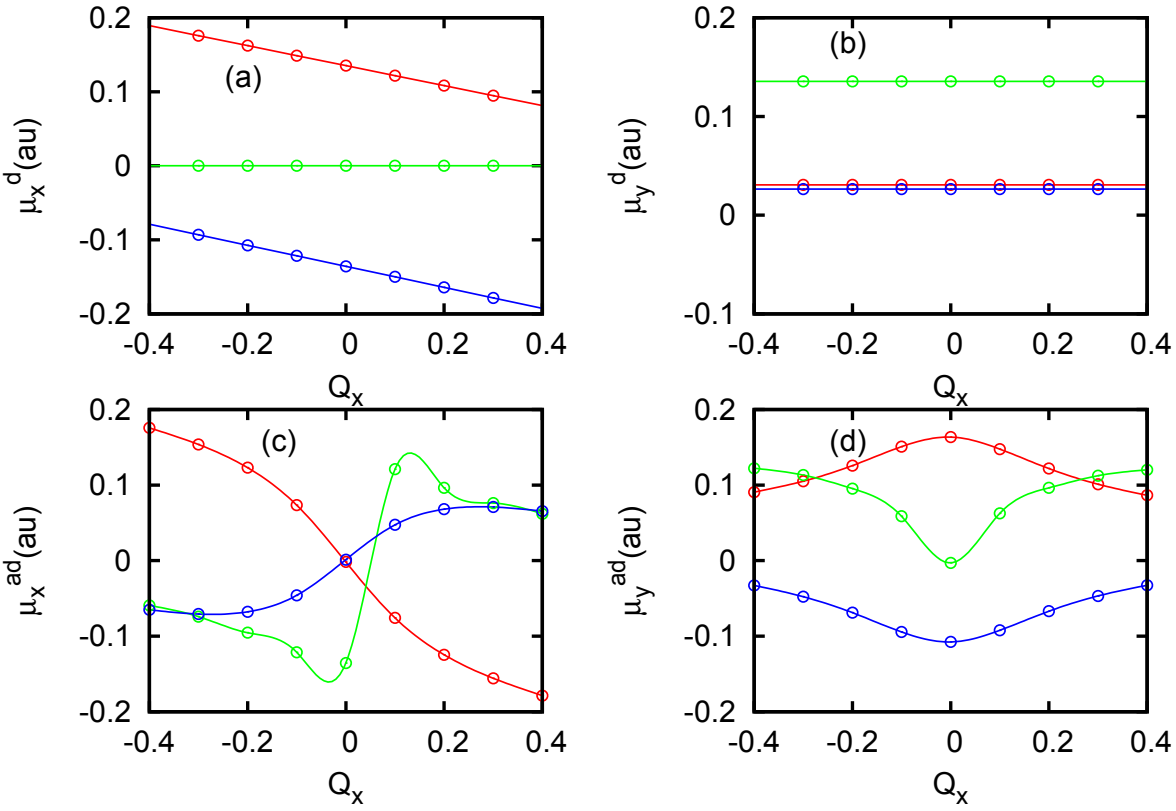

Figure 6.2: Adiabatic (lower panels) and diabatic (upper panels) dipole moment cuts for the $^5E''$ state of MnF_3 along the degenerate bending mode Q_x for a fixed value of Q_y = -0.2. Lower (c) and upper (a) left panels correspond to the adiabatic and diabatic μ_x along Q_x, lower (d) and upper (b) right panels correspond to the adiabatic and diabatic μ_y along Q_x. In the upper panels, circles correspond to the diabatic μ's (transformed from adiabatic *ab initio* data using the ADT) and solid lines correspond to the fitted dipole moment functions. In the lower panels, solid lines with circles correspond to the *ab initio* adiabatic dipole moments. The red and the blue lines and symbols represent the dipole moment expectation values $\langle\psi_x|\mu_k|\psi_x\rangle$, $\langle\psi_y|\mu_k|\psi_y\rangle$, respectively and the green lines and symbols correspond to the TDM $\langle\psi_x|\mu_k|\psi_y\rangle$ $(k = x, y)$.

of the x and y components of dipole moment ($\mu_{k,xx}$, $\mu_{k,xy}$, $\mu_{k,yy}$ where $k = x, y$) for the E'' state of MnF_3 along the dimensionless normal coordinate Q_x for fixed values of Q_y, - 0.2 and - 0.4, respectively. While the lower (c) and upper (a) left panels represent to the adiabatic and diabatic μ_x along Q_x, the lower (d) and upper (b) right panels represent the adiabatic and diabatic μ_y along Q_x, respectively. In the upper panels, circles correspond to the diabatic μ's (transformed from adiabatic *ab initio* data using the ADT) and solid lines correspond to the fitted dipole moment functions. In the lower panels, solid lines with circles correspond to the *ab initio* adiabatic dipole moments. Here adiabatic μ_x refers to the matrix elements of μ_x with adiabatic electronic basisfunctions and diabatic

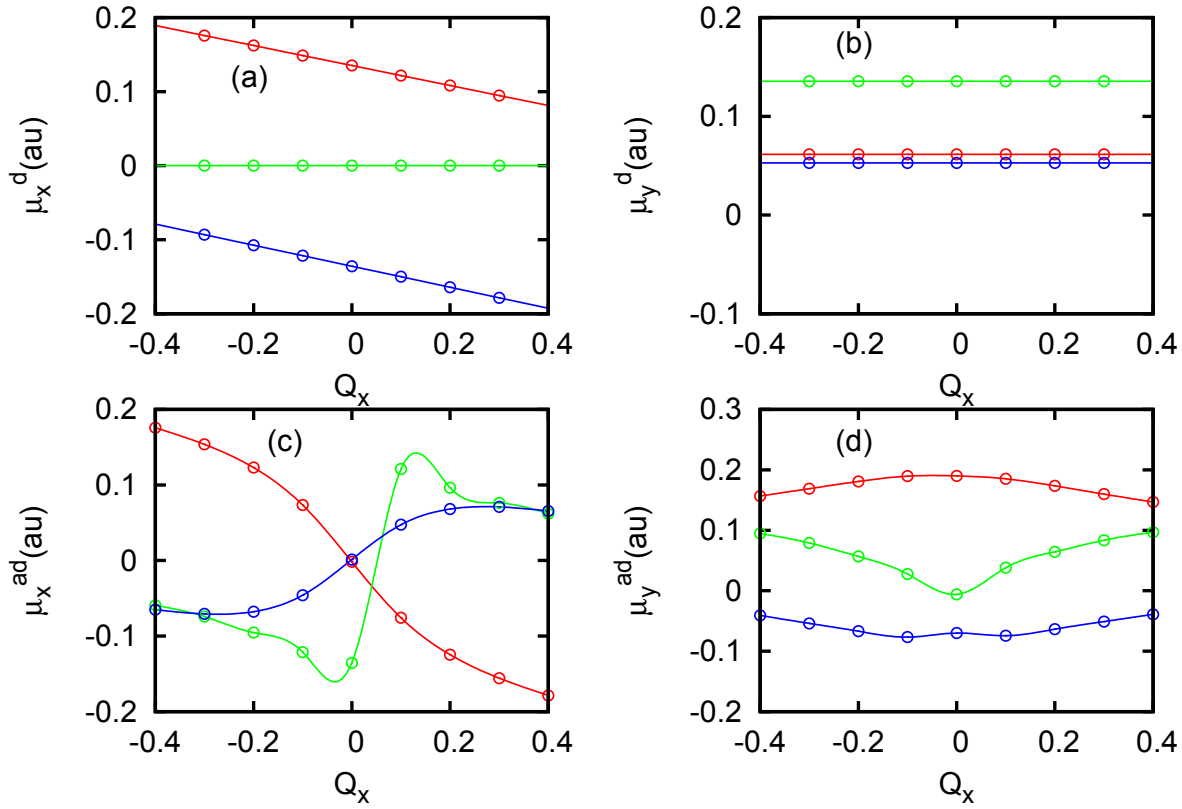

Figure 6.3: Adiabatic (lower panels) and diabatic (upper panels) dipole moment cuts for the $^5E''$ state of MnF_3 along the degenerate bending mode Q_x for a fixed value of Q_y = - 0.4. For further explanations, see the caption of Fig. 6.2.

μ_x refers to the matrix elements of μ_x with diabatic electronic basisfunctions.

Figs. 6.4 and 6.5 show the matrix elements of the the dipole moment components

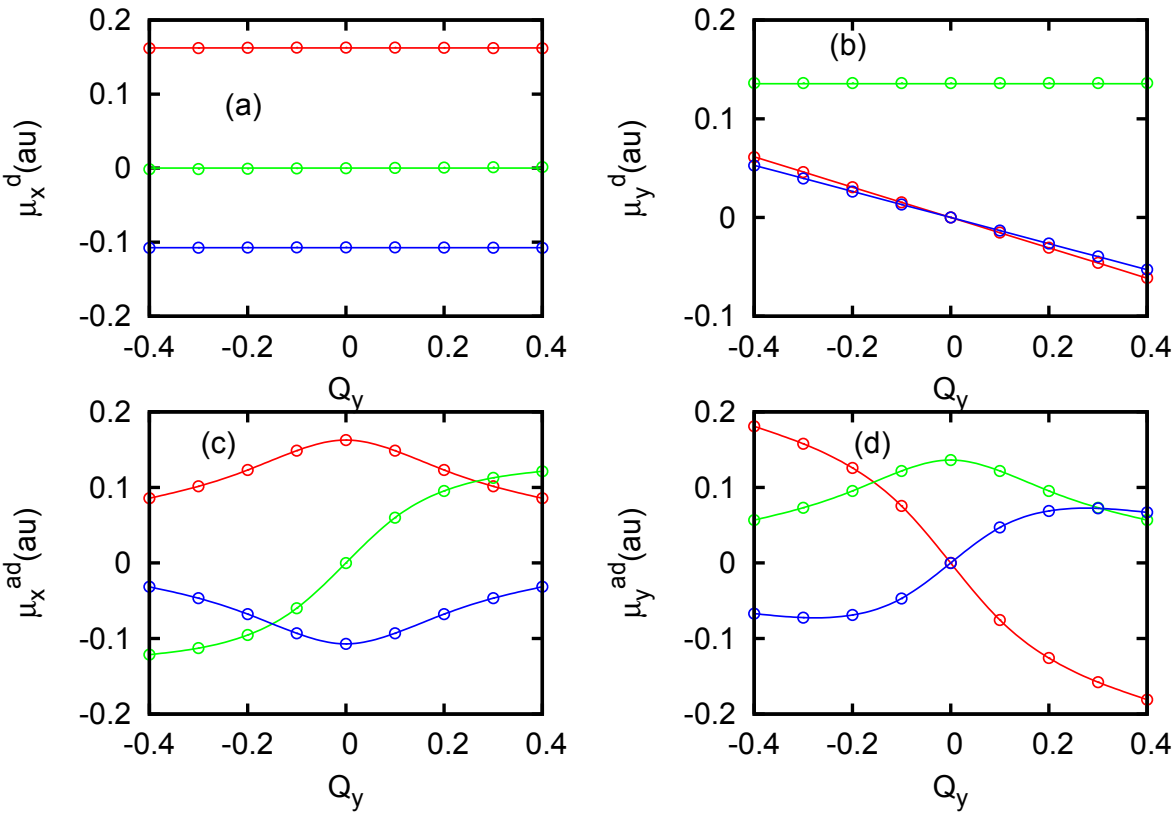

Figure 6.4: Adiabatic (lower panels) and diabatic (upper panels) dipole moment cuts for the ${}^5E''$ state of MnF_3 along the degenerate bending mode Q_y for a fixed value of Q_x = - 0.2.

μ_x and μ_y for the E'' state of MnF_3 along the dimensionless normal coordinate Q_y for fixed values of Q_x, - 0.2 and - 0.4, respectively. The lower panels show the adiabatic dipole moment functions and the upper panels panels show the diabatic dipole moment functions obtained by the ADT. In the upper panels, circles correspond to the diabatic μ's (transformed from adiabatic *ab initio* data) and solid lines correspond to the fitted dipole moment functions. In the lower panels, solid lines with circles correspond to the *ab initio* adiabatic dipole moments. In each of the subfigures, the red and blue lines and symbols correspond to the dipole moment expectation values $\langle\psi_x|\mu_k|\psi_x\rangle$ ($\mu_{k,xx}$), $\langle\psi_y|\mu_k|\psi_y\rangle$ ($\mu_{k,yy}$), respectively, and the green lines and symbols correspond to the TDM $\langle\psi_x|\mu_k|\psi_y\rangle$ ($\mu_{k,xy}$) with $k = x, y$. It can be seen that the adiabatic TDM (green lines) are rapidly varying functions of the nuclear geometry in the vicinity of the CI (see Figs. 6.2c, 6.3c, 6.4c, 6.5c and 6.2d, 6.3d, 6.4d, 6.5d). The unitary transformation by the ADT matrix (Eq.(2.11)) results in smoothly-varying dipole moments as a function of the nuclear geometry (Figs. 6.2a, 6.3a, 6.4a, 6.5a and 6.2b, 6.3b, 6.4b, 6.5b). The smoothness of the TDM functions is a control criterion for the validity of the construction of quasidiabatic wavefunctions.

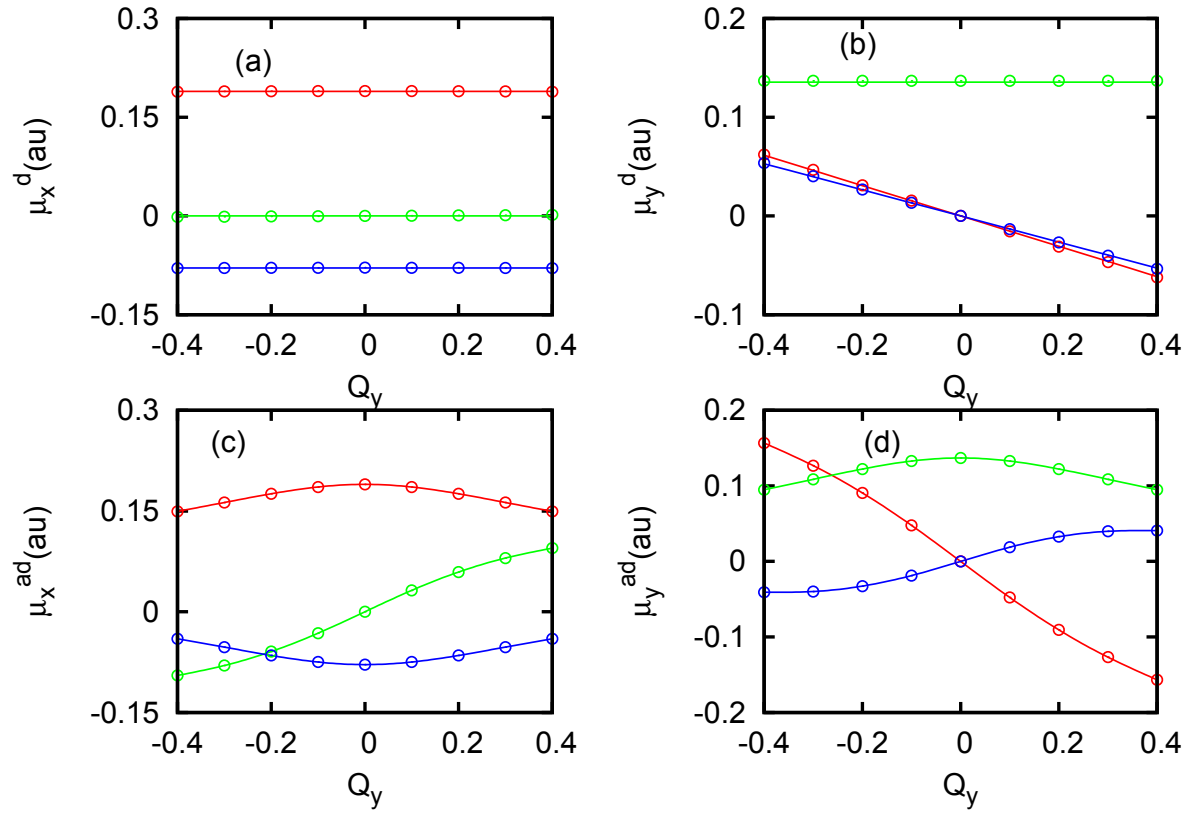

Figure 6.5: Adiabatic (lower panels) and diabatic (upper panels) dipole moment cuts for the $^5E''$ state of MnF_3 along the degenerate bending mode Q_y for a fixed value of Q_x = - 0.4.

components	$\mu^0_{ex,xx}$	$\mu^0_{ex,yy}$	$\mu^0_{ex,xy}$	$\mu'_{nx,x,xx}$	$\mu'_{nx,y,xx}$	$\mu'_{nx,x,yy}$	$\mu'_{nx,y,yy}$
x	0.135331	-0.135755	0.00	-0.135001	0.0	-0.142091	0.0
components	$\mu^0_{ey,xx}$	$\mu^0_{ey,yy}$	$\mu^0_{ey,xy}$	$\mu'_{ny,x,xx}$	$\mu'_{ny,y,xx}$	$\mu'_{ny,x,yy}$	$\mu'_{ny,y,yy}$
y	0.00	0.00	0.135587	0.0	-0.153695	0.0	-0.132187

Table 6.1: Dipole moment parameters for the E'' state of MnF_3 (in atomic units). $\mu^{(0)}_{ex,xx}$, $\mu^{(0)}_{ex,yy}$ are the zeroth-order dipole moment matrix elements, and $\mu^{(0)}_{ex,xy}$ is the TDM matrix element for the x component of the electronic dipole moment operator, see Eq. (F.2). $\mu'_{nx,x,xx}$ and $\mu'_{nx,y,yy}$ (see Eq. (F.5)) are the derivatives of the dipole moment matrix elements of the x-component of the nuclear dipole moment operator with respect to the nuclear coordinates Q_x and Q_y, respectively. Analogous definitions apply for the y-component.

The ADT allows the fitting of the dipole moment expectation values as well as TDM with linear functions in Q_x and Q_y.

It has been checked that the calculation of the DMS from -0.5 to 0.5 in Q_x and Q_y is sufficient for the fitting of linear dipole moment functions and extraction of the TDM and dipole moment derivatives for the E'' state of MnF_3. Figs. 6.2a, 6.3a, 6.4a and 6.5a reveal that the expectation value of dipole moment component μ_x is a linear function of Q_x and constant along Q_y in the diabatic representation. Figs. 6.2b, 6.3b, 6.4b and 6.5b reveal that the expectation value of dipole moment component μ_y is constant along Q_x and a linear function of Q_y, in the diabatic representation. The dipole moment parameters, extracted from the *ab initio* DMS by least-squares fitting, are given in Table 6.1. Details of the fitting of the DMS and the determination of dipole moment parameters are discussed in Appendix E. It should be noted that the Condon approximation is accurate for the electronic TDM.

6.2.2 Internal vibronic spectra

Using the TDM and the dipole moment derivatives determined by the fitting of the DMS, internal vibronic spectra have been calculated (see Section 3.5 and Appendix F). The eigenvalues and the components of the eigenvectors were calculated employing the linear-plus-quadratic JT (or JT-SO) Hamiltonian using the time-independent approach, see Section 3.3. Only absorption spectra are considered here.

Fig. 6.6a shows the internal vibronic spectra for the $^5E''$ state of MnF_3, considering the bending vibrational mode without inclusion of SO coupling and T = 0. Intensities near the origin of the spectrum refer to vibrational transitions (contribution from the dipole moment derivatives). The higher-energy part of the spectrum, i.e. the energy range [0.03 eV - 0.3 eV] shows the transitions from the lower sheet to the upper sheet of the adiabatic surface (intersheet transitions) of the E'' state which gain intensity from the nonzero transition dipole moment). The intensities in the energy range [0 eV - 0.03 eV] have contributions from both the nuclear and the electronic dipole moments. Since the intensities of intersheet transitions are small compared to the intrasheet transitions,

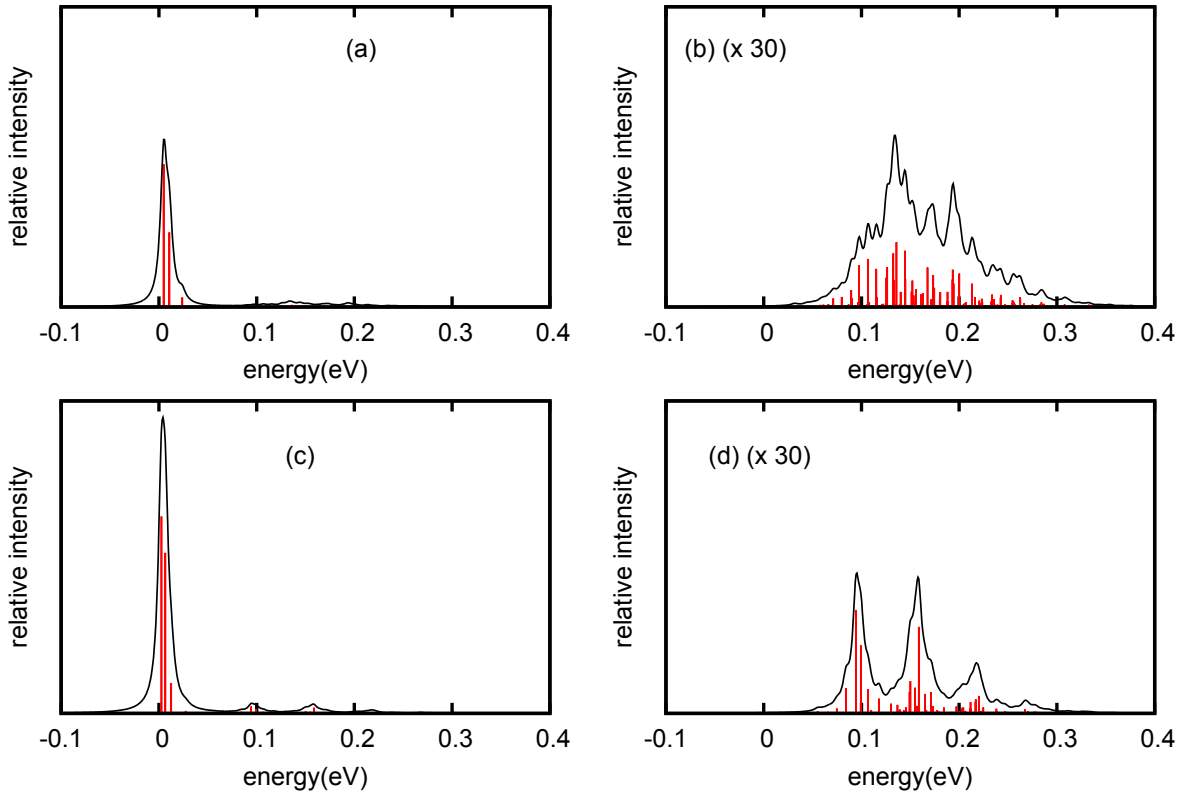

Figure 6.6: Internal vibronic spectra for the $^5E''$ state of MnF_3 considering the bending vibrational mode at T = 0 K without (a) and with (c) inclusion of SO coupling. (b) and (d) show the intersheet transitions of (a) and (c), respectively, on an enlarged scale (30 times).

the spectrum of intersheet transitions is shown in Fig. 6.6b on an enlarged scale.

Fig. 6.6c shows the internal vibronic spectra for the ${}^5E''$ state of MnF_3 considering the bending vibrational mode with inclusion of SO coupling and T = 0. The spectrum is more structured, especially at the higher-energy part due to the separation of the adiabatic PE surfaces by the SO splitting of the ${}^5E''$ state (see Eqs. (3.87, 3.92)). The spectrum of intersheet transitions with inclusion of SO coupling is shown in Fig. 6.6d on an enlarged scale. It also reveals the reduction of nonadiabatic coupling due to the separation of the adiabatic surfaces by the SO splitting.

Fig. 6.7 shows the comparison of internal vibronic spectra calculated for different

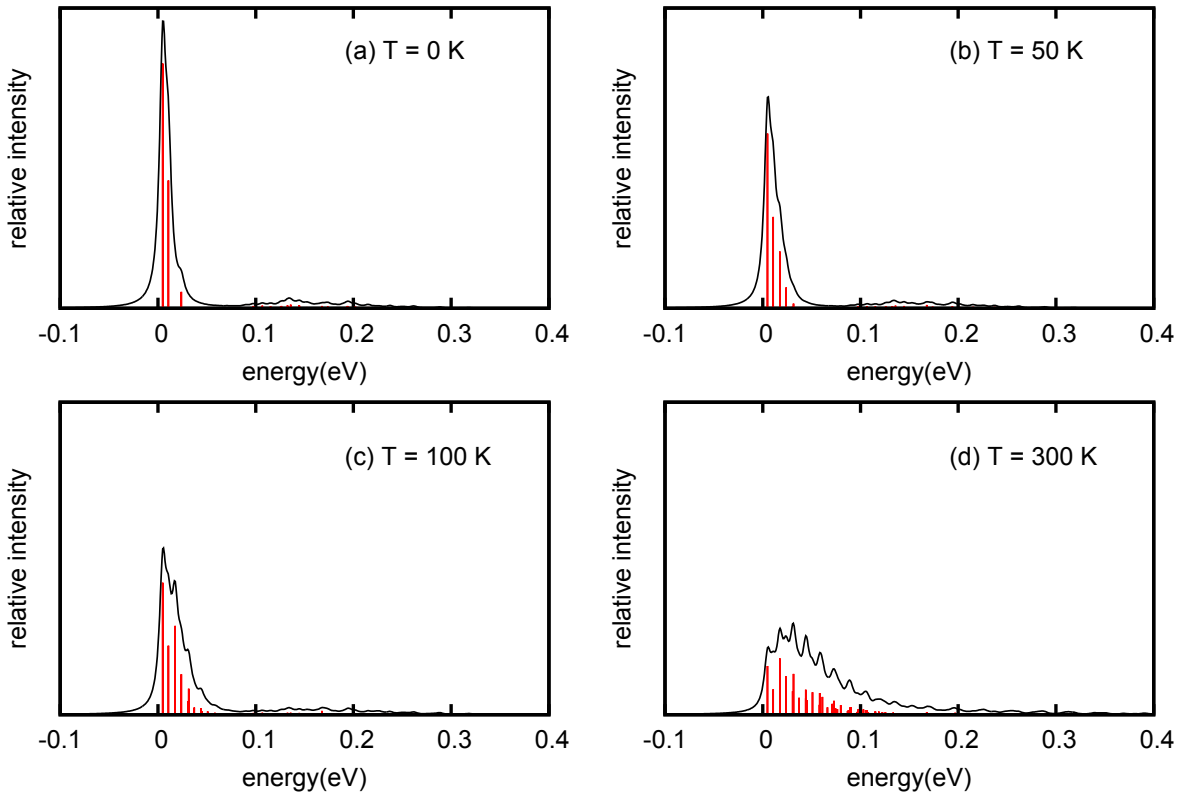

Figure 6.7: Internal vibronic spectra for the ${}^5E''$ state of MnF_3 considering the bending vibrational mode at different temperatures T = 0 K (a) T = 50 K (b) T = 100 K (c) T = 300 K (d).

temperatures, T = 0 K (a) T = 50 K (b) T = 100 K (c) and T = 300 K (d) without inclusion of SO coupling. It is clearly seen that with increasing temperature transitions to higher vibronic levels gain intensity and the total line density increases as well. For higher temperatures,the intensities arising from the pure vibrational part (nuclear dipole moment derivative) and the intensities arising from the TDM begin to merge and a single band is found at room temperature (T = 300 K, see Fig. 6.7d).

Fig. 6.8 shows the internal vibronic spectra calculated with inclusion of SO coupling for the temperatures T = 0 K (a) T = 50 K (b) T = 100 K (c) and T = 300 K (d). The

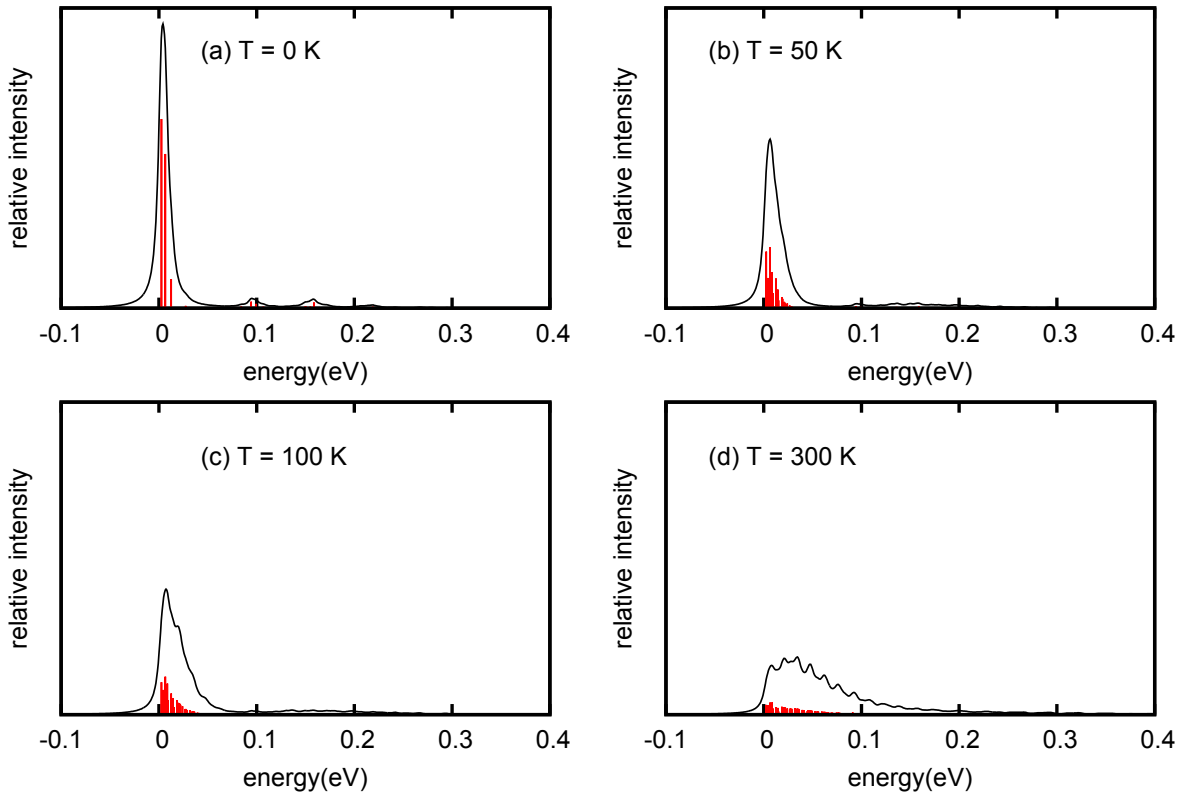

Figure 6.8: Internal vibronic spectra for the $^5E''$ state of MnF_3 considering the bending vibrational mode with inclusion of SO coupling at different temperatures T = 0 K (a) T = 50 K (b) T = 100 K (c) T = 300 K (d).

effect of SO coupling is less pronounced as temperature increases. It is seen that the line density increases substantially by the inclusion of SO coupling, in particular at higher temperatures.

6.3 NiF_3 - The $^4E'$ state

6.3.1 Dipole moment and transition dipole moment surfaces

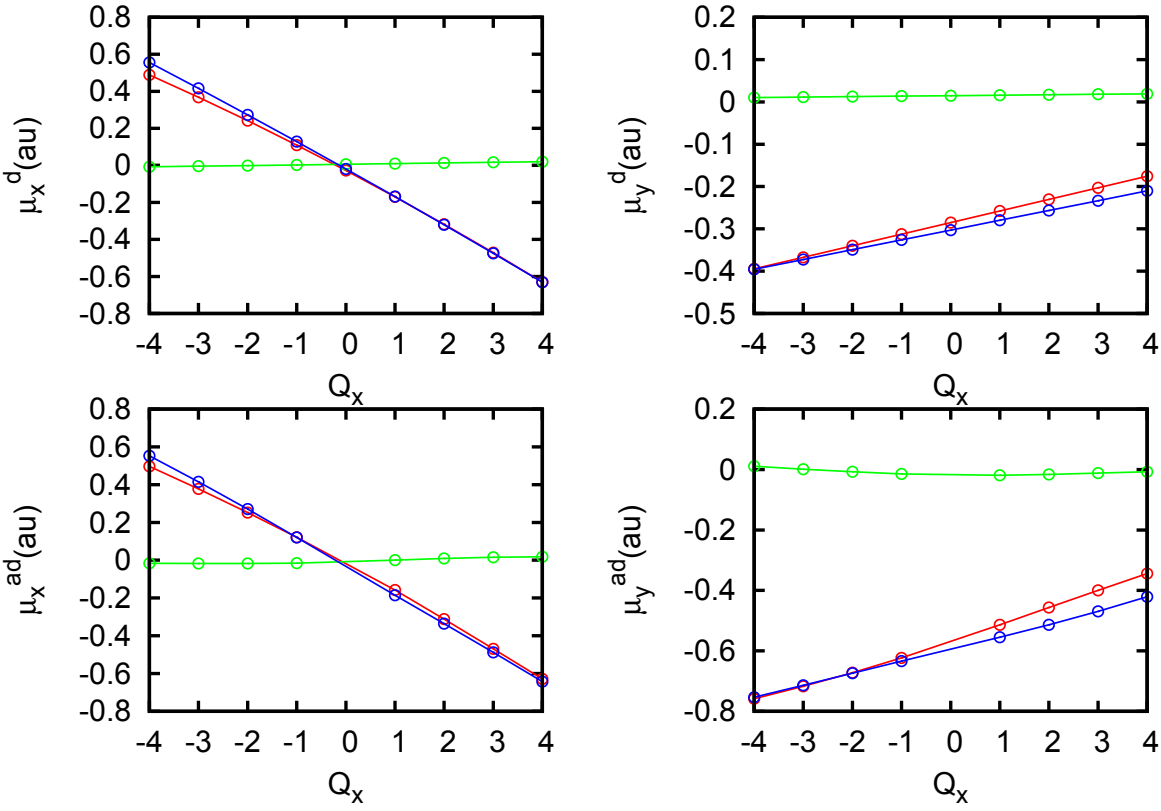

Figure 6.9: Adiabatic (lower panels) and diabatic (upper panels) dipole moment cuts for the $^4E'$ state of NiF_3 along the degenerate bending mode Q_x for a fixed value of $Q_y = 2.0$. Lower (c) and upper (a) left panels correspond to the adiabatic and diabatic μ_x, respectively, along Q_x, lower (d) and upper (b) right panels correspond to the adiabatic and diabatic μ_y, respectively, along Q_x. Circles and solid lines in (a) and (b) correspond to diabatized *ab initio* data and the fitted dipole moment functions, respectively. Solid lines with circles in (c) and (d) correspond to the adiabatic *ab initio* data. The red and the blue lines and symbols represent the dipole moment expectation values $\langle\psi_x|\mu|\psi_x\rangle$, $\langle\psi_y|\mu|\psi_y\rangle$, respectively and the green lines and symbols represent the TDM $\langle\psi_x|\mu|\psi_y\rangle$.

Figs. 6.9 and 6.10 show the matrix elements (with electronic basis functions ψ_x, ψ_y) of the x and y components of dipole moment operator ($\mu_{k,xx}$, $\mu_{k,xy}$ and $\mu_{k,yy}$) for the E'

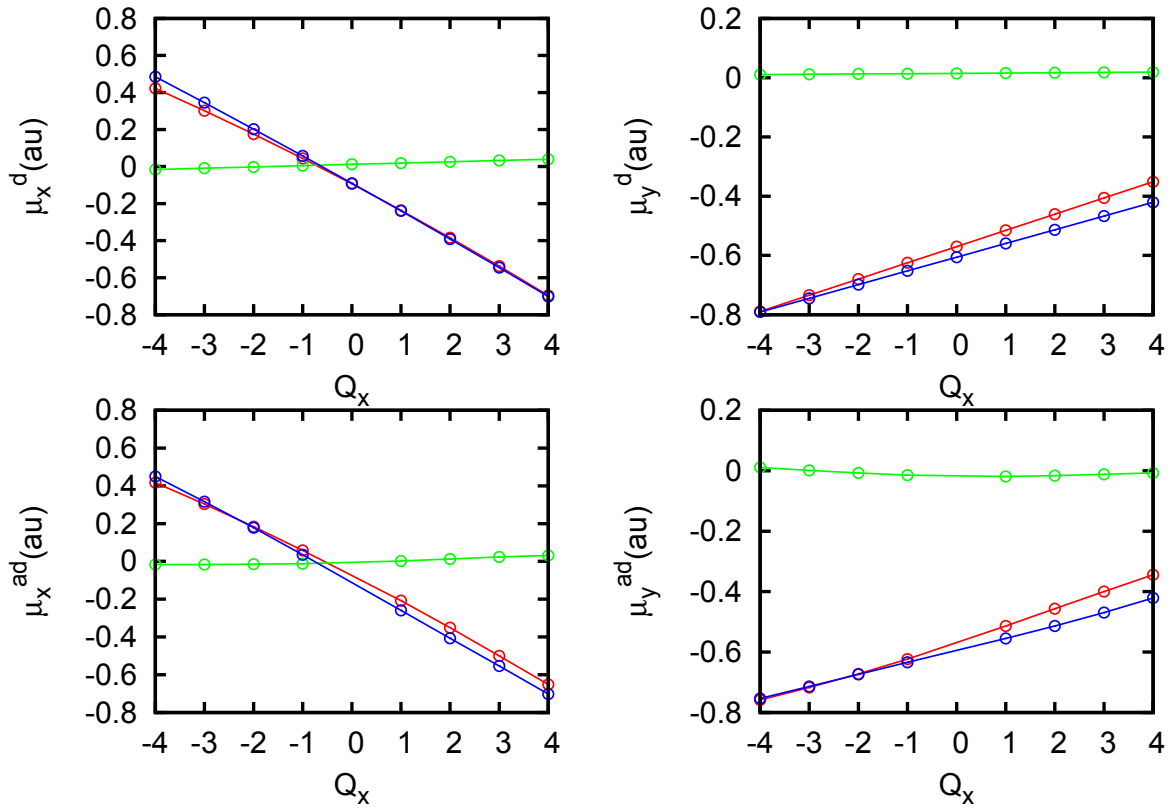

Figure 6.10: Adiabatic (lower panels) and diabatic (upper panels) dipole moment cuts for the $^4E'$ state of NiF_3 along the degenerate bending modes Q_x for a fixed value of $Q_y = 4.0$.

state of NiF_3 along the dimensionless normal coordinate Q_x for fixed values 2.0 and 4.0 of Q_y, respectively. While the lower (c) and upper (a) left panels represent the adiabatic and diabatic μ_x along Q_x, the lower (d) and upper (b) right panels correspond to the adiabatic and diabatic μ_y along Q_x, respectively. In the upper panels, circles correspond to the diabatic μ's (transformed from adiabatic *ab initio* data using the ADT) and solid lines correspond to the fitted dipole moment functions. In the lower panels, solid lines with circles correspond to the *ab initio* adiabatic dipole moments and TDM.

Figs. 6.11 and 6.12 show the matrix elements of the dipole moment components μ_x and

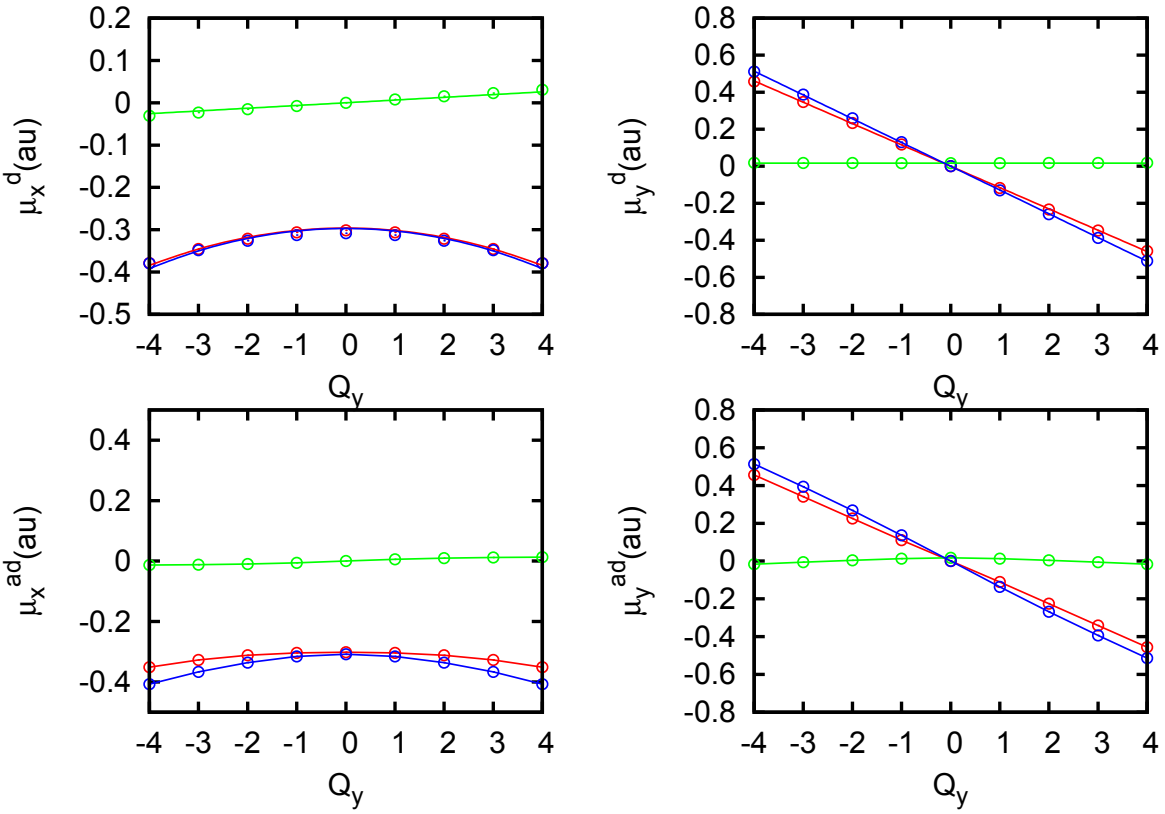

Figure 6.11: Adiabatic (lower panels) and diabatic (upper panels) dipole moment cuts for the $^4E'$ state of NiF_3 along the degenerate bending modes Q_y for a fixed value of $Q_x = 2.0$.

μ_y for the E' state of NiF_3 along dimensionless normal coordinate Q_y for fixed values of Q_x, 2.0 and 4.0, respectively. The lower panels show the adiabatic dipole moment functions and the upper panels show the diabatic dipole moment functions obtained by the ADT In the upper panels, circles correspond to the diabatic μ's (transformed from adiabatic *ab initio* data using the ADT) and solid lines correspond to the fitted dipole moment functions. In the lower panels, solid lines with circles correspond to the *ab initio* adiabatic dipole moments. In each of the subfigures, the red and blue lines and symbols correspond to the dipole moment expectation values $\langle\psi_x|\mu_k|\psi_x\rangle$ $(\mu_{k,xx})$, $\langle\psi_y|\mu_k|\psi_y\rangle$ $(\mu_{k,yy})$, respectively, and the green lines and symbols correspond to the TDM $\langle\psi_x|\mu_k|\psi_y\rangle$ $(\mu_{k,xy})$

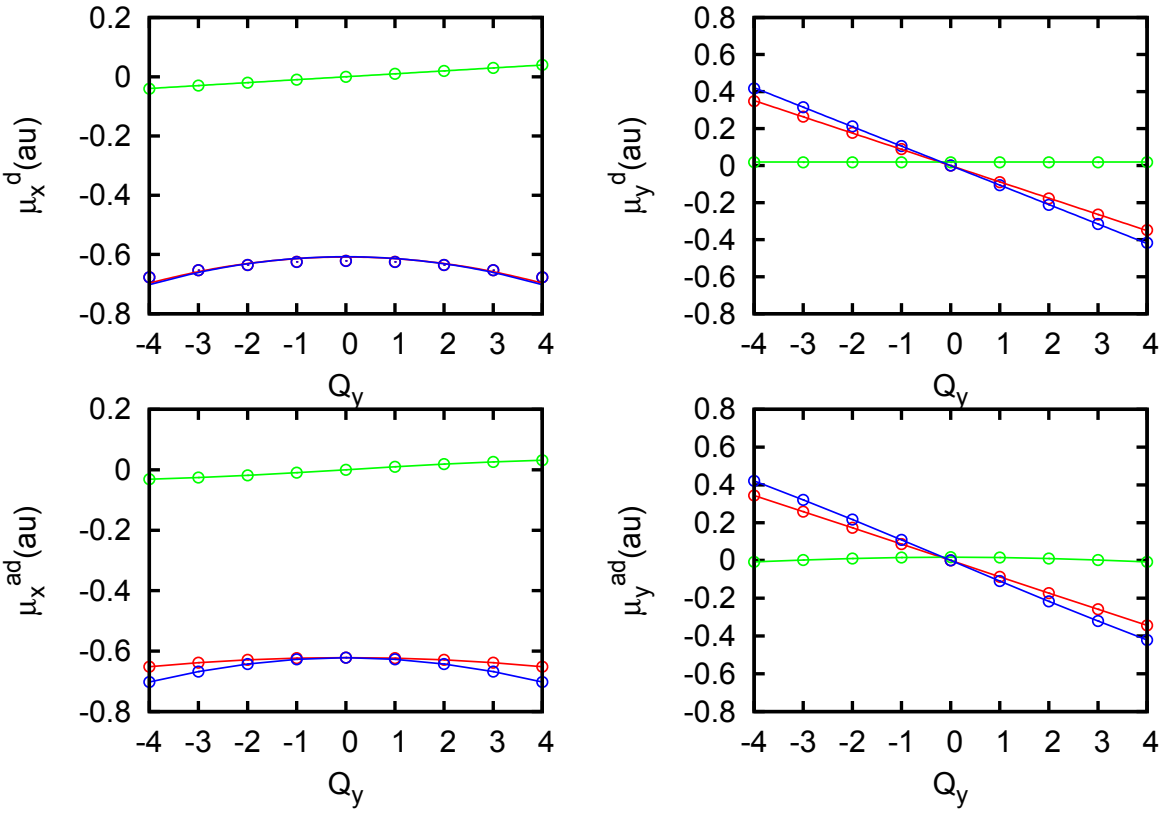

Figure 6.12: Adiabatic (lower panels) and diabatic (upper panels) dipole moment cuts for $^4E'$ state of NiF_3 along the degenerate bending modes Q_y for a fixed value of $Q_x = 4.0$.

components	$\mu^{(0)}_{ex,xx}$	$\mu^{(0)}_{ex,yy}$	$\mu^{(0)}_{ex,xy}$	$\mu'_{nx,x,xx}$	$\mu'_{nx,y,xx}$	$\mu'_{nx,x,yy}$	$\mu'_{nx,y,yy}$
x	-0.005698	0.005482	0.0	-0.139922	0.0	-0.148441	0.0
components	$\mu^{(0)}_{ey,xx}$	$\mu^{(0)}_{ey,yy}$	$\mu^{(0)}_{ey,xy}$	$\mu'_{ny,x,xx}$	$\mu'_{ny,y,xx}$	$\mu'_{ny,x,yy}$	$\mu'_{ny,y,yy}$
y	0.00	0.00	0.014735	0.0	-0.142541	0.0	-0.151468

Table 6.2: Dipole moment parameters for the E' state of NiF_3 (in atomic units). $\mu^{(0)}_{ex,xx}$, $\mu^{(0)}_{ex,yy}$ are the zeroth-order dipole moment matrix elements, and $\mu^{(0)}_{ex,xy}$ is the TDM matrix element of the x component of the electronic dipole moment operator, see Eq. (F.2). $\mu'_{nx,x,xx}$ and $\mu'_{nx,y,yy}$ (see Eq. (F.5)) are the derivatives of the dipole moment matrix elements of the x component of the nuclear dipole moment operator with respect to the nuclear coordinates Q_x and Q_y, respectively.

with $k = x, y$. It should be noted that although the *ab initio* adiabatic dipole moments and TDM are smoothly varying function of vibrational coordinates in case of E' state of NiF_3 and thus ADT as such is not needed, but the fitting has been done in the diabatic representation for consistency.

It has been checked that the calculation of the DMS from -5.0 to 5.0 in Q_x and Q_y is sufficient for the fitting of dipole moment functions to determine the TDM and dipole moment derivatives for the E' state of NiF_3. A full quadratic expansion of dipole moment function is necessary for a good fitting. The dipole moment parameters are extracted from the diabatic DMS by a least-squares fitting procedure using a quadratic function in Q_x and Q_y. Since the parameters from the quadratic expansions are too small to affect the spectra, only the parameters upto linear expansion of dipole moment functions are given in Table 6.2 and are used to calculate the internal vibronic spectra. Details of the fitting of the DMS and the determination of the dipole moment parameters are discussed in Appendix E.

6.3.2 Internal vibronic spectra

Fig. 6.13 shows the internal vibronic spectra for the $^4E'$ state of NiF_3 considering the bending vibrational mode at T = 0 K without (a) and with (c) inclusion of SO coupling and T = 0. In Fig. 6.13a, the first transition, to an energy level which is very close to the ground vibrational level, is a consequence of strong quadratic JT coupling. In this case the first excited vibrational level approches to the doubly-degenerate ground vibrational level rendering it approximately triply degenerate. In the $^4E'$ state of NiF_3, the intersheet transitions begin at an energy of about 0.2 eV. Their intensities are too small to be visible in the same scale as intrasheet vibrational transition. The intersheet transitions are shown in Fig. 6.13b (without SO coupling) and Fig. 6.13d (with SO coupling) on an enlarged scale to become visible. The very dense and erratic line structure in Fig. 6.13b reflects the strong nonadiabatic coupling of the upper adiabatic JT surface. With inclusion of the SO coupling, which is rather large in the $^4E'$ state of NiF_3, the nonadiabatic coupling of the adiabatic JT energy surfaces is substantially reduced. As a result, a Frank-Condon

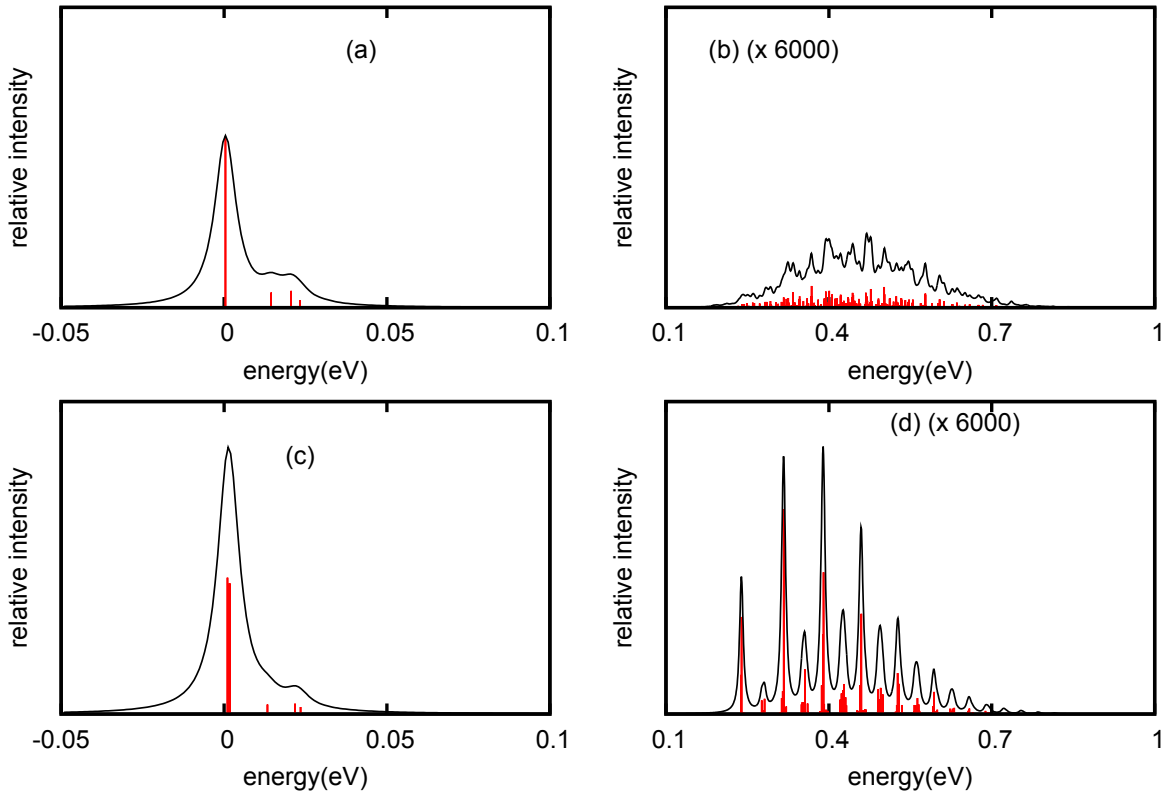

Figure 6.13: Internal vibronic spectra for the $^4E'$ state of NiF_3 considering the bending vibrational mode at T = 0 K without (a) and with (c) inclusion of SO coupling. (b) and (d) show the intersheet transitions at T = 0 K with and without SO coupling, respectively, on an enlarged scale.

like progression is observed in the low-resolution spectrum of Fig. 6.13d. Note, however, the clumps of lines in the high-resolution spectrum of Fig. 6.13d. The high line density in these clumps reflect the nonadiabatic coupling of the upper adiabatic JT-SO surface to the lower adiabatic surface.

Fig. 6.14 shows the internal vibronic spectra for $^4E'$ state of NiF_3, considering the

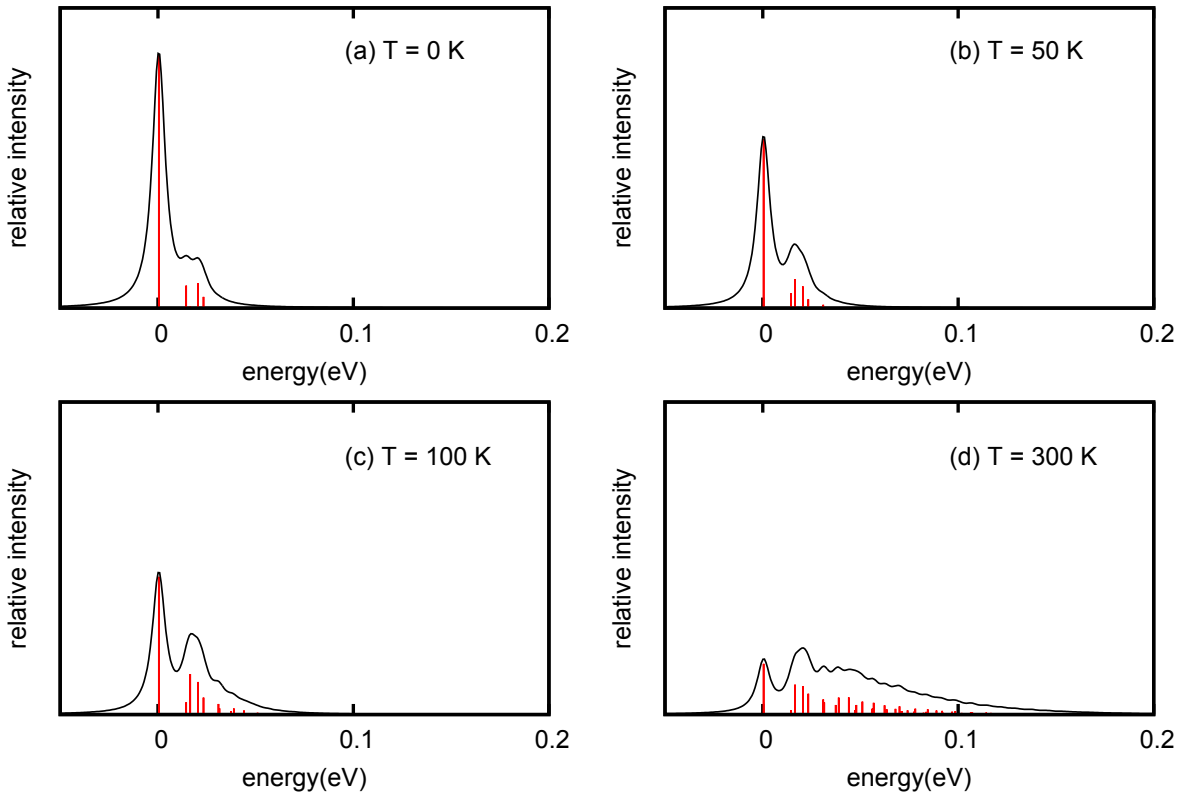

Figure 6.14: Internal vibronic spectra for the $^4E'$ state of NiF_3 considering the bending vibrational mode for different temperatures T = 0 K (a) T = 50 K (b) T = 100 K (c) and T = 300 K (d).

bending vibrational mode and the temperatures, T = 0 K (a) T = 50 K (b) T = 100 K (c) and T = 300 K (d). Since the intersheet transitions are not visible here, only the intrasheet transitions are shown on an expanded energy scale. The effect of temperature on the vibrational spectra of the $^4E'$ state of NIF_3 is similar to the $^5E''$ state of MnF_3. The spectral range broadens as the tempreature increases. At T = 0 K, the first peak of the low-resolution spectrum has higher intensity than the second peak. As temperature increases, second peak in the low-resolution spectra increases in intensity and becomes the highest peak at T = 300 K.

Fig. 6.15 shows the internal vibronic spectra for the $^4E'$ state of NiF_3 considering the bending vibrational mode with inclusion of SO coupling at different temperatures T = 0 K (a) T = 50 K (b) T = 100 K (c) and T = 300 K (d). Only the intrasheet transitions are shown. The effect of SO coupling becomes less pronounced as temperature increases.

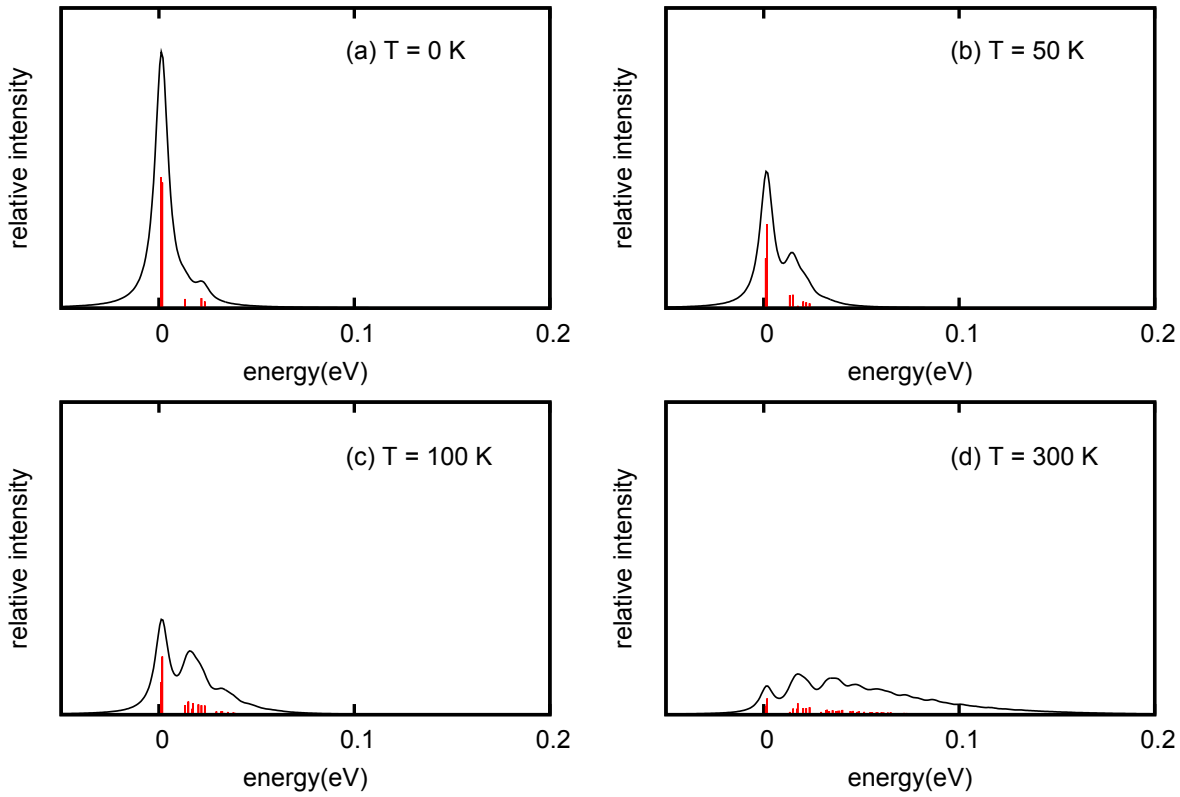

Figure 6.15: Internal vibronic spectra for the $^4E'$ state of NiF_3 considering the bending vibrational mode with inclusion of SO coupling at different temperatures T = 0 K (a) T = 50 K (b) T = 100 K (c) and T = 300 K (d).

Chapter 7

Summary and outlook

The purpose of this thesis is the investigation of the combined effects of JT and SO coupling on the electronic and vibrational spectra of first-row transition-metal trifluorides. The JT-SO model Hamiltonian used in this work is a combination of the electrostatic (JT) Hamiltonian and the microscopic BP SO Hamiltonian. SO coupling is thus treated as a perturbation of the electrostatic Hamitonian. In case of systems with strong JT couplings, the electrostatic Hamiltonian has been expanded beyond the standard model, i.e. a higher-order (beyond second order) expansion has been employed. The BP SO Hamiltonian matrices derived by Poluyanov and Domcke[30] are employed for the calculation of JT-SO spectra of electronic states with high-spin multiplicities. The so-called external (electronic) and the so-called internal (vibrational) vibronic spectra are calculated and discussed with and without inclusion of SO coupling.

The combined effects of JT coupling and SO coupling on the adiabatic PE surfaces and the external vibronic spectra of TiF_3, CrF_3 and NiF_3 (systems with odd number of unpaired electrons) and MnF_3, CoF_3 (systems with even number of unpaired electrons) have been investigated. Any combination of weak or strong JT couplings and weak or strong SO couplings can be found in the transition-metal trifluorides.

The adiabatic PE surfaces of the ${}^M E'$ and ${}^M E''$ ($M = 2, 4, 5$ are spin multiplicities) electronic states of TiF_3, CrF_3, MnF_3, CoF_3 and NiF_3 have been calculated with the CASSCF method. The SO splittings and the JT coupling parameters (up to sixth order in the normal-mode displacements) have been determined. It has been shown that the *ab initio* PE surfaces are accurately reproduced at this level of JT theory. The doublet E states of TiF_3 and the quartet E states of CrF_3 and NiF_3 exhibit the characteristic mutual quenching of JT and SO coupling. They split into M doubly degenerate surfaces with inclusion of SO coupling (Kramers degeneracy). The ${}^2E'$ state of TiF_3 and the ${}^4E'$ state of CrF_3 exhibit strong JT effects and rather weak SO splitting. The ${}^4E'$ state of NiF_3 exhibits strong linear and quadratic JT coupling combined with strong SO coupling. For the quintet E states of MnF_3 and CoF_3, two of the ten JT surfaces are unaffected by SO coupling, while SO coupling tends to quench the JT effect for the other surfaces. While the ${}^5E'$ state of MnF_3 exhibits a strong JT effect and weak SO splitting, the ${}^5E'$ state of CoF_3 exhibits strong JT coupling combined with strong SO coupling. Comparatively weak JT and SO couplings have been found in case of the ${}^5E''$ states of CoF_3 and MnF_3. The JT stabilization energies determined in the quadratic approximation are in

good agreement with the few previous results.

We have presented the *ab initio* calculated external vibronic spectra of ${}^{M}E$ states of MF_3 molecules, where M = Ti, Cr, Mn, Co and Ni. The external vibronic spectra have been computed with the inclusion of JT coupling up to sixth-order and fourth-order in JT-active bending and stretching modes, respectively. The nonseparability of the JT active bending and stretching vibrations (the $E \times (e + e)$ JT effect) has been taken into account. For the examples of the ${}^{2}E'$ state of TiF_3, the ${}^{4}E'$ state of NiF_3 and the ${}^{5}E'$ state of MnF_3, the inclusion of higher order JT coupling constants as well as the two-mode JT effect and the SO coupling effects have been outlined step by step to clarify the relevance of the various coupling mechanisms. For the other cases, only the final results obtained without and with SO coupling have been shown and discussed. The spectra calculated with inclusion of SO coupling are a superposition of two (for $M = 4$) or three (for $M = 5$) complicated JT-SO spectra. As seen in the JT-SO spectra in some cases (${}^{2}E'$ and ${}^{2}E''$ states of TiF_3, ${}^{4}E'$ state of CrF_3, ${}^{5}E'$ state of MnF_3), SO coupling is strongly quenched by a strong or moderately strong JT effect at the origin of the spectrum. The quenching factor[16] increases with the increase of JT coupling strength. The states where SO coupling and JT coupling are of equal strength (${}^{5}E''$ state of MnF_3 and ${}^{5}E''$ state of CoF_3), weak SO coupling is partially quenched by the moderate JT effect at the origin of the spectrum. For the rest of the cases (${}^{5}E'$ state of CoF_3 and ${}^{4}E'$ state of NiF_3), the partial quenching of the JT effects by the strong SO couplings (large splitting of the two humps in the low-resolution spectra) has been noticed. A strong quenching of the JT effect by strong SO coupling can be predicted to be found in second- and third-row transition-metal complexes. It would be very difficult to analyze these spectra without a detailed *ab initio* theoretical simulation.

For the calculation of internal vibronic spectra, the adiabatic DMS were calculated using the CASSCF method. The combined effects of JT and SO coupling in the internal vibronic spectra of the ${}^{5}E''$ state of MnF_3 and the ${}^{4}E'$ state of NiF_3 have been calculated and discussed. The combinations of weak JT and weak SO coupling (${}^{5}E''$ state of MnF_3) and strong JT coupling with strong SO coupling (${}^{4}E'$ state of NiF_3) have been analyzed.

The internal vibronic spectra provide additional insight into the JT and SO coupling effects in transition-metal trifluorides. In the internal vibronic spectra, the pseudorotational motion is reflected by vibronic transitions of unusually low-frequency. The structure of the intersheet spectra has been found to be very complicated due to the presence of strong nonadiabatic coupling effects. A pronounced effect of the SO coupling in the intersheet spectra has been found. The intersheet spectra become simpler and more structured upon inclusion of SO coupling.

The effect of temperature on the internal vibronic spectra has been explored and analyzed. Since the higher vibronic energy levels are initially populated, with increasing temperature, the line density of the spectra increases significantly. At T = 300 K, broad and unresolved IR spectra are predicted.

The results of this thesis represent the first *ab initio* study of the static and dynamic $E \times e$ JT effect with inclusion of SO coupling in transition-metal trifluorides. $(E + A) \times e$ and $(E + E) \times e$ PJT effects may exist in these systems, but have been ignored in this work. The interactions of ${}^{M}E$ states with states of the same or different spin multiplicity via the SO operator also have been neglected. In the future, such electrostatic as well

as SO-induced inter-state couplings should be included in the calculation of the spectra. The totally symmetric stretching mode and the umbrella mode should be included to obtain full-dimensional PE surfaces and full-dimensional vibronic spectra of transition-metal trifluorides. Analogous *ab initio* studies for second-row and third-row transition-metal halides, which exhibit stronger SO couplings, should be of interest. The present results illuminate the multitude of effects of JT and SO coupling in trigonal transition-metal complexes. It is another challenge for future research to extend the theory and the *ab initio* computations to tetrahedral and octahedral transition-metal complexes.

Part of the thesis has been published in the following two articles

- Ab initio study of dynamical $E \times e$ Jahn-Teller and spin-orbit coupling effects in the transition-metal trifluorides TiF_3, CrF_3 and NIF_3, P. Mondal, D. Opalka, L. V. Poluyanov and W. Domcke, J. Chem. Phys., 2012, **136**, 84308.

- Jahn-Teller and spin-orbit coupling effects in transition-metal trifluorides, P. Mondal, D. Opalka, L. V. Poluyanov and W. Domcke, Chem. Phys., 2011, **387**, 56.

Appendix A

Matrix elements of the spinless $E \times e$ JT Hamiltonian up to sixth order

The matrix elements $U^{(n)}$, $W^{(n)}$ and $Z^{(n)}$ (see Eq. (3.26)) are given by[74]

$$
\begin{aligned}
U^{(0)} &= {a_1}^{(0)} \\
U^{(1)} &= 0 \\
U^{(2)} &= {a_1}^{(2)}[{Q_x}^2 + {Q_y}^2] \\
U^{(3)} &= {a_1}^{(3)}[2{Q_x}^3 - 6Q_x{Q_y}^2] \\
U^{(4)} &= {a_1}^{(4)}[{Q_x}^4 + 2{Q_x}^2{Q_y}^2 + {Q_y}^4] \\
U^{(5)} &= {a_1}^{(5)}[2{Q_x}^5 - 4{Q_x}^3{Q_y}^2 - 6Q_x{Q_y}^4] \\
U^{(6)} &= {a_1}^{(6)}[2{Q_x}^6 - 30{Q_x}^4{Q_y}^2 + 30{Q_x}^2{Q_y}^4 - 2{Q_y}^6] + {a_2}^{(6)}[{Q_x}^6 + 3{Q_x}^4{Q_y}^2 + 3{Q_x}^2{Q_y}^4 + {Q_y}^6] \\
W^{(0)} &= 0 \\
W^{(1)} &= {\lambda_1}^{(1)}Q_x \\
W^{(2)} &= {\lambda_1}^{(2)}[{Q_x}^2 - {Q_y}^2] \\
W^{(3)} &= {\lambda_1}^{(3)}[{Q_x}^3 + Q_x{Q_y}^2] \\
W^{(4)} &= {\lambda_1}^{(4)}[{Q_x}^4 - 6{Q_x}^2{Q_y}^2 + {Q_y}^4] + {\lambda_2}^{(4)}[{Q_x}^4 - {Q_y}^4] \\
W^{(5)} &= {\lambda_1}^{(5)}[{Q_x}^5 - 10{Q_x}^3{Q_y}^2 + 5Q_x{Q_y}^4] + {\lambda_2}^{(5)}[{Q_x}^5 + 2{Q_x}^3{Q_y}^2 + Q_x{Q_y}^4] \\
W^{(6)} &= {\lambda_1}^{(6)}[{Q_x}^6 - 5{Q_x}^4{Q_y}^2 - 5{Q_x}^2{Q_y}^4 + {Q_y}^6] + {\lambda_2}^{(6)}[{Q_x}^6 + {Q_x}^4{Q_y}^2 - {Q_x}^2{Q_y}^4 - {Q_y}^6]
\end{aligned}
$$

$$
\begin{aligned}
Z^{(0)} &= 0 \\
Z^{(1)} &= {\lambda_1}^{(1)} Q_y \\
Z^{(2)} &= -2{\lambda_1}^{(2)} Q_x Q_y \\
Z^{(3)} &= {\lambda_1}^{(3)} [{Q_x}^2 Q_y + {Q_y}^3] \\
Z^{(4)} &= {\lambda_1}^{(4)} [4{Q_x}^3 Q_y - 4Q_x {Q_y}^3] + {\lambda_2}^{(4)} [-2{Q_x}^3 Q_y - 2Q_x {Q_y}^3] \\
Z^{(5)} &= {\lambda_1}^{(5)} [-5{Q_x}^4 Q_y + 10{Q_x}^2 {Q_y}^3 - {Q_y}^5] + {\lambda_2}^{(5)} [{Q_x}^4 Q_y + 2{Q_x}^2 {Q_y}^3 + {Q_y}^5] \\
Z^{(6)} &= {\lambda_1}^{(6)} [4{Q_x}^5 Q_y - 4Q_x {Q_y}^5] + {\lambda_2}^{(6)} [-2{Q_x}^5 Q_y - 4{Q_x}^3 {Q_y}^3 - 2Q_x {Q_y}^5]
\end{aligned}
$$

Appendix B

Trasformation of symmetry coordinates to normal coordinates and calculation of vibrational frequencies

Wilson's FG matrix method[78] has been used to transform symmetry coordinates (linear combinations of internal coordinates) to normal coordinates as well as to calculate vibrational frequencies of degenerate modes of e symmetry. The F and G matrices are related to the potential and kinetic energies of vibration, respectively, by the following relation

$$2V = S^{\dagger} F S \; ; \; 2T = \dot{S}^{\dagger} G^{-1} \dot{S} \tag{B.1}$$

where F and G are the force constant matrix and kinematic matrix, respectively, in symmetry coordinates. They are defined as

$$F = \begin{pmatrix} f_r - f_{rr} & f^{(1)}_{r\alpha} - 2f^{(2)}_{r\alpha} \\ f^{(1)}_{r\alpha} - 2f^{(2)}_{r\alpha} & f_\alpha - f_{\alpha\alpha} \end{pmatrix}, \tag{B.2}$$

$$G = \begin{pmatrix} g_r - g_{rr} & g^{(1)}_{r\alpha} - 2g^{(2)}_{r\alpha} \\ g^{(1)}_{r\alpha} - 2g^{(2)}_{r\alpha} & g_\alpha - g_{\alpha\alpha} \end{pmatrix}. \tag{B.3}$$

Here, r and α correspond to the internal stretching and bending coordinates. The elements of the G matrix for an MF_3 molecule are given by[78]

$$\begin{aligned} g_r &= \mu_M + \mu_F, \\ g_r &= \mu_M \cos\alpha_0, \\ g_\alpha &= 2[\mu_F + 2\mu_M \sin^2(\alpha_0/2)], \\ g^{(1)}_{r\alpha} &= -2\mu_M \sin\alpha_0 \cos\psi, \\ g^{(2)}_{r\alpha} &= -\mu_M \sin\alpha_0, \end{aligned} \tag{B.4}$$

$$g_{\alpha\alpha} = \mu_F \cos\psi + \mu_M[2\sin^2(\alpha_0/2)\cos\psi + \sin^2\alpha_0 \sin^2\psi],$$

where μ_M and μ_F are the inverse masses of M and F, α_0 and ψ are the equilibrium F-M-F angle and dihedral angle, respectively. For a molecule with D_{3h} symmetry, $\alpha_0 = 120^0$ and $\psi = 180^0$. The mass-weighted normal coordinates (q) are linearly related to the symmetry coordinates (S) by a transformation

$$S = Lq. \tag{B.5}$$

In normal coordinates, the potential and the kinetic energy read

$$2V = q^\dagger L^\dagger F L q = q^\dagger \Lambda q, \tag{B.6}$$

$$2T = \dot{q}^\dagger L^\dagger G^{-1} L \dot{q} = \dot{q}^\dagger E \dot{q}, \tag{B.7}$$

where Λ is a diagonal matrix from which the vibrational frequencies of the corresponding normal modes are obtained and E is the unit matrix. Using $L^\dagger = L^{-1}G$ in the first equation and multiplying by L on the left, we obtain

$$GFL = L\Lambda. \tag{B.8}$$

The transformation matrix L is determined from this equation when the F and G matrices are known. The vibrational frequencies of normal coordinates are obtained as

$$\omega_k = \frac{1}{2\pi c}\sqrt{\lambda_k}, \tag{B.9}$$

where λ_k are the components of the diagonal matrix Λ. Dimensionless normal coordinates (Q) from the mass weighted normal coordinates (q) are obtained by the following scaling factor

$$Q = (\frac{2\pi\omega c}{\hbar})^{\frac{1}{2}} q. \tag{B.10}$$

Appendix C

Fitting of PE surfaces to determine the JT and SO coupling parameters

The JT coupling parameters have been determined by a Levenberg-Marquardt least-squares fitting of adiabatic PE surfaces of the (nonrelativistic) JT Hamiltonian to the (nonrelativistic) *ab initio* data. The SO coupling parameter Δ has been obtained from the *ab initio* SO splitting at the D_{3h} reference geometry. For the second-order fitting, taking the mean and difference of the adiabatic electrostatic PE functions Eq. (3.19) and Eq.(3.20) in Subsection 3.1.1, we obtain

$$\frac{1}{2}(V_+ + V_-) = \frac{1}{2}\omega({Q_x}^2 + {Q_y}^2), \tag{C.1}$$

$$\frac{1}{2}(V_+ - V_-) = \sqrt{W^2 + Z^2}. \tag{C.2}$$

Ab initio potential energies are calculated for each component of the E states along the Q_x and Q_y direction of each degenerate mode. The function at the right-hand side of Eq. (C.1) are fitted to the mean of the potential energies of two components of the E state to obtain the vibrational frequency. The function at the right-hand side of Eq. (C.2) are fitted to the difference of the potential energies of two components of the E state to obtain the linear and quadratic JT coupling parameters. For the second-order fitting, the ab initio energies determined at about 50 geometries in the interval [-2, 2] for Q_x and Q_y have been used for the least squares fitting.

For the higher-order (sixth order) fitting, the mean and differences of adiabatic electrostatic PE functions Eq.(3.27) and Eq. (3.28) are

$$\frac{1}{2}(V_+ + V_-) = \sum_{n=0}^{6} \frac{1}{n!} 2U^{(n)} \tag{C.3}$$

$$\frac{1}{2}(V_+ - V_-) = \sqrt{\left(\sum_{n=0}^{6} \frac{1}{n!} W^{(n)}\right)^2 + \left(\sum_{n=0}^{6} \frac{1}{n!} Z^{(n)}\right)^2} \tag{C.4}$$

where $U^{(n)}$, $W^{(n)}$ and $Z^{(n)}$ are defined in Appendix A. For the large-amplitude degenerate bending mode, *ab initio* energy points at about 300 geometries for each of the E' and E''

states of interest have been computed along the Q_x and Q_y axes as well as along several cuts parallel to the Q_x and Q_y axes in the interval of [-12 : 12]. For the degenerate stretching mode, ab initio calculations along Q_x, Q_y and the diagonal cut, $Q_x/Q_y = 1$, were sufficient. The JT coupling parameters up to sixth order (in the bending mode) and fourth order (in the stretching mode) have been determined by a Levenberg-Marquardt least-squares fit.

Appendix D

The real Chebyshev wave-packet propagator for complex Hamiltonian

The following mapping between the complex number $x + iy$ and a real 2×2 matrix is used for the extension of the wave-packet propagation for complex-valued Hamiltonians[83]

$$x + iy \rightarrow \begin{pmatrix} x & -y \\ y & x \end{pmatrix} \; x, y \in \mathbf{R}. \tag{D.1}$$

Any complex $N \times N$ matrix can be mapped to an isomorphic real $2N \times 2N$ matrix, provided that functions of the matrices obey the following equation

$$f(\lambda_i^*) = f^*(\lambda_i) \tag{D.2}$$

where λ_i are the eigenvalues of the matrix.[88] As Eq. (D.2) is true for any real function of a Hermitian operator, the Hermitian Hamiltonian in the recursive propagation is also mapped to real symmetric matrix. Similarly, a complex-valued vector $v \in \mathbf{C}^N$ can be mapped to a real representation $v' \in \mathbf{R}^{2N}$ by

$$v_i \rightarrow \begin{pmatrix} Re[v_i] \\ Im[v_i] \end{pmatrix}. \tag{D.3}$$

The autocorrelation function (C_{2k}) is invariant under this mapping and the spectral distribution is preserved. As the recursion relation (Eq. (3.119)) contains only matrix-vector multiplications and the complex-valued Hermitian matrix as well as the vector can be mapped to real representations, the computation of JT-SO spectra can be performed over the field of real numbers. The propagation of a complex-valued wave-packet with a complex-valued Hamiltonian costs approximately four times of CPU time and twice the amount of memory than the propagation of a real-valued wavepacket with a real-valued Hamiltonian.

The autocorrelation function is calculated using the following relation

$$C_{2k} = \langle \Psi_0 | T_{2k}(H_s) | \Psi_0 \rangle = \langle \Psi_k | \Psi_k \rangle - C_0 \tag{D.4}$$

$$C_{2k+1} = 2\langle \Psi_{k+1} | \Psi_k \rangle - C_1. \tag{D.5}$$

Since the $2M \times 2M$ JT-SO Hamiltonian for spin multiplicity M can be written in block diagonal form, it is split in M copies of $2M \times 2M$ matrices with nonzero elements in only one 2×2 block. Therefore, instead of solving the TDSE using the full $2M \times 2M$ JT-SO Hamiltonian, it is solved M times using each of these M copies of 2×2 matrices. The spectral intensities obtained from these propagations are superimposed to yield the final spectrum.

Appendix E

Fitting of dipole moment surfaces

The TDM and dipole moment derivatives in the diabatic representation are extracted from *ab initio* adiabatic DMS of JT-active E states. The dipole moments as well as TDM for each displacement of nuclear coordinates Q_x and Q_y are obtained by ab initio electronic structure calculations using the CASSCF method. Adiabatic dipole moments at about 80 *ab initio* points for each of the E states of interest have been computed along the Q_x and Q_y axes as well as along several cuts parallel to the Q_x and Q_y axes. In some cases (e.g. the ${}^5E''$ state of MnF_3), the adiabatic dipole moments (especially the TDM) vary drastically near the CI. An ADT (Eq. (2.11)) of the electronic wavefunctions yields smooth diabatic DMS. In the ADT matrix $\theta(Q)$ is defined as

$$\theta(Q) = \frac{1}{2}\tan^{-1}\frac{2U_{12}}{U_{11}-U_{22}}, \tag{E.1}$$

where U_{11}, U_{22} are the diagonal elements and U_{12} is the offdiagonal element of the 2×2 diabatic PE matrix. In the diabatic representation, TDM are approximately constants and give the parameters $(\mu^{(0)}_{ex,xy},\ \mu^{(0)}_{ey,xy})$ for the calculation of internal vibronic spectra. The diabatic DMS are then fitted simultaneously along Q_x and Q_y with the linear expansions given in Eqs. (3.141, 3.142, 3.143, 3.144) to obtain the dipole moment derivatives with respect to Q_x and Q_y.

For ${}^4E'$ state of NiF_3, although the adibatic dipole moments and TDM are smoothly varying functions along the bending coordinates Q_x and Q_y, for consistency, parameters have been extracted by the fitting of the diabtaic DMS.

Appendix F

Expansion of dipole moment operator

Using the expansions (3.97) and (3.98) in Section 3.3, μ_{ex}^{fi} reads as

$$
\begin{aligned}
\mu_{ex}^{fi} &= \sum_{v_{x'},v_{y'}} \sum_{v_x,v_y} C^{*f}_{x,v_{x'},v_{y'}} C^{i}_{x,v_x,v_y} \langle v_{x'} v_{y'} | \langle \psi_x | \mu_{ex} | \psi_x \rangle | v_x v_y \rangle \\
&+ \sum_{v_{x'},v_{y'}} \sum_{v_x,v_y} C^{*f}_{x,v_{x'},v_{y'}} C^{i}_{y,v_x,v_y} \langle v_{x'} v_{y'} | \langle \psi_x | \mu_{ex} | \psi_y \rangle | v_x v_y \rangle \\
&+ \sum_{v_{x'},v_{y'}} \sum_{v_x,v_y} C^{*f}_{y,v_{x'},v_{y'}} C^{i}_{x,v_x,v_y} \langle v_{x'} v_{y'} | \langle \psi_y | \mu_{ex} | \psi_x \rangle | v_x v_y \rangle \\
&+ \sum_{v_{x'},v_{y'}} \sum_{v_x,v_y} C^{*f}_{y,v_{x'},v_{y'}} C^{i}_{y,v_x,v_y} \langle v_{x'} v_{y'} | \langle \psi_y | \mu_{ex} | \psi_y \rangle | v_x v_y \rangle \\
&= \sum_{v_{x'},v_{y'}} \sum_{v_x,v_y} C^{*f}_{x,v_{x'},v_{y'}} C^{i}_{x,v_x,v_y} \langle v_{x'} v_{y'} | \mu^0_{ex,xx} | v_x v_y \rangle \\
&+ \sum_{v_{x'},v_{y'}} \sum_{v_x,v_y} C^{*f}_{x,v_{x'},v_{y'}} C^{i}_{y,v_x,v_y} \langle v_{x'} v_{y'} | \mu^0_{ex,xy} | v_x v_y \rangle \\
&+ \sum_{v_{x'},v_{y'}} \sum_{v_x,v_y} C^{*f}_{y,v_{x'},v_{y'}} C^{i}_{x,v_x,v_y} \langle v_{x'} v_{y'} | \mu^0_{ex,yx} | v_x v_y \rangle \\
&+ \sum_{v_{x'},v_{y'}} \sum_{v_x,v_y} C^{*f}_{y,v_{x'},v_{y'}} C^{i}_{y,v_x,v_y} \langle v_{x'} v_{y'} | \mu^0_{ex,yy} | v_x v_y \rangle
\end{aligned} \tag{F.1}
$$

where $\mu^{(0)}_{ex,xx}$ refers to the dipole matrix element $\langle \psi_x | \mu^0_{ex} | \psi_x \rangle$. Since matrix elements of ${\mu_{ex}}^{(0)}$ in electronic basis do not depend on the nuclear coordinates (Condon approximation) and the nuclear basis functions are orthonormal, we obtain

$$
\begin{aligned}
\mu_{ex}^{fi} &= \sum_{v_{x'},v_{y'}} \sum_{v_x,v_y} C^{*f}_{x,v_{x'},v_{y'}} C^{i}_{x,v_x,v_y} \mu^0_{ex,xx} \delta_{v_x,v_{x'}} \delta_{v_y,v_{y'}} \\
&+ \sum_{v_{x'},v_{y'}} \sum_{v_x,v_y} C^{*f}_{x,v_{x'},v_{y'}} C^{i}_{y,v_x,v_y} \mu^0_{ex,xy} \delta_{v_x,v_{x'}} \delta_{v_y,v_{y'}} \\
&+ \sum_{v_{x'},v_{y'}} \sum_{v_x,v_y} C^{*f}_{y,v_{x'},v_{y'}} C^{i}_{x,v_x,v_y} \mu^0_{ex,yx} \delta_{v_x,v_{x'}} \delta_{v_y,v_{y'}} \\
&+ \sum_{v_{x'},v_{y'}} \sum_{v_x,v_y} C^{*f}_{y,v_{x'},v_{y'}} C^{i}_{y,v_x,v_y} \mu^0_{ex,yy} \delta_{v_x,v_{x'}} \delta_{v_y,v_{y'}} \\
&= \sum_{v_x,v_y} C^{*f}_{x,v_{x'},v_{y'}} C^{i}_{x,v_x,v_y} \mu^0_{ex,xx} \\
&+ \sum_{v_x,v_y} C^{*f}_{x,v_{x'},v_{y'}} C^{i}_{y,v_x,v_y} \mu^0_{ex,xy} \\
&+ \sum_{v_x,v_y} C^{*f}_{y,v_{x'},v_{y'}} C^{i}_{x,v_x,v_y} \mu^0_{ex,yx} \\
&+ \sum_{v_x,v_y} C^{*f}_{y,v_{x'},v_{y'}} C^{i}_{y,v_x,v_y} \mu^0_{ex,yy}. \qquad \text{(F.2)}
\end{aligned}
$$

Similarly μ_{nx}^{fi} can be written as

$$
\begin{aligned}
\mu_{nx}^{fi} &= \sum_{v_{x'},v_{y'}} \sum_{v_x,v_y} C^{*f}_{x,v_{x'},v_{y'}} C^{i}_{x,v_x,v_y} \langle v_{x'} v_{y'} | \langle \psi_x | \mu_{nx} | \psi_x \rangle | v_x v_y \rangle \\
&+ \sum_{v_{x'},v_{y'}} \sum_{v_x,v_y} C^{*f}_{x,v_{x'},v_{y'}} C^{i}_{y,v_x,v_y} \langle v_{x'} v_{y'} | \langle \psi_x | \mu_{nx} | \psi_y \rangle | v_x v_y \rangle \\
&+ \sum_{v_{x'},v_{y'}} \sum_{v_x,v_y} C^{*f}_{y,v_{x'},v_{y'}} C^{i}_{x,v_x,v_y} \langle v_{x'} v_{y'} | \langle \psi_y | \mu_{nx} | \psi_x \rangle | v_x v_y \rangle \\
&+ \sum_{v_{x'},v_{y'}} \sum_{v_x,v_y} C^{*f}_{y,v_{x'},v_{y'}} C^{i}_{y,v_x,v_y} \langle v_{x'} v_{y'} | \langle \psi_y | \mu_{nx} | \psi_y \rangle | v_x v_y \rangle \\
&= \sum_{v_{x'},v_{y'}} \sum_{v_x,v_y} C^{*f}_{x,v_{x'},v_{y'}} C^{i}_{x,v_x,v_y} \langle v_{x'} v_{y'} | \langle \psi_x | \left(\mu'_{nx,x} Q_x + \vec{\mu}'_{nx,y} Q_y \right) | \psi_x \rangle | v_x v_y \rangle \\
&+ \sum_{v_{x'},v_{y'}} \sum_{v_x,v_y} C^{*f}_{x,v_{x'},v_{y'}} C^{i}_{y,v_x,v_y} \langle v_{x'} v_{y'} | \langle \psi_x | \left(\mu'_{nx,x} Q_x + \vec{\mu}'_{nx,y} Q_y \right) | \psi_y \rangle | v_x v_y \rangle \\
&+ \sum_{v_{x'},v_{y'}} \sum_{v_x,v_y} C^{*f}_{y,v_{x'},v_{y'}} C^{i}_{x,v_x,v_y} \langle v_{x'} v_{y'} | \langle \psi_y | \left(\mu'_{nx,x} Q_x + \vec{\mu}'_{nx,y} Q_y \right) | \psi_x \rangle | v_x v_y \rangle \\
&+ \sum_{v_{x'},v_{y'}} \sum_{v_x,v_y} C^{*f}_{y,v_{x'},v_{y'}} C^{i}_{y,v_x,v_y} \langle v_{x'} v_{y'} | \langle \psi_y | \left(\mu'_{nx,x} Q_x + \vec{\mu}'_{nx,y} Q_y \right) | \psi_y \rangle | v_x v_y \rangle. \qquad \text{(F.3)}
\end{aligned}
$$

$$
\begin{aligned}
\mu_{nx}^{fi} = & \sum_{v_{x'},v_{y'}} \sum_{v_x,v_y} C^{*f}_{x,v_{x'},v_{y'}} C^{i}_{x,v_x,v_y} \left(\mu'_{nx,x,xx} \langle v_{x'} v_{y'} | Q_x | v_x v_y \rangle + \mu'_{nx,y,xx} \langle v_{x'} v_{y'} | Q_y | v_x v_y \rangle \right) \\
& + \sum_{v_{x'},v_{y'}} \sum_{v_x,v_y} C^{*f}_{x,v_{x'},v_{y'}} C^{i}_{y,v_x,v_y} \left(\mu'_{nx,x,xy} \langle v_{x'} v_{y'} | Q_x | v_x v_y \rangle + \mu'_{nx,y,xy} \langle v_{x'} v_{y'} | Q_y | v_x v_y \rangle \right) \\
& + \sum_{v_{x'},v_{y'}} \sum_{v_x,v_y} C^{*f}_{y,v_{x'},v_{y'}} C^{i}_{x,v_x,v_y} \left(\mu'_{nx,x,yx} \langle v_{x'} v_{y'} | Q_x | v_x v_y \rangle + \mu'_{nx,y,yx} \langle v_{x'} v_{y'} | Q_y | v_x v_y \rangle \right) \\
& + \sum_{v_{x'},v_{y'}} \sum_{v_x,v_y} C^{*f}_{y,v_{x'},v_{y'}} C^{i}_{y,v_x,v_y} \left(\mu'_{nx,x,yy} \langle v_{x'} v_{y'} | Q_x | v_x v_y \rangle + \mu'_{nx,y,yy} \langle v_{x'} v_{y'} | Q_y | v_x v_y \rangle \right) \\
= & \sum_{v_{x'},v_{y'}} \sum_{v_x,v_y} C^{*f}_{x,v_{x'},v_{y'}} C^{i}_{x,v_x,v_y} \left(\mu'_{nx,x,xx} \langle v_{x'} | Q_x | v_x \rangle \delta_{v_{y'},v_y} + \mu'_{nx,y,xx} \langle v_{y'} | Q_y | v_y \rangle \delta_{v_{x'},v_x} \right) \\
& + \sum_{v_{x'},v_{y'}} \sum_{v_x,v_y} C^{*f}_{x,v_{x'},v_{y'}} C^{i}_{y,v_x,v_y} \left(\mu'_{nx,x,xy} \langle v_{x'} | Q_x | v_x \rangle \delta_{v_{y'},v_y} + \mu'_{nx,y,xy} \langle v_{y'} | Q_y | v_y \rangle \delta_{v_{x'},v_x} \right) \\
& + \sum_{v_{x'},v_{y'}} \sum_{v_x,v_y} C^{*f}_{y,v_{x'},v_{y'}} C^{i}_{x,v_x,v_y} \left(\mu'_{nx,x,yx} \langle v_{x'} | Q_x | v_x \rangle \delta_{v_{y'},v_y} + \mu'_{nx,y,yx} \langle v_{y'} | Q_y | v_y \rangle \delta_{v_{x'},v_x} \right) \\
& + \sum_{v_{x'},v_{y'}} \sum_{v_x,v_y} C^{*f}_{y,v_{x'},v_{y'}} C^{i}_{y,v_x,v_y} \left(\mu'_{nx,x,yy} \langle v_{x'} | Q_x | v_x \rangle \delta_{v_{y'},v_y} + \mu'_{nx,y,yy} \langle v_{y'} | Q_y | v_y \rangle \delta_{v_{x'},v_x} \right) \qquad \text{(F.4)}
\end{aligned}
$$

Using the selection rules (3.101, 3.102) discussed in Section 3.3, the final form of μ_{nx}^{fi} is obtained as

$$
\begin{aligned}
\mu_{nx}^{fi} = & \frac{1}{\sqrt{2}} \sum_{v_{x'}} \sum_{v_x,v_y} C^{*f}_{x,v_{x'},v_y} C^{i}_{x,v_x,v_y} \mu'_{nx,x,xx} \left(\sqrt{v_x+1} \delta_{v_{x'},v_x+1} + \sqrt{v_x} \delta_{v_{x'},v_x-1} \right) \\
+ & \frac{1}{\sqrt{2}} \sum_{v_{y'}} \sum_{v_x,v_y} C^{*f}_{x,v_x,v_{y'}} C^{i}_{x,v_x,v_y} \mu'_{nx,y,xx} \left(\sqrt{v_y+1} \delta_{v_{y'},v_y+1} + \sqrt{v_y} \delta_{v_{y'},v_y-1} \right) \\
+ & \frac{1}{\sqrt{2}} \sum_{v_{x'}} \sum_{v_x,v_y} C^{*f}_{x,v_{x'},v_{y'}} C^{i}_{y,v_x,v_y} \mu'_{nx,x,xy} \left(\sqrt{v_x+1} \delta_{v_{x'},v_x+1} + \sqrt{v_x} \delta_{v_{x'},v_x-1} \right) \\
+ & \frac{1}{\sqrt{2}} \sum_{v_{y'}} \sum_{v_x,v_y} C^{*f}_{x,v_x,v_{y'}} C^{i}_{y,v_x,v_y} \mu'_{nx,y,xy} \left(\sqrt{v_y+1} \delta_{v_{y'},v_y+1} + \sqrt{v_y} \delta_{v_{y'},v_y-1} \right) \\
+ & \frac{1}{\sqrt{2}} \sum_{v_{x'}} \sum_{v_x,v_y} C^{*f}_{y,v_{x'},v_{y'}} C^{i}_{x,v_x,v_y} \mu'_{nx,x,yx} \left(\sqrt{v_x+1} \delta_{v_{x'},v_x+1} + \sqrt{v_x} \delta_{v_{x'},v_x-1} \right) \\
+ & \frac{1}{\sqrt{2}} \sum_{v_{y'}} \sum_{v_x,v_y} C^{*f}_{y,v_x,v_{y'}} C^{i}_{x,v_x,v_y} \mu'_{nx,y,yx} \left(\sqrt{v_y+1} \delta_{v_{y'},v_y+1} + \sqrt{v_y} \delta_{v_{y'},v_y-1} \right) \\
+ & \frac{1}{\sqrt{2}} \sum_{v_{x'}} \sum_{v_x,v_y} C^{*f}_{y,v_{x'},v_{y'}} C^{i}_{y,v_x,v_y} \mu'_{nx,x,yy} \left(\sqrt{v_x+1} \delta_{v_{x'},v_x+1} + \sqrt{v_x} \delta_{v_{x'},v_x-1} \right) \\
+ & \frac{1}{\sqrt{2}} \sum_{v_{y'}} \sum_{v_x,v_y} C^{*f}_{y,v_{x'},v_{y'}} C^{i}_{y,v_x,v_y} \mu'_{nx,y,yy} \left(\sqrt{v_y+1} \delta_{v_{y'},v_y+1} + \sqrt{v_y} \delta_{v_{y'},v_y-1} \right). \qquad \text{(F.5)}
\end{aligned}
$$

Appendix G

Analysis for the anomaly in the fitting of the PE curves of the $^4E'$ state of CrF_3

An anomaly has been observed in the PE curves of the $^4E'$ state of CrF_3 as a function of the Q_x bending coordinate (Fig. G.1). Among the JT effects considered in this work, this is the only example where the sixth-order JT model fails to provide an accurate fit of the *ab initio* electronic-structure data. The origin of this anomaly is a curve crossing of the lower adiabatic $^4E'$ potential-energy with the potential energy of the $^4A_1'$ ground state of CrF_3.

Fig. G.1 shows the potential-energy functions of the $^4E'$ and $^4A_1'$ states of CrF_3 as a function of the dimensionless bending coordinate Q_x. It is seen that an intersection of the $^4E'$ and $^4A_1'$ energy functions occurs at $Q_x \approx 8.0$. The $^4E'$ and $^4A_1'$ electronic states interact via the bending and stretching modes of e' symmetry ($(E' + A_1') \times (e' + e')$ PJT effect). In principle, a two-mode JT + PJT model Hamiltonian can be derived by an expansion up to sixth or higher-order, which provides an accurate description of the $(E' + A_1') \times (e' + e')$ three-state conical intersection problem.[74,89] The analysis of the PJT effect and its dynamic consequences (radiationless decay of the $^4E'$ excited state to the $^4A_1'$ ground state) is, however, beyond the scope of the present work.

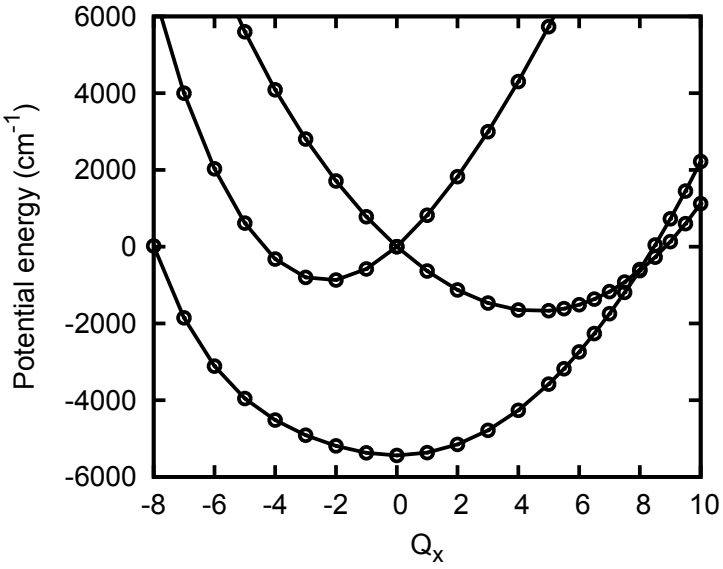

Figure G.1: PE curves of the ${}^4E'$ and ${}^4A_1'$ states of CrF_3 along dimensionless bending coordinate Q_x without SO coupling. The circles with solid lines correspond to the *ab initio* data.

Bibliography

[1] H. Jahn and E. Teller, Proc. Roy. Soc. Lond. A 161 (1937) 220.

[2] H. Jahn, Proc. Roy. Soc. Lond. A 164 (1938) 117.

[3] M. Born, Nachr. Akad. Wiss. Göttingen, Math-Physik. Kl. IIa (1951) 1.

[4] W. Domcke, D. R. Yarkony and H. Köppel (Eds.), Conical Intersections : Electronic Structure, Dynamics & Spectroscopy, World Scientific, Singapore, 2004.

[5] W. Domcke, D. R. Yarkony and H. Köppel (Eds.), Conical Intersections : Theory, Computation and Experiment, World Scientific, Singapore, 2011.

[6] I. Bersuker, The Jahn-Teller Effect, Cambridge University Press, Cambridge, 1979.

[7] M. D. Sturge, Solid State Phys. 20 (1967) 91.

[8] R. Englman, The Jahn-Teller Effect in Molecules and Crystals, Wiley, New York, 1972.

[9] F. T. Chau and L. Karlson, Phys. Scr. 16 (1977) 258.

[10] L. Wang, B. Niu, Y. T. Lee, D. E. Shirley, E. Ghelichkhani and E. R. Grant, J. Chem. Phys. 93 (1990) 6318.

[11] I. B. Bersuker, Chem. Rev. 101 (2001) 1067.

[12] H. Köppel, Z. Phys. Chem. 200 (1997) 3.

[13] B. E. Applegate, T. Barckholtz and T. A. Miller, Chem. Soc. Rev. 32 (2003) 38.

[14] G. Auböck, J. Nagl, C. Callegari and W. E. Ernst, J. Chem. Phys. 129 (2008) 114501.

[15] P. Pyykkö, Ann. Rev. Phys. Chem. 63 (2012) 45.

[16] F. S. Ham, Phys. Rev. A 138 (1965) 1727.

[17] A. J. Stone, Proc. Roy. Soc. Lond. A 351 (1976) 141.

[18] H. Koizumi and S. Sugano, J. Chem. Phys. 102 (1995) 4472.

[19] J. Schön and H. Köppel, J. Chem. Phys. 108 (1998) 1503.

[20] T. A. Barckholtz and T. Miller, Int. Rev. Phys. Chem. 17 (1998) 435.

[21] H. A. Bethe, Ann. Phys. 3 (1929) 10.

[22] J. H. Van Vleck, J. Chem. Phys. 7 (1939) 72.

[23] J. Kanamori, Progr. Theor. Phys. 17 (1957) 177.

[24] H. A. Bethe and E. E. Salpeter, Quantum Mechanics for One- and Two-Electron Atoms, Springer, Berlin, 1957.

[25] A. Wolf, M. Reiher, B. A. Hess and P. E. Schwerdtfeger, Relativistic Electronic-Structure Theory, Part I, Chapter 11, Elsevier, Amsterdam, 2002.

[26] L. L. Foldy and S. A. Wouthuysen, Phys. Rev. 78 (1950) 29.

[27] P. Schwerdtfeger, Relativistic Electronic-Structure Theory, Part II, Elsevier, Amsterdam, 2004.

[28] B. A. Hess, C. M. Marian, P. Jensen and P. R. E. Bunker, Computational Molecular Spectroscopy, Wiley, New York, 2000.

[29] D. G. Fedorov and M. S. Gordon, J. Chem. Phys. 112 (2000) 5611.

[30] L. V. Poluyanov and W. Domcke, Chem. Phys. 352 (2008) 125.

[31] R. Colton and J. H. Canterford, Halides of the First-Row Transition Metals, Wiley, New York, 1971.

[32] A. F. Wells, Structural Inorganic Chemistry, fourth ed., Clarendon Press, Oxford, 1975.

[33] J. H. Yates and R. M. Pitzer, J. Chem. Phys. 70 (1979) 4049.

[34] M. Hargittai, B. Reffy, M. Kolonits, C. J. Marsden and J. L. Heully, J. Am. Chem. Soc. 119 (1997) 9042.

[35] M. Hargittai, M. Kolonits, J. Tremmel, J. L. Fourquet and G. Ferey, Struct. Chem. 1 (1989) 75.

[36] G. V. Girichev, N. I. Giricheva, V. N. Petrova, S. A. Shlykov and E. Rakov, Zh. Strukt. Khim. 35 (1994) 61.

[37] V. N. Bukhmarina, A. Y. Gerasimov, Y. B. Predtechenskii and V. G. Shklyarik, Opt. Spectrosc. 65 (1988) 518.

[38] V. N. Bukhmarina, A. Y. Gerasimov and Y. B. Predtechenskii, Vib. Spectrosc. 4 (1992) 91.

[39] Y. B. Predtechenskii, R. B. Dushin and S. N. Nekhoroshkov, Opt. Spectrosc. 88 (2000) 862.

[40] O. P. Charkin and M. E. Dytkina, J. Struct. Chem. 5 (1964) 854.

[41] O. P. Charkin and M. E. Dytkina, J. Struct. Chem. 5 (1964) 858.

[42] O. P. Charkin, J. Struct. Chem. 10 (1969) 654.

[43] O. P. Charkin, Russ. J. Inorg. Chem. 18 (1973) 122.

[44] O. P. Charkin, J. Struct. Chem. 14 (1973) 355.

[45] J. W. Hastie, R. H. Hauge and J. L. Margrave, J. Chem. Phys. 51 (1969) 2648.

[46] T. C. De Vore, W. Weltner, Jr., J. Am. Chem. Soc. 99 (1977) 4700.

[47] V. Solomonik, J. E. Boggs and J. F. Stanton, J. Phys. Chem. A 103 (1999) 838.

[48] M. S. Child and L. S. Longuet-Higgins, Phil. Trans. R. Soc. London A 254 (1962) 259.

[49] W. R. Thorson, J. Chem. Phys. 29 (1958) 938.

[50] B. Scharf and T. A. Miller, J. Chem. Phys. 84 (1986) 561.

[51] J. K. G. Watson, Mol. Phys. 59 (1986) 127.

[52] M. Born and R. Oppenheimer, Ann. Phys. 389 (1927) 457.

[53] M. Born and K. Huang, Dynamical Theory of Crystal Lattice, 2nd Ed., Clarendon Press, Oxford, 1962.

[54] F. T. Smith, Phys. Rev. 179 (1969) 111.

[55] M. Baer, Chem. Phys. Lett 35 (1975) 112.

[56] H. Köppel, W. Domcke and L. S. Cederbaum, Adv. Chem. Phys. 57 (1984) 59.

[57] A. Shapere and F. E. Wilczek, Geometric Phases in Physics, World Scientific, Singapore, 1989.

[58] B. K. Kendrick, Conical Intersections, edited by W. Domcke, D. R. Yarkony and H. Koeppel, pp. 521-553, World Scientific, Singapore, 2004.

[59] I. B. Bersuker and V. Z. Polinger, Vibronic Interaction in Molecules and Crystals, New York, Springer, 1989.

[60] P. A. M. Dirac, Proc. Roy. Soc. A 117 (1928) 610.

[61] G. Breit, Phys. Rev. 34 (1929) 553.

[62] W. Heisenberg, Z. Phys. A. 39 (1926) 499.

[63] W. Pauli, Z. Phys. 43 (1927) 601.

[64] C. M. Marian, Spin-Orbit Coupling in Molecules, in K. Lipkowitz, D. Boyd (Eds.), Reviews in Computational Chemistry, Wiley-VCH, 2001.

[65] W. Domcke, S. Mishra and L. V. Poluyanov, Chem. Phys. 322 (2006) 405.

[66] C. Cohen-Tanoudji, B. Diu and F. Laloe, Quantum Mechanics, Vol. II, John Wiley & Sons, 1977.

[67] E. J. Heller, Acc. Chem. Res. 14 (1981) 368.

[68] R. Schinke, Photodissociation Dynamics, Cambridge University Press, Cambridge, 1993.

[69] D. J. Tannor, Introduction to Quantum Mechanics : A time-dependent perspective, University Science Books, Sausalito, 2006.

[70] J. P. Boyd, Chebyshev and Fourier Spectral Methods, Dover, New York, 2000.

[71] H. Tal-Ezer and R. Kosloff, J. Chem. Phys. 81 (1984) 3967.

[72] G. G. Balint-Kurti, Int. Rev. Phys. Chem. 27 (2008) 507.

[73] R. L. Whetten, K. S. Haber and E. R. Grant, J. Chem. Phys. 84 (1986) 1270.

[74] A. Viel and W. Eisfeld, J. Chem. Phys. 120 (2004) 4603.

[75] L. V. Poluyanov and W. Domcke, in The Jahn-Teller Effect : Fundamentals and Implications for Physics and Chemistry, edited by H. Koeppel, D. R. Yarkony and H. Barentzen, pp. 77-97, Springer, Berlin, 2010.

[76] P. R. Bunker and P. Jensen, Molecular Symmetry and Spectroscopy, National Research Council of Canada, 1998.

[77] E. Wigner, Group Theory, Academic, New York, 1959.

[78] E. B. Wilson, Jr., J. C. Decius and P. C. Cross, Molecular Vibrations, McGraw Hill, New York, 1955.

[79] H. C. Longuet-Higgins, U. Opik, M. H. L. Pryce and R. A. Sack, Proc. Roy. Soc. Lond. A 244 (1958) 1.

[80] D. O. Harris, G. G. Engerholm and W. D. Gwinn, J. Chem. Phys. 43 (1965) 1515.

[81] J. Echave and D. C. Clary, Chem. Phys. Lett. 190 (1992) 225.

[82] E. Anderson et. al., LAPACK User's Guide, 3rd Ed., Society for Industrial and Applied mathematics, Philadelphia, PA, 1999.

[83] D. Opalka, L. V. Poluyanov and W. Domcke, J. Chem. Phys. 135 (2011) 104108.

[84] C. W. Bauschlicher, Theor. Chim. Acta. 92 (1995) 183.

[85] T. H. Dunning, J. Chem. Phys. 90 (1989) 1007.

[86] H. J. Werner, et. al., MOLPRO, a package of ab initio programs, version 2006.1.

[87] V. G. Solomonik, V. V. Silznev and N. B. Balabanov, Z. Phys. Chem. 200 (1997) 77.

[88] D. W. Robinson, Math. Mag. 32 (1959) 213.

[89] A. Viel, W. Eisfeld, S. Neumann, W. Domcke and U. Manthe, J. Chem. Phys. 124 (2006) 214306.

Acknowledgments

First of all, I would like to express my deepest gratitude to Prof. Wolfgang Domcke for giving me oppotunity to work in such an interesting project in such a nice atmoshphere and for his sincere supervision, guidance and valuable suggestions throughout this work.

I am very thankful to Dr. Daniel Opalka for valuable discussions and help. I am grateful to all of my colleagues in theoretical chemistry department for their cooperation and helping hands in all respect. I would like to thank Frau Mösch for her help in all semi-academic matters. Thanks to Swarnendu and Riddhiman da for relaxing discussions during coffee break.

I am highly thankful to my Indian friends in Munich for giving a great friendly environment in a foreign land. Kiran da needs a special mention for his extensive help in the beginning of my life in Munich.

Thanks to Nirupam for his invaluable support.